Single-point diamond turning

SINGLE-POINT DIAMOND TURNING

T.C.G. LO-A-FOE

SINGLE-POINT DIAMOND TURNING

Proefschrift

ter verkrijging van de graad van doctor aan de Technische Universiteit Eindhoven, op gezag van de Rector Magnificus, Prof. ir. M. Tels, voor een commissie aangewezen door het college van dekanen in het openbaar te verdedigen op dinsdag 10 januari 1989 te 16.00 uur

door

TJOE CHONG GEORGE LO-A-FOE

geboren te Paramaribo

Druk: Boek en Offsetdrukkerij Letru, Helmond, 04920-37797

Dit proefschrift is goedgekeurd door de promotoren:
Prof.dr.ir. A.C.H. van der Wolf
en
Prof.ir. F. Doorschot

Copromotor: dr.ir. J.H. Dautzenberg

ERRATA

SINGLE-POINT DIAMOND TURNING

Page	Line	Text	should be replaced by
iv	27	betweeb	between
v	18	the section	the last section
v	25	f_{ef}	f_e
viii	14	eigen vector	eigenvector
viii	16	eigen frequency	eigenfrequency
1	24	machine data	machine
3	2	a least	at least
16	13	chip flow	chip flow direction
26	21,25	variation of	variation in
40	17	variation of	variation in
41	14	variation of	variation in
44	19	10.5 µm	10.5 μm^2
58	14	appendix A.1	appendix A
61	6	separate components	components
66	20	then estimates	then the estimates
76	25	in next	in the next
77	21	Fig.3.27	Fig.3.18
77	24	lathe for	lathe at
85	30	appropiate	appropriate
90	7	measurement	measured
97	3	is in	is in the
97	7	appendix A.1	appendix A
97	24	appendix A.2	appendix B
119	6	type of errors	types of error
122	11	in x-	in the x-
124	15	of the rotational	in the rotational
132	17,19	Appendix 4.A	Appendix C
140	18	variations of	variations in
144	21	Fig.6	Fig.4.21
144	23,25	variations of	variations in
145	5	type of errors	types of error
148	9	according (See	according to (See

Page	Line	Text	should be replaced by
156	28	can chosen	can be chosen
161	8	not necesarry	not necessary
161	20	except an	except a
162	26	2n eigenvalues	$2n_d$ eigenvalues
164	9,11,13	order n	order n_d
170	22,23,25	$r.\sin\beta_s$	$r.\cos\beta_s$
170	22	$\sqrt{(r^2-1)}$	$\sqrt{(r^2-x^2)}$
170	23	$-\frac{r}{\sin\beta_s}$	$+\frac{r}{\sin\beta_s}$
175	9	at straight	at a straight
178	3	binnen the	binnen de

Page 21 Figs.13a and 13b should be replaced by

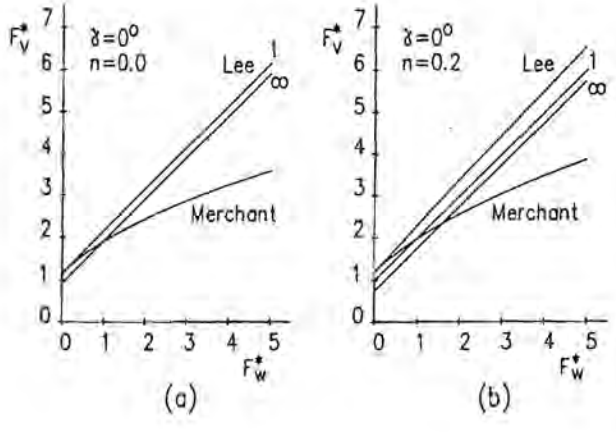

Page 171 Fig.C.1 $2r.\sin\beta_s$ should be replaced by $2r.\cos\beta_s$

TABLE OF CONTENTS

GLOSSARY OF SYMBOLS

A	area of the undeformed chip section	$[m^2]$
A_{VB}	area of contact between the work-piece and the flank wear land	$[m^2]$
A_{WS}	area of contact between the work-piece and the stylus	$[m^2]$
a	amplitude of a sinusoidal surface	[m]
a_k	scaling constant	[-]
B	system matrix	$[Nm^{-1}]$
b	depth of cut	[m]
b_o	average depth of cut	[m]
b_j	amplitude of the j^{th} variation in the depth of cut	[m]
b_{ce}	equivalent chip width	[m]
C	specific stress	$[Nm^{-2}]$
C	damping matrix	$[Nsm^{-1}]$
d	lateral resolution of a stylus instrument	[m]
E	modulus of elasticity	$[Nm^{-2}]$
E_o^*	specific energy	[-]
F_f	feed force	[N]
$F_j(t)$	time-dependent force on degree of freedom j	[N]
$F_j(i\omega)$	Fourier transform of $F_j(t)$	[N]
F_n	normal force	[N]
F_s	shear force in the shear plane	[N]
F_{sn}	normal force on the shear plane	[N]
F_R	resultant force between the tool face and the chip	[N]
F_R'	resultant force betweeb the work-piece and the chip	[N]
F_v	cutting force	[N]
F_v'	total cutting force	[N]
F_w	friction force	[N]
F_w'	total friction force	[N]

F_x	force component in x-direction	[N]
F_y	force component in y-direction	[N]
F_{11}	additional cutting force resulting from the rubbing action at the tool base	[N]
F_{12}	additional friction force resulting from the rubbing action at the tool base	[N]
F_{21}	additional cutting force resulting from the rubbing of the work-piece over the lower surface of the dead metal zone	[N]
F_{22}	additional friction force resulting from the rubbing of the work-piece over the lower surface of the dead metal zone	[N]
F_{31}	additional cutting force due to the chip sliding over the dead metal zone	[N]
F_{32}	additional friction force due to the chip sliding over the dead metal zone	[N]
ΔF_i	difference between the forces measured in the first and in the section of the test-piece	[N]
$\Delta F_{tot,i}$	sum of extra forces ΔF_i of preceeding measuring cycles	[N]
ΔF_v	additional cutting force	[N]
ΔF_w	extra friction force	[N]
f	feed	[m/r]
f	frequency of vibration	[Hz]
f_{ef}	equivalent undeformed chip thickness	[m]
G	modulus of elasticity in shear	$[Nm^{-2}]$
G_{IJ}	crosspower spectrum between the signals I and J	
H_{ij}	transfer function of forces at degree of freedom j to displacements at degree of freedom i	$[mN^{-1}]$
H_V	Vickers hardness	$[Nm^{-2}]$
h	depth of penetration	[m]
K	stiffness matrix	$[Nm^{-1}]$
k	spring constant	$[Nm^{-1}]$

L	triangle matrix after the Choleski decomposition	
M	mass matrix	[kg]
m	mass	[kg]
n	strain hardening exponent	[-]
n_d	number of degrees of freedom	[-]
n_s	number of shear planes in region 1	[-]
n_o	average number of revolutions	[r s^{-1}]
n_j	amplitude of the j^{th} variation in rotational speed	[r s^{-1}]
P	stylus loading	[N]
p_k	pole of mode k	[rad s^{-1}]
R	tip radius of the tool	[m]
R_a	average roughness	[m]
R_q	root-mean-square roughness	[m]
R_t	peak-to-valley height	[m]
R_w	radius of the work-piece	[m]
R_k	residue of mode k	[$mN^{-1}s^{-1}$]
r	cutting edge roundness	[m]
r	radius of the stylus	[m]
T	surface energy	[Nm^{-2}]
Δt	measuring error of the stylus instrument	[m]
U	real part of the residue	[$mN^{-1}s^{-1}$]
u	friction force per unit undeformed chip thickness along an unit length	[Nm^{-2}]
u_s	energy required to create two surfaces per unit volume	[Nm^{-2}]
V	imaginary part of the residue	[$mN^{-1}s^{-1}$]
v	cutting speed	[ms^{-1}]
v_f	feed velocity	[ms^{-1}]
v_{fo}	average feed velocity	[ms^{-1}]

v_{fj}	amplitude of the j^{th} variation in the feed velocity	$[ms^{-1}]$
$x(t)$	time-dependent displacement vector	[m]
$\dot{x}(t)$	time-dependent velocity vector	$[ms^{-1}]$
$\ddot{x}(t)$	time-dependent acceleration vector	$[ms^{-2}]$
$x_i(t)$	time-dependent displacement at degree of freedom i	[m]
$x_i(i\omega)$	Fourier transform of $x_i(t)$	[m]
Xo_i	x-position of the tool relative to the work-piece after i revolutions of the work-piece	[m]
ΔX_{fi}	displacement of the tool relative to the work-piece in x-direction due to cutting forces	[m]
Yo_i	y-position of the tool relative to the work-piece after i revolutions of the work-piece	[m]
ΔY_{fi}	displacement of the tool relative to the work-piece in y-direction due to cutting forces	[m]
Z	amplitude of the vibration in z-direction	[m]
β	friction angle	[-]
β_s	included angle of the stylus	[-]
γ	rake angle	[-]
γ_i	effective rake angle in shear plane i	[-]
γ^2_{UV}	coherence function of the signals U and V	[-]
δ	real part of the pole	$[rad\ s^{-1}]$
ϵ	strain	[-]
$\dot{\epsilon}$	strain rate	$[s^{-1}]$
$\bar{\epsilon}$	effective strain	[-]
$\bar{\epsilon}_{oi}$	effective strain in shear plane i	[-]
ζ_k	damping ratio for mode k	[-]
θ	stagnation point angle	[-]
θ_s	slope angle of the surface	[-]
κ	chip flow angle	[-]
λ	wavelength	[-]

λ	eigenvalue	[rad s^{-1}]
μ_f	coefficient of friction between the tool and the work-piece at the flank face	[-]
μ_r	coefficient of friction between the tool and the work-piece at the rake face	[-]
ν	damped natural frequency	[Hz]
σ	flow stress	[Nm^{-2}]
$\bar{\sigma}$	effective flow stress	[Nm^{-2}]
τ	shear stress	[Nm^{-2}]
φ	modal matrix	[-]
φ	shear angle	[-]
φ_i	shear angle in shear plane i	[-]
φ_j	phase of the j^{th} variation	[-]
Ψ_k	eigen vector for mode k	[-]
ω	radial frequency	[rad s^{-1}]
ω_k	undamped eigen frequency	[rad s^{-1}]
ω_j	radial frequency of the j^{th} variation	[rad s^{-1}]
ω_z	radial frequency of the vibration in z-direction	[rad s^{-1}]

ABSTRACT

This thesis deals with the influence of diverse parameters, that are involved in cutting, upon the surface quality of diamond turned products.
The aim of the study was to get a better understanding of the complex cutting process and, consequently, to improve cutting techniques and to meet the demand for better quality control in mass production.
Firstly, a cutting model for describing the influence of operational settings (cutting speed, feed and depth of cut), material properties of the work-piece (especially, its plastic properties), and tool geometry upon the cutting forces has been evaluated (Chapter 2).
The experiments showed that, several features that have been ignored in the starting model, such as the influence of the forces on the clearance face and of the strain rate upon material properties, may not be neglected in single-point diamond turning. If these effects are taken into account, the cutting forces can be predicted within 20%.
Then, the dynamic behaviour of the available precision machine has been determined by means of modal analysis (Chapter 3). This analysis showed that this behaviour was not optimal. Therefore, a method, which makes use of experimental data, has been applied in order to determine how the weak elements should be modified in order to improve the performance of the machine data. Finally, a numerical model, which includes the results from previous analyses, has been developed in order to simulate the direct influence of the operational settings, the material properties of the work-piece, the geometry of the cutting tool and the dynamic behaviour and their indirect influence, via the cutting forces, upon the surface roughness (Chapter 4).
This model has been evaluated; the experiments showed that the accuracy of this model is better than 10%.
The simulations of the influence of diverse parameters illustrated that valuable information about the machine and cutting tool condition can be extracted from the finished surface of the work-piece, but they also revealed that it is not possible to distinguish among all types of error.

1 General introduction

Over the last 200 years, progress towards greater precision has led to tolerances less than 1 micron and although many problems in micro-engineering have not been solved yet, components can be produced now with tolerances of a few nanometers.
The development of achievable machining accuracy over the last fifty years is shown in Fig.1.1 [1.1]. It also lists the processing equipment and dimensional measuring equipment by which the indicated resolution can be achieved.

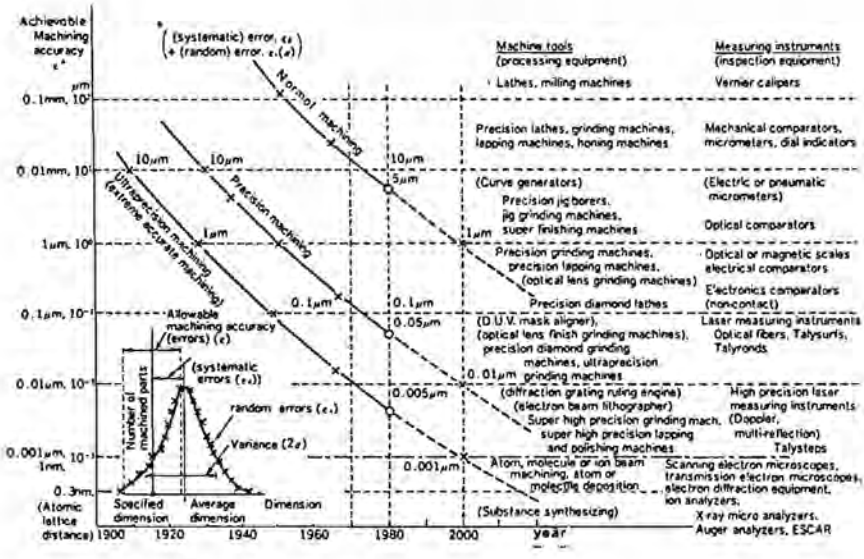

Fig.1.1. The development of achievable machining accuracy (after Taniguchi [1.1]).

It should be remarked that the curves present the highest possible machining accuracy at a given point in time that has been achieved at some laboratories and thus, may not be representative for commercial machines. The progress of the machining accuracy of these has not been as great as indicated in the figure. The difference between the accuracy of commercially available machines and that depicted in the figure may be even one order of magnitude [1.3].

Nevertheless, the progress of machining accuracy, which has improved by a least one order of magnitude in the past few decades, is still considerable. The main pressures for this development are the demand for greater miniaturization and increased packing densities, for better systems performance and longer reliable product lifes and for better quality control through higher machining accuracy, thereby, reducing waste, reworking and conventional inspections.
Today's accuracy targets are dimensional tolerances in the order of 0.01 μm and surface roughness in the order of 0.001 μm (1 nm).
The dimensions of machined components may be as small as 1 μm; for example: the patterns of integrated circuits, and the resolution and repeatability of operations must be in the order of 0.01 μm (10 nm).
Such requirements cannot be satisfied by a simple extension of conventional machining processes. In fact, a whole new range of techniques for the manufacture of parts with such accuracy limits has had to be developed and introduced [1.1],[1.2].
One of these techniques is diamond turning, a cutting process in which a diamond tool is used on a precision lathe under precisely controlled conditions.
Turning with a diamond tool is not a new technique in itself, since way back in 1777 Jessie Ramsden, the famous inventor, turned a lead screw using a diamond [1.4], but the development of modern machine-elements, measuring equipment, cutting tools, work materials and position control systems has dramatically changed the technique over the past few decades and, therefore, it may be called new.
The real development started in World War II with the research activities of some companies in the United States and Europe, including Dupont, Polaroid and Philips [1.4],[1.5] and they led to an improvement of profile accurary from a few micrometres to about 0.1 μm and surface roughness (peak-to-valley height) from 0.1 μm to less than 0.01 μm.

Products made by diamond turning include:
- cylinders for video tape recorders;
- drums for plain paper copiers;
- computer magnetic memory disc substrates;
- convex mirrors for high output carbon dioxide laser resonators;
- spherical bearing surfaces in beryllium,copper etc.;
- infra-red lenses made of germanium for thermal imaging systems;
- scanners for laser printers;
- elliptical mirrors for YAG (yttrium aluminium garnet) laser beam collectors;
- X-ray mirror substrates;
- moulds for Compact Disc lenses.

Although the great accuracies mentioned can be achieved nowadays, further improvements continue, mainly, driven by the demands for a higher product precision and better quality control in mass production. In order to meet these demands, the following conditions should be fulfilled:

a. The accuracy of tool motions and work operations should be less than 0.01 μm, since the target accuracy of surface roughness is now less than 0.01 μm.
The precision lathe usually comprises a spindle with hydrostatic or aerostatic bearings, hydrostatic or aerostatic linear slides, an air and/or oil supply system, a motor for driving the spindle and a position control system [1.6], [1.7], [1.8], [1.9].
In order to achieve the above mentioned accuracy the static, dynamic and thermal behaviour of the machine's components should be analysed and improved by levelling up the inherent precision of all the elements/sub-systems. This includes the selection or development of (a) elements with a higher stiffness and damping, plus a lower thermal expansion, (b) better production machines and (c) better measuring equipment. However, this is restricted by limitations of the material properties and the dimensions of the elements and a further improvement needs optimizing the assembly of the components.

Any remaining errors should be minimized by introducing better metrology and control systems, i.e. adaptive control of the machine-element motions, with a wide measuring and adjusting range, a high resolution and speed.
The tool operations will depend upon the environmental conditions too, and these should be controlled within exact limits. Vibrations of the foundations should be isolated from the tool/work zone and temperature variations of the machine-shop should be small. An effective method for controlling the temperature of the machine is to enclose the entire machine and work-piece with temperature controlled fluid. However, this is not always desirable and alternatives may include temperature-controlled air flow around the machine, or fluid passages in the the machine itself.

b. Better material production processes should be developed in order to improve the material behaviour during and after the cutting process.
Voids, inclusions and anisotropy of the material behaviour have a considerable influence upon surface roughness of the work-piece [1.10], [1.11] and the amount of these can be reduced by:
- production under high vacuum and zero gravity;
- selecting of nucleus-forming and grain-refining elements;
- controlling the temperature during production.

c. Diamond tools with an excellent cutting quality should be selected.
The use of a diamond tool has several advantages. The extreme hardness allows the fabrication of very sharp cutting edges which will produce mirror-like finishes after a single pass and the strength and toughness permits the machining of difficult materials which can hardly be worked with more conventional tools. However, the properties of diamond are very complex and how they are influenced by the cutting process is by no means clear [1.12],[1.13]. Therefore, there are no scientific specifications of diamond tools yet.

Diamond turning has been successfully performed on copper, gold, silver, aluminium, platinum, lead, nickel and plastic; however, the most interesting material, namely steel, still causes problems, due to the extremely high rate of tool wear. It is generally agreed that this is caused by a chemical affinity between the diamond and the metal, which leads to the degeneration of the diamond's lattice, but the process is still not well understood.

d. The operators must be skilled and have a 'feeling' for precision machining.
They must understand the importance of temperature, vibration and motion control and have a good knowledge of mechanics, optics, metallurgy and electronics.

It is obvious that fulfilling these conditions needs a very good understanding of the processes involved in cutting. In spite of the great progress made in the past few decades, such knowledge is still limited, mainly due to the large number of parameters, which have a role in the generation of surfaces and shapes, and the complexity of interactions between these parameters during the cutting process. Inputs of the cutting process include the properties of the tool and work-piece material and the behaviour of the machine. During the process, other parameters come into play, such as strains, temperatures and cutting forces, and these parameters interact with the other factors. Consequently, they will all have direct and indirect influences on the surface quality of machining.
The aim of this study is to determine some of these influences and, consequently, to get a better understanding of the cutting process. Firstly, the influences of operational settings (cutting speed, feed and depth of cut), material properties of the work-piece, especially, its plastic properties, and tool geometry upon the cutting forces have been investigated by means of a simple model for conventional cutting, which has been modified for single-point diamond turning (Chapter 2).

Then, the dynamic behaviour of the available precision machine has been determined by means of modal analysis (Chapter 3). This analysis showed that this behaviour was not optimal. Therefore, a method, which makes use of experimental data, has been developed in order to determine which modifications of the weak elements may be necesarry for a better performance of the machine.
Finally, the direct influences of the operational settings, the material properties of the work-piece, the geometry of the cutting tool and the dynamic behaviour and their indirect influences via the cutting forces has been estimated by means of a numerical model, which includes the results from previous analyses (Chapter 4).
This model may be used for developing a simple machine tool monotoring system based on the finished surface of the work-piece. This will also be discussed in Chapter 4.
Chapter 5 presents the final conclusions and makes suggestions for further research.

References

1.1. Taniguchi, N.:
Current Status in, and Future Trends of, Ultraprecision Machining and Ultrafine Materials Processing.
Annals of the CIRP, Vol.32/2, 1983, p.573-580.

1.2. McKeown, P.:
High precision manufacturing in an advanced industrial economy.
Preprints Precision Engineering, IPES4 (Cranfield), 1987, p.1-19.

1.3. Doorschot, F.:
Bewerkingstechnieken met een speciaal character (Dutch).
Review of some studies at the Eindhoven University of Technology.

1.4. Hannah, P.R.:
A personal prospective on the quest for higher precision diamond turning lathes.
Proc. Int. Congress for Ultraprecision Technology (Aachen), 1988, p.237-251.

1.5. Saito, T.T.:
Machining of optics: an introduction.
Applied Optics, Vol.14/8, 1975, p.1773-1776.

1.6. Brehm, P.B.:
Machinery considerations for precision machining.
SME-Technical Paper, MR78-956, 1978.

1.7. Barkman, W.E.; Steger, P.J.:
Diamond turning machine design overview.
SME-Technical Paper, MR78-959, 1978.

1.8. Kobayashi, A.:
Diamond Turning Machine Developments in Japan.
SME-Technical Paper, MR82-929, 1982.

1.9. Gijsbers, T.G.:
COLATH, a numerically controlled lathe for very high precision.
Philips Tech. Rev., 39, 1980, p.229-244.

1.10. Ohmori, G. and Takada, S.
Primary factors affecting accuracy in ultra precision machining by diamond tool.
Bull. Japan Soc. of Prec. Eng., Vol.16/1, 1982, p.8-15.

1.11. Stadler, H.J., Freisleben, B. and Heubeck, C.
Response of metallic material to micromachining.
Preprints Precision Engineering, IPES4, 1987.

1.12. Wilks, J.:
Performance of diamonds as cutting tools for precision machining.
Precision Engineering, Vol.2, No.2, 1980, p.57-71.

1.13. Ikawa, N.; Shimada, S.; Ohmori, G.:
Recent trends in diamond tool technology.
Proc. Int. Congress for Ultraprecision Technology (Aachen), 1988, p.126-142.

2. CUTTING FORCES

2.1 Introduction.

Metal cutting is composed of several processes such as:

a the separation of material at the tool tip;

b the process of changing the flow direction and thickening of the chip material and

c the burnishing process at the clearance face.

Each of these processes plays an important role in the surface generation mechanism. Therefore, it is necessary to have a good understanding of these processes in order to improve cutting techniques and the quality of the products. It means an advanced knowledge of the influences of the parameters involved in cutting. Inputs to the cutting process include the properties of the work-piece and the tool, the operational settings and the behaviour of the machine.

A multiplicity of interactions between these parameters and additional factors, such as the temperatures, the strains, the strain rates, the stresses and the forces, occurs during the cutting process.

This multiplicity of interactions and the lack of geometrical constraint make cutting a complex process and account for the extremely wide range of views that have appeared in literature to explain cutting results.

Many simple models have been proposed for describing the processes [2.1- 2.20]. Their publication started in 1870 [2.12] and the end has not come yet, since there is still no universally accepted method. Most of the proposed models were supported by sound experimental data, but the range of cutting conditions was small and in most cases, they failed to hold when applied to different operating conditions.

The reason for this failure is that these models are dealing with only a few features of the cutting process, while experience teaches that no mechanism dominates over the whole range of operating conditions.
A model which holds for the whole range of operating conditions should deal with all the possible mechanisms involved in cutting. Such a model will be too heavy to handle, since it will contain many undetermined factors.
A more practical approach will be the use of a combination of a few relatively simple models, each describing one or two key effects and valid for the range of conditions of interest.
Due to the poor understanding of the cutting phenomena, it is difficult to decide which model is the best to start with. Practically all of the simple solutions that have been previously published represent good models over a limited range of operating conditions and the numerous discussions about these [2.11], [2.21-2.22] did not result in the selection of the most outstanding one.
In the following sections some models will be discussed and the least objectionable will be chosen and evaluated for the operating conditions in single-point diamond turning. The attention will be restricted to global parameters, such as the cutting forces. Local parameters, including local stresses and strains, are important with respect to the surface generation and the wear rate of the tool, but a model for these parameters will contain many unknown factors, such as the geometry of the processes and the local material properties during cutting. Most of these unknown variables cannot be determined due to a lack of appropriate measuring facilities.

2.2 Orthogonal cutting.

Most of the models are based on the following assumptions:

1. The cutting edge is a straight line extending perpendicular to the velocity vector.
2. The chip does not flow to either side (plane strain).
3. The tool is perfectly sharp and there is no contact along the clearance face.
4. The depth of cut is constant.
5. The velocity is uniform.
6. A continuous chip is produced.
7. The shear surface is a plane extending upward from the cutting edge.

With these assumptions the geometry of the cutting process can be simplified to one representative plane (Fig.2.1). Such an ideal two-dimensional cutting operation is referred to as orthogonal cutting and its geometry is completely defined by the feed (f), the shear angle (φ) and the rake angle (γ).

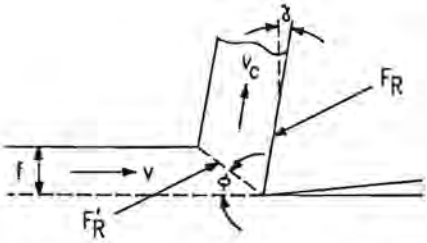

Fig.2.1. Schematic representation of the orthogonal cutting process.

The resultant forces – the force between the tool face and the chip (F_R) and the force between the work-piece and the chip along the shear plane (F'_R) – can be resolved into three sets of components as indicated in Fig.2.2a.

1. In the horizontal and the vertical direction, F_v and F_f.
2. Along and perpendicular to the shear plane, F_s and F_{sn}.
3. Along and perpendicular to the tool face, F_w and F_n.

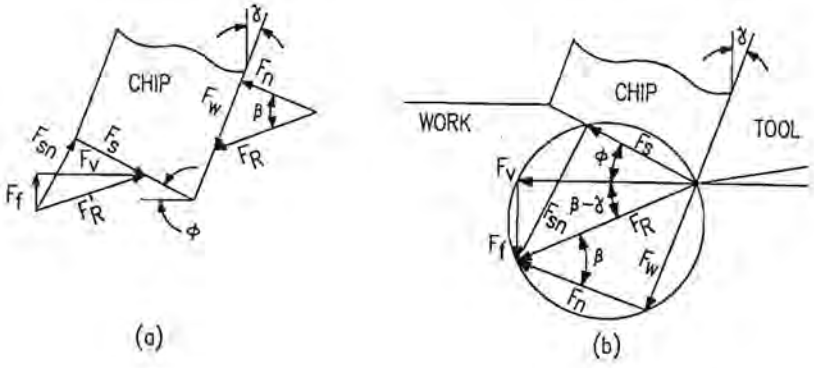

Fig.2.2. The components of the forces on the chip (a) and the compact cutting force circle (b).

For the equilibrium, F_R and F'_R must be equal and parallel, so a compact diagram (Fig.2.2b) can be obtained if these forces are plotted at the tool point instead of at their actual points of application.

The force components on the tool face and on the shear plane can be related to the horizontal and the vertical components, F_v and F_f, which are normally the measured forces:

$$F_w = F_v.\sin\gamma + F_f.\cos\gamma \quad (2.1)$$

$$F_n = F_v.\cos\gamma - F_f.\sin\gamma \quad (2.2)$$

$$F_s = F_v.\cos\varphi - F_f.\sin\varphi \quad (2.3)$$

$$F_{sn} = F_v.\sin\varphi + F_f.\cos\varphi \quad (2.4)$$

In the following sections some models for predicting the force components will be discussed.

2.2.1 Model of Merchant

With the assumption that the shear stress along the shear plane is uniform, the following relationships for the cutting forces can be derived:

$$F_v = \tau.A.\frac{\cos(\beta-\gamma)}{\cos(\varphi+\beta-\gamma).\sin\varphi} \tag{2.5}$$

$$F_f = \tau.A.\frac{\sin(\beta-\gamma)}{\cos(\varphi+\beta-\gamma).\sin\varphi} \tag{2.6}$$

where

τ = shear stress along the shear plane

A = area of the undeformed chip section

β = friction angle = $\tan^{-1}(\mu_r)$ (2.7)

μ_r = mean coefficient of friction on the rake face.

The shear angle (φ) is the only unknown factor. Consequently, if it can be related to the known factors then the forces can be predicted.

Merchant [2.2] assumed that φ would be such that the total power consumed in the cutting process would be a minimum.
The expression for the total power is:

$$P = F_v.v = \tau.A.v.\frac{\cos(\beta-\gamma)}{\sin\varphi.\cos(\varphi+\beta-\gamma)} \tag{2.8}$$

The following relationship for the shear angle (φ) was obtained by differentiating Eq.(2.8) with respect to φ, thereby considering the shear stress (τ) and the friction angle (β) to be independent of φ, and equating the result to zero.

$$\varphi = 45^{\circ} - \frac{\beta}{2} + \frac{\gamma}{2} \tag{2.9}$$

2.2.2 Model of Lee and Shaffer

With the assumptions that the material cut behaves as an ideal plastic which does not strain harden and, that the shear plane represents a direction of maximum shear stress, Lee and Shaffer [2.3] proposed a slip-line field A-B-C as indicated in Fig.2.3a.
Since this region is subjected to an uniform state of stress, it can be characterized by a single Mohr's stress circle diagram (Fig.2.3b). Here point a corresponds to the stress on face A-B, which is the shear plane with the maximum shear stress and point b represents the stress on face B-C along which the stress is zero.

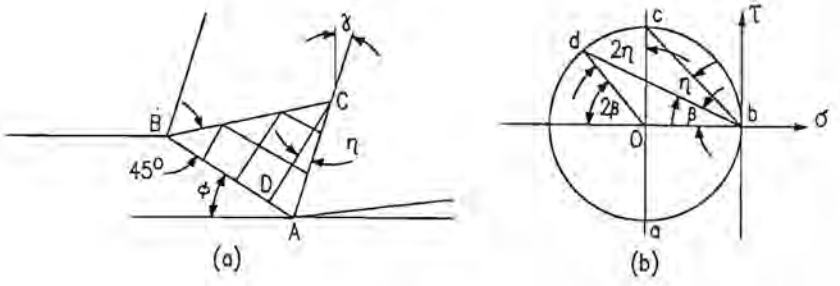

Fig.2.3. Stress field at the tool point for an ideal plastic material. (a) Slip line field. (b) Mohr's circle diagram for field ABC.

Because the Mohr's circle has a double-angle feature and point b in Fig.2.3b is 90 degrees from point a, the angle between face B-C and face A-B will be 45 degrees (Fig.2.3a). In a similar way point c in Fig.2.3b represents the stress on face C-D with the maximum shear stress in Fig.2.3a and the stress on the tool face A-C in Fig.2.3a is represented as point d in Fig.2.3b.
The angle dbO in Fig.2.3b is the friction angle (β). If the angle dOc is taken to be 2η, the angle ACD will be η and it can be seen from Fig.2.3b that:

$$\eta = 45^{\circ} - \beta \qquad (2.10)$$

and from Fig.2.3a:

$$\eta = \varphi - \gamma \tag{2.11}$$

With these equations the relationship for the shear angle (φ) is:

$$\varphi = 45^{o} - \beta + \gamma \tag{2.12}$$

2.2.3 Model of Dautzenberg

The model [2.17 - 2.19] is based on the following assumptions (Fig.2.4):

- there are two regions of deformation.
  In the first region the chip flow is changed without any thickening of the chip and in region 2 the chip thickness increases due to the friction between the chip and the tool.
- the supplied power is completely dissipated by the two plastic processes.
- the work material behaves according to the constitutive equation of Lüdwik:

$$\bar{\sigma} = C.\bar{\varepsilon}^{n} \tag{2.13}$$

where : $\bar{\sigma}$ = effective stress

$\bar{\varepsilon}$ = effective strain

n = strain hardening exponent

C = specific stress

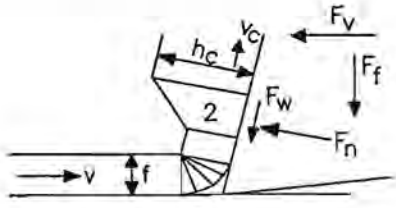

Fig.2.4. Representation of the two dimensional cutting process.

In region 1 (Fig.2.5) the mean chip velocity (v) is the same as the cutting speed. Area 1 is unloaded and on the areas 2 and 3 forces and a moment are in effect.

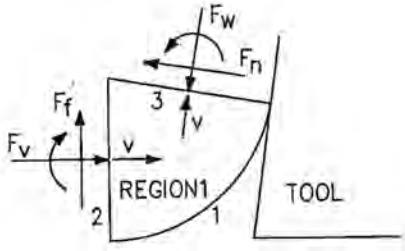

Fig.2.5. Global equilibrium of region 1.

The power balance is:

$$F_v.v - F_w.v = \int_0^{\bar{\epsilon}} \sigma.d\epsilon.b.f.v \qquad (2.14)$$

Substitution of Eq.(2.13) in Eq.(2.14) and dividing by the term Cbfv gives:

$$F_v^* = F_w^* + \int_0^{\bar{\epsilon}_1} \bar{\epsilon}^n.d\bar{\epsilon} \qquad (2.15)$$

with: $F_v^* = \dfrac{F_v}{Cbf}$ = cutting force number (dimensionless) (2.16)

$F_w^* = \dfrac{F_w}{Cbf}$ = friction force number (dimensionless) (2.17)

$\bar{\epsilon}_1$ = effective enddeformation in region 1

Eq.(2.15) holds for each form of the stream profile of the material in region 1, i.e. bending or shear.

In order to find the minimum energy for the plastic process in region 1 the term $\int_0^{\bar{\epsilon}_1} \bar{\epsilon}^n . d\bar{\epsilon} = \frac{1}{n+1} . (\bar{\epsilon}_1)^{n+1}$, which will be referred to as the specific energy E_o^*, is minimized [2.18].
It depends upon the number of shear planes, n_s, in region I (Fig.2.6). This number may vary between 1 and ∞ .

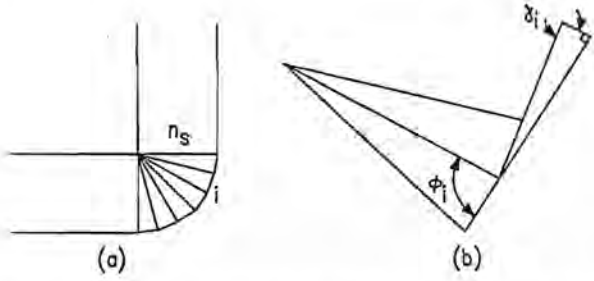

Fig.2.6. Region 1 with n_s shear planes. (b) The shear angle φ_i and rake face γ_i for shear plane i.

For n_s shear planes the strain $\bar{\epsilon}_{oi}$ in shear plane i will be:

$$\bar{\epsilon}_{oi} = \frac{\cos\gamma_i}{\sqrt{3} . \sin\varphi_i . \cos(\varphi_i - \gamma_i)} \qquad (2.18)$$

$$\text{with } \varphi_i = \frac{\pi}{4} + \frac{\gamma_i}{2} \qquad (2.19)$$

and the relationship for the specific energy is:

$$E_o^* = \frac{1}{n+1} . \left(\sum_{j=1}^{n_s} \bar{\epsilon}_{oi} \right)^{n+1} \qquad (2.20)$$

The minimizing of E_o^* with respect to γ_i results in the following expression:

$$\gamma_i = \frac{\pi}{2} - \frac{\pi - 2\gamma}{2n_s} \tag{2.21}$$

Substitution of Eq.(2.19) and Eq.(2.21) in Eq.(2.18) gives:

$$\bar{\epsilon}_{oi} = \frac{2}{\sqrt{3}} \cdot \tan\left(\frac{\pi - 2\gamma}{4n_s}\right) \tag{2.22}$$

Hence, the equation for the specific energy becomes:

$$E_o^* = \frac{1}{n+1} \cdot \left\{ n_s \cdot \frac{2}{\sqrt{3}} \cdot \tan\left(\frac{\pi - 2\gamma}{4n_s}\right) \right\}^{n+1} \tag{2.23}$$

With this equation the relationships for the forces are [1.18]:

- For one shear plane in region 1 ($n_s = 1$):

$$F_v^* = F_w^* + \frac{1}{n+1} \cdot \left\{ \frac{2}{\sqrt{3}} \cdot \tan\left(\frac{\pi - 2\gamma}{4}\right) \right\}^{n+1} \tag{2.24}$$

- For an infinite number of shear planes in region 1 ($n_s = \infty$):

$$F_v^* = F_w^* + \frac{1}{n+1} \cdot \left\{ \frac{\pi - 2\gamma}{2\sqrt{3}} \right\}^{n+1} \tag{2.25}$$

2.2.4 Comparison of the models

The force relationships of the models of Merchant and Lee and Shaffer can be compared to those of Dautzenberg in terms of dimensionless forces.

The general force relationships are:

$$F_v = \tau . A . \frac{\cos(\beta - \gamma)}{\cos(\varphi + \beta - \gamma) . \sin\varphi} \tag{2.5}$$

$$F_w = \tau . A . \frac{\sin\beta}{\cos(\varphi + \beta - \gamma) . \sin\varphi} \tag{2.26}$$

In order to compare the models in similar terms of dimensionless forces, namely F/CA, the following relationship, which is based on the von Mises criterion and the equation of Lüdwik Eq.(2.13), is used for the shear stress (τ):

$$\tau = \frac{1}{\sqrt{3}}.C.\bar{\epsilon}^{n} \tag{2.27}$$

For the effective strain ($\bar{\epsilon}$) it holds:

$$\bar{\epsilon} = \frac{\cos\gamma}{\sqrt{3}.\sin\varphi.\cos(\varphi-\gamma)} \tag{2.28}$$

The relationships in terms of dimensionless forces are now derived by substitution of the Eqs.(2.27) and (2.28) in the Eqs.(2.5) and (2.26), followed by dividing the resulting equations by the term CA.

$$F_v^* = \frac{1}{\sqrt{3}}.\left(\frac{\cos\gamma}{\sqrt{3}.\sin\varphi.\cos(\varphi-\gamma)}\right)^{n}.\frac{\cos(\beta-\gamma)}{\cos(\varphi+\beta-\gamma).\sin\varphi} \tag{2.29}$$

$$F_w^* = \frac{1}{\sqrt{3}}.\left(\frac{\cos\gamma}{\sqrt{3}.\sin\varphi.\cos(\varphi-\gamma)}\right)^{n}.\frac{\sin\beta}{\cos(\varphi+\beta-\gamma).\sin\varphi} \tag{2.30}$$

The specific relationships for Merchant and Lee and Shaffer are obtained by replacing the shear angle (φ) by terms of the rake angle (γ) and the friction angle (β) according to their shear angle relationships Eqs.(2.9) and (2.12).
Then, the dimensionless forces depend only upon the rake angle (γ), the friction angle (β) and the hardening exponent (n) and the models can be compared by calculating the dimensionless forces for some values of these variables (Fig.2.7).
Fig.2.7a shows that the model of Dautzenberg for one shear plane (n_s=1) will give the same results as the model of Lee and Shaffer if n and γ are zero. This is not surprising, since Lee and Shaffer assumed that the work-piece material behaves as an ideal plastic and, that there is one shear plane, which represents a direction of maximum shear stress.

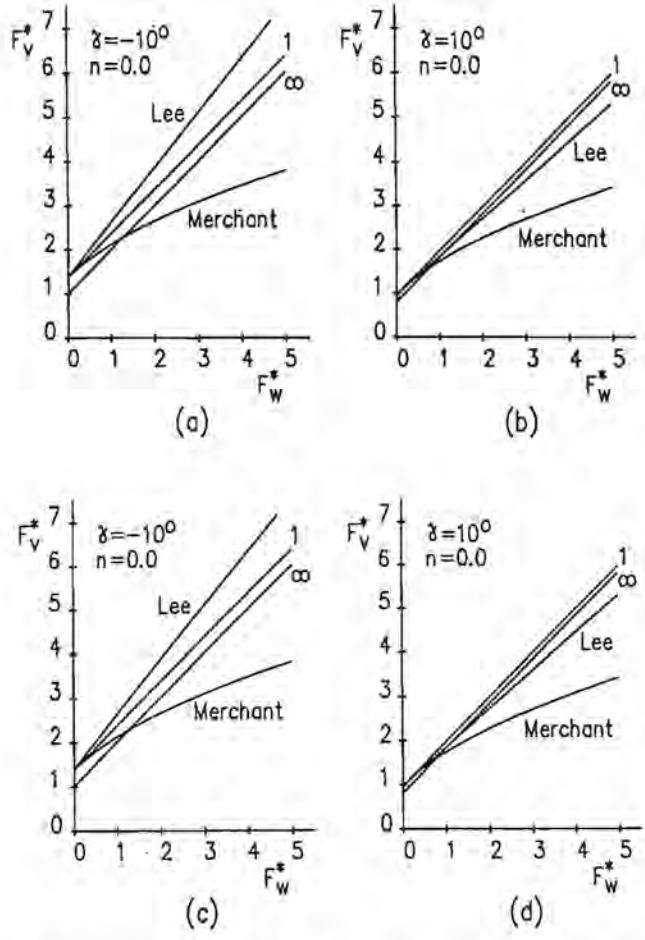

Fig.2.7. The cutting force number versus the friction force number for several models, materials and rake angles of the tool.

The ideal plastic solution of Lee and Shaffer also indicates that the shear stress and the normal stress on the shear plane should be equal (point a in Fig.2.3b), which is generally not the case [2.23]. This is the main reason for the deviations at other values of the rake angle (Fig.7c and d).

The difference between the relationship of the model of Dautzenberg and that of the model of Merchant is large. It can be explained by the following reason.

Merchant assumed that the shear stress on the shear plane is independent of the shear angle. This assumption is questionable, because the shear stress depends upon the shear angle according to Eq.(2.27) and most materials strain-harden ($n > 0$); however some experiments show that at high cutting speed the work-hardening effects are small and the static stress-strain curve can be replaced by a flat-topped stress-strain relationship. But the stress also depends upon the strain rate, which is a function of the shear angle, and the assumption remains doubtful.

Due to the questionable assumptions, the models of Merchant and Lee and Shaffer are open to doubt. Since the assumptions of Dautzenberg are less objectionable and, a promising experimental correspondence was obtained in previous studies, his model is regarded as the best to start with.

It should be noticed that the models discussed so far are simple models, which have ignored several features of the cutting process, such as the influence of the hydrostatic pressure upon the shear flow stress [2.23], the forces on the clearance face [2.14], the nose forces [2.15], the side spread of the chip [2.24], the strain rate and the temperature upon the material properties [2.25], the chip curl [2.26] and the stress distributions on the rake face [2.20]. Although the incorporation of these factors results in some improvement of the models, none of them have been generally accepted yet, mainly due to the uncertainties and complexities associated with the accurate measurement of the parameters involved. In spite of this, some of the features will be considered in the following sections, because the influence of these may be significant in single-point diamond turning.

It should also be remarked, that region 2 in the model of Dautzenberg has not been considered. Hence, only one equation (Eq.(2.24) or Eq.(2.25)) is available, while there are two unknown variables (F_v and F_w). Therefore, the forces cannot be predicted. A second equation will be discussed in section 2.5.4.

2.3 Non-orthogonal cutting

The force relationships have been derived for the orthogonal cutting process, which is assumed to be two-dimensional. However, single-point diamond cutting is a three-dimensional non-orthogonal process, in which the chip can be regarded as the sum of oblique chips having various thicknesses (Fig.2.8). This means that the equations cannot be used without modifications.

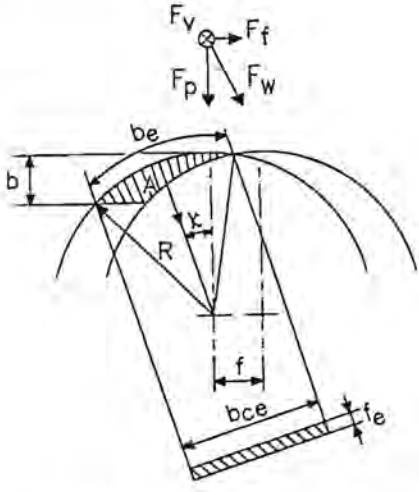

Fig.2.8. The geometry in single-point diamond turning.

For the sake of simplicity, two additional assumptions are made:
- the cutting process is a two-dimensional process with a cutting edge angle κ, which is the same as the chip flow angle.
- the direction of the chip flow is perpendicular to the tool edge in the middle of the width of contact between the tool edge and the work-piece material (Fig.2.8).

With these assumptions, only the Eqs.(2.1) and (2.2) change:

$$F_w = F_v.\sin\tau + (F_f.\sin\kappa + F_p.\cos\kappa)\cos\tau \qquad (2.31)$$

$$F_n = F_v.\cos\tau - (F_f.\sin\kappa + F_p.\cos\kappa)\sin\tau \qquad (2.32)$$

The term bf in the force number Eqs.(2.16) and (2.17) should be replaced by the term $b_{ce}f_e$ which is the area of the undeformed chip section A (Fig.2.8).

Young [2.27] showed that a better estimation of the chip flow angle can be made by means of a model, which assumes that:

1. the friction force per unit undeformed chip thickness along a unit length is a constant, u, and
2. the local chip flow direction is normal to the cutting edge for the element considered (Fig.2.9).

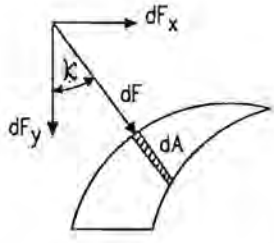

Fig.2.9. The local flow direction for an element of the chip.

With these assumptions the expressions for the resulting forces are:

$$F_x = u.\int\sin\kappa.dA \qquad (2.33)$$

$$F_y = u.\int\cos\kappa.dA \qquad (2.34)$$

The resulting chip flow angle is :

$$\bar{\kappa} = \tan^{-1}(F_x/F_y) \qquad (2.35)$$

The flow angles calculated with this equation are larger than those which follow from the simple assumption, but the differences are only a few degrees for the conditions of interest (Fig.2.10) and the force components will differ only a few percent, so it is not worth applying the more laborious model of Young.

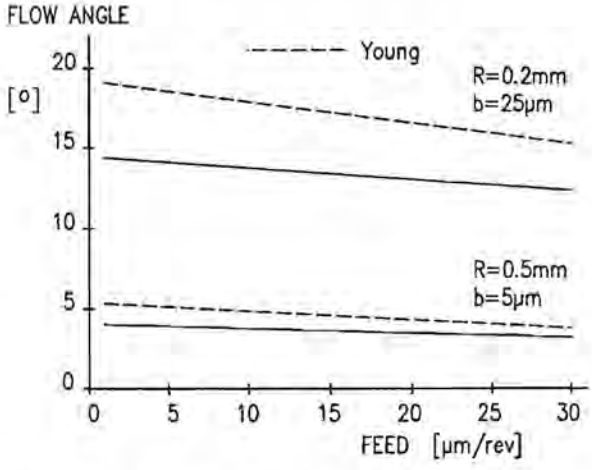

Fig.2.10. The chip flow angle versus the feed for the model of Young in comparison with the simple model at different values of the tool radius (R) and the depth of cut (b).

2.4 Experiments

In order to evaluate the cutting model plain turning tests have been carried out with the experimental set-up described in the next section and under the test conditions mentioned in section 2.4.2.

2.4.1 Experimental set-up

The experiments have been carried out on a precision lathe with hydrostatic bearings. A detailed description of this lathe is given in chapter 3 and only the features which are relevant to the measurement of the forces are mentioned in this chapter.
The shaft of the spindle can make a travel in the direction of the axis of rotation. The speed in this direction, which is the feed velocity in plain (longitudinal) cutting, can be adjusted by variable flow-control valves.
This speed should be constant in time; however, it varied. This was caused by geometric errors of the elements of the spindle. The magnitude of variation was about 25 μm/s, which is only a few percent with respect to a high speed of 1 mm/s, but 25% with respect to a low speed of 0.1 mm/s. In order to reduce this inadmissible variation of the speed to only a few μm/s the spindle should be modified drastically. As this would be time consuming, another solution was chosen for this problem. The test-piece was divided into 5 sections by making grooves in it (Fig.2.11). The variation of the speed in a section is small and the mean speed in each section can be determined, so reliable measurements can be made.

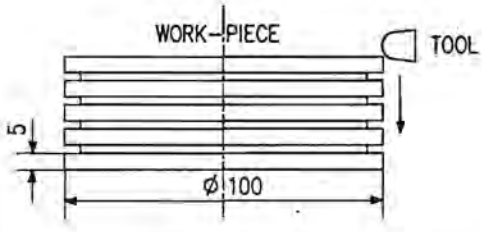

Fig.2.11. The geometry of the work-piece with grooves.

The arrangement of the measuring equipment is shown in Fig.2.12. The forces were measured by a dynamometer with a three component Kistler-piezo-element (type 9251A). The induced signals were amplified by three Kistler type 5007 charge amplifiers and the final signals were recorded on a Yew multi-pen x-t recorder (type 3066).

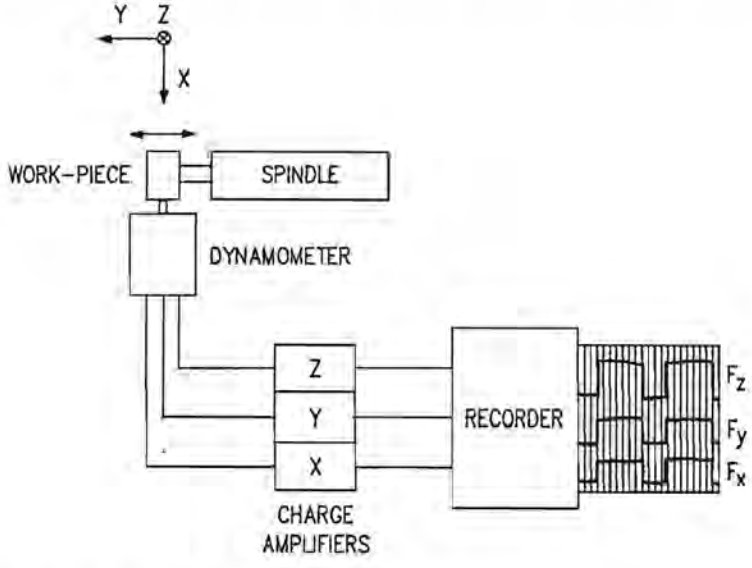

Fig.2.12. *The arrangement of the measuring equipment.*

In order to reduce the drift of the signals due to heat transfer from the tool to the piezo-element, a zerodur toolholder was used. Temperature variation in the piezo-element was also caused by the mist lubrication and the heating of chips, but it could be minimized by putting a tempex screen in front of the dynamometer.
The drift-effect was also controlled by making the grooves in the test-piece.

After making these adjustments, the force measuring resolution was better than 3 mN with an accuracy of about 5%, depending upon the mutual influencing of the piezo-elements (<1.16%) and the accuracy of the charge amplifier (± 1% of the full scale) and the pen recorder (± 0.25% of the full scale).

The dynamometer was mounted on the carriage via a double-screw slide in order to adjust the depth of cut, which was measured by a mikrokator (resolution 1 μm).

2.4.2 The test conditions

The work-piece materials were aluminium and brass, of which the chemical composition is listed in table 2.1.

Table 2.1. The chemical composition of the work-piece materials.

DIN	Standard No.	Cu %	Pb %	Sn %	Fe %	Ni %	Si %	Mn %	Mg %	Al %	Zn %
AlMgSi0.8	3.2316	<0.1	-	-	-	-	0.8-1.2	1	0.6	rest	rest
CuZn40Pb3	2.0405	58-60	2	0.9	0.7	1	0.05	0.5	-	-	-

The specific parameters C and n of these materials were determined from tensile tests with a strain rate ($\dot{\epsilon}$) of about 10^{-3} s^{-1} and the values are mentioned in table 2.2.

Table 2.2. The plastic material properties of the work-piece materials.

DIN	C N/mm^2	n -
AlMgSi0.8	485	0.15
CuZn40Pb3	750	0.30

Two tools with different radii, namely 0.2 and 0.5 mm, were selected and the rake angle of the tools was 0^{o}.
The operational settings were:
- cutting speed 8 m/s
- feed 5 - 50 μm/rev
- depth of cut 5 - 20 μm

The forces were divided by the specific stress and the area of the undeformed chip section in order to get the dimensionless force numbers.

2.5 Results and discussion

The experimental and theoretical results are represented in Fig.2.13. This figure shows a moderate agreement.
The reasons for the deviations will be discussed in the following sections.

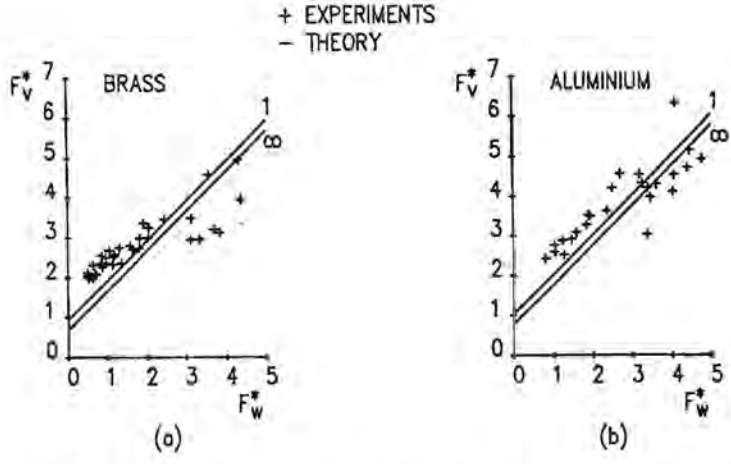

Fig.2.13. The cutting force number versus the friction force number without any correction.

2.5.1 The energy consumed in the separation and burnishing process

In the model, the assumption is made that the total supplied energy is consumed in the primary and secondary shear zone only and, that the energy dissipated in the separation process and the burnishing process can be neglected. This assumption may not be true.
The energy required for the separation process can be determined from the surface energy (T) of the materials. The energy required to create two surfaces per unit chip volume is:

$$u_s = \frac{2.T.v.b}{v.b.f} = \frac{2.T}{f} \qquad (2.36)$$

The value of T for most materials is about 3 J/m^2 and in diamond turning the feed (f) should be replaced by the equivalent chip thickness (f_e), which ranges from 0.2 to 7μm for the conditions considered. Hence the surface energy per unit chip volume for the separation process will range from about $9*10^5$ to $3*10^7$ J/m^3. This is small with respect to the total energy per unit chip volume, of which the magnitude of order is 10^9 J/m^3, so the energy for the surface energy can be neglected.
The energy dissipated in the burnishing process depends upon the forces on the clearance face. These will be discussed in the following sections.

2.5.1.1 The nose forces

If the tool edge is infinitely sharp, the forces on the clearance face and thus the energy dissipated in the burnishing process will be small. However, tool edges in practice are not perfectly sharp and even if they are, a rapid breakdown will cause a certain dullness of the edge.

This blunting of the edge is generally defined in terms of the radius of the tiny cylindrical surface connecting the rake and the flank face surfaces [2.9], [2.15], [2.28-2.29] and the extra forces on the tool nose can be estimated by means of an extrusion-like model as proposed by Abdelmoneim and Scrutton [2.15].

This model is based on the following assumptions (See Fig.2.14):

1. There is a stagnation point at which the work-piece material divides into two parts,namely that part which flows above this point and is removed in the form of a chip and, that part which flows beneath this point and subsequently beneath the base of the tool.
2. The work-piece material beneath the stagnation point is subjected to a rubbing action and a plastic region of circular shape exists beneath the tool base.
3. The work-piece material is ideal rigid plastic and a small, stable built-up is formed in front of the edge.
4. Sticking friction conditions will prevail at the tool edge.

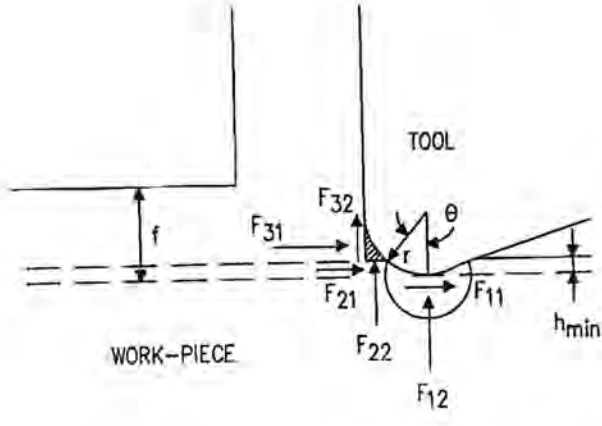

Fig.2.14. The extra forces at the tip of a blunt tool.

With these assumptions the extra forces will consist of three parts (Fig.2.14), namely part:

1. associated with the rubbing action at the tool base (F_{11} and F_{12}),
2. resulting from the rubbing of the workpiece over the lower surface of the dead-metal zone (F_{21} and F_{22}) and
3. due to the chip sliding over the dead-metal zone (F_{31} and F_{32}).

The following relationships are derived by Abdelmoneim and Scrutton:

- part 1

$$F_{11} = r.b_{ce}.\tau(2.\theta+\pi.\sin^2\theta)/\cos\theta \qquad (2.37)$$

$$F_{12} = 2.r.b_{ce}.\sigma.\sin\theta \qquad (2.38)$$

where r = the radius of the tool edge
b_{ce} = the width of contact between the work-piece and the tool edge
σ = the flow stress
τ = the shear stress
θ = the stagnation point angle

- part 2

$$F_{21} = r.b_{ce}.\tau(1-\sin\theta) \qquad (2.39)$$

$$F_{22} = r.b_{ce}.\sigma(1-\sin\theta) \qquad (2.40)$$

- part 3

$$F_{31} = r.b_{ce}.\sigma.\cos\theta \qquad (2.41)$$

$$F_{32} = r.b_{ce}.\tau.\cos\theta \qquad (2.42)$$

The extra friction force and cutting force will be:

$$\Delta F_w = F_{12} + F_{22} + F_{32} \qquad (2.43)$$

$$\Delta F_v = F_{11} + F_{21} + F_{31} \qquad (2.44)$$

The problems in applying these formulas are the difficulties associated with the measurement of the edge radius, the flow stress and the stagnation point angle. Nevertheless, the order of magnitude and thus the importancy of the nose forces can be determined by substituting some feasible values in the equations.
A value of 0.2 μm can be used for the radius of the tool edge, since this is the tolerance for the tool edge, and several investigations [2.29 - 2.30] showed that the stagnation point angle is about 15^{o}.
The flow stress is assumed to be the same as the effective flow stress in region 1 of the cutting model (σ = 750 N/mm^2 for brass and σ = 500 N/mm^2 for aluminium) and the shear stress is equal to $\sigma/\sqrt{3}$ (von Mises). If the feed f = 10 μm/rev, the depth of cut b = 10 μm and the tool radius R = 0.5 mm, then the width of contact between the work-piece and the tool edge b_{ce} = 105 μm.
The extra forces are :
ΔF_v = 19 mN for aluminium and 29 mN for brass and
ΔF_w = 19 mN for aluminium and 30 mN for brass.
The forces measured are:
F_v = 120 mN for aluminium and 150 mN for brass and
F_w = 80 mN for aluminium and 90 mN for brass.
It is clear, that the extra forces can be more than 15% of the measured forces and thus may not be neglected.

2.5.1.2 Extra forces due to flank wear

Another phenomenon, which increases the forces on the clearance face, is the flank wear of the tool (Fig.2.15).
A rapid increase of forces, especially for aluminium, is to be seen in Fig.2.16, which shows the forces as functions of the cutting time. This increase is mainly due to flank wear (Fig.2.17).
If the cutting time for one tool is longer than 30 minutes, as is in the experiments for evaluating the cutting model, the influence of the forces on the clearance face will be considerable.

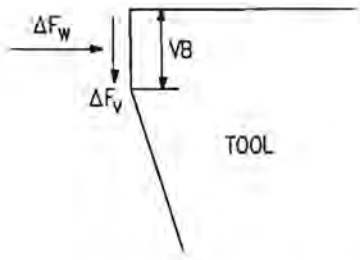

Fig.2.15. The extra forces due to flank wear.

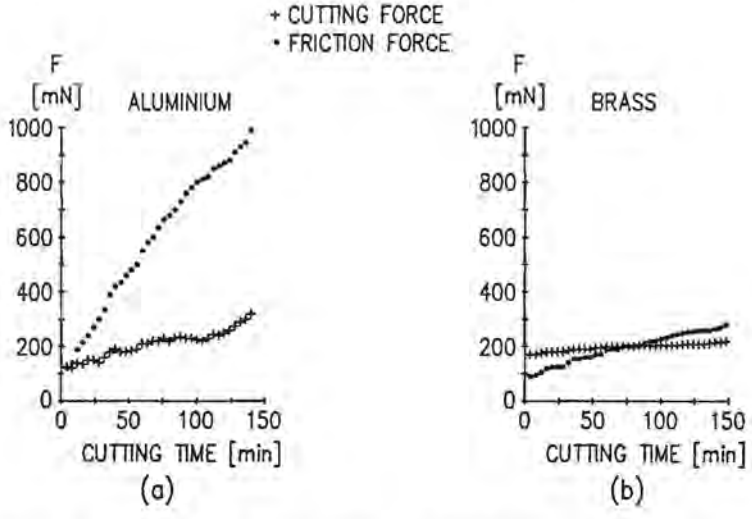

Fig.2.16. The cutting forces versus the cutting time.

A B

Fig.2.17. Secondary electron images of the diamond tool after 150 minutes cutting of (A) aluminium and (B) brass.

A rough approximation of the forces on the clearance face due to flank wear can be made by means of a simple model which is based on the following assumptions:

1. The flank wear land is parallel to the cutting direction and
2. The normal stresses on the clearance face are uniform and equal to the effective flow stress in region 1 of the cutting model.

With these assumptions the forces on the clearance face will be:

$$\Delta F_w = A_{VB} . \sigma \qquad (2.45)$$

$$\Delta F_v = \mu_f . A_{VB} . \sigma \qquad (2.46)$$

where σ = the flow stress

A_{VB} = the area of contact between work-piece and the flank wear land

μ_f = the mean coefficient of friction between the tool and the workpiece at the flank face.

Figs.2.16a and 2.17a will be considered for evaluating the model. The width of contact between the tool and the work-piece (b_{ce}) was 105 μm and the width of the flank wear land after 150 minutes of cutting aluminium was about 7 μm, so A_{VB} was about 735 μm^2. With a flow stress of 500 N/mm^2 the extra friction force ΔF_w would be about 370 mN. However, Fig.2.16a shows that the extra friction force was about 900 mN. As it is unlikely that the real area of contact between the tool and the work-piece is more than twice the above mentioned value, the assumption that the flow stress is equal to 500 N/mm^2 is not true. There are several reasons for this deviation and these will be discussed in the following section.

2.5.2 Material properties

a The material parameters were determined in tensile tests at room temperature and at low strain rates (of order 10^{-3}/s). Besides an enhanced temperature, there is also a very high strain rate (of order 10^6/s) in micro-cutting.
Contrary to the temperature rise, a higher strain rate increases the yield stress. Since the strain rate is very high, the total effect will be a higher yield stress, a higher C-value and a smaller n-value, too.

b It is assumed that the pre-deformation of the work-piece is zero. As the work-pieces had not been heat-treated, the materials had a certain strain history.
For a strain history $\bar{\varepsilon}_o$ Eq.(2.13) becomes:

$$\bar{\sigma} = C(\bar{\varepsilon}_o + \bar{\varepsilon})^n \qquad (2.47)$$

This means an increase of the flow stress.

From these two facts, it can be concluded that the flow stress should be higher than that determined in tensile tests.

2.5.3 Corrections for tool wear and material properties

If the measured forces are corrected for the forces on the clearance face, the experimental data fit very well to a line which is parallel to the theoretical lines (Fig.2.18). And, using C-values which are more than double - factor 2.3 for brass and factor 2.4 for aluminium - the values obtained from tensile tests, results even in an excellent agreement between the experimental data and the theory (Fig.2.19).

In order to correct for the tool wear, the experiments have been carried out in a sequence of continually increasing contact width b_{ce}.

The increase of the forces due to tool wear of one measuring cycle is approximated by the difference between the forces measured in the last and in the first section of the testpiece (ΔF_i in Fig.2.20). The correction for each measuring cycle is the sum of extra forces of the preceding measuring cycles (ΔF_{tot_i} for cycle i+1).

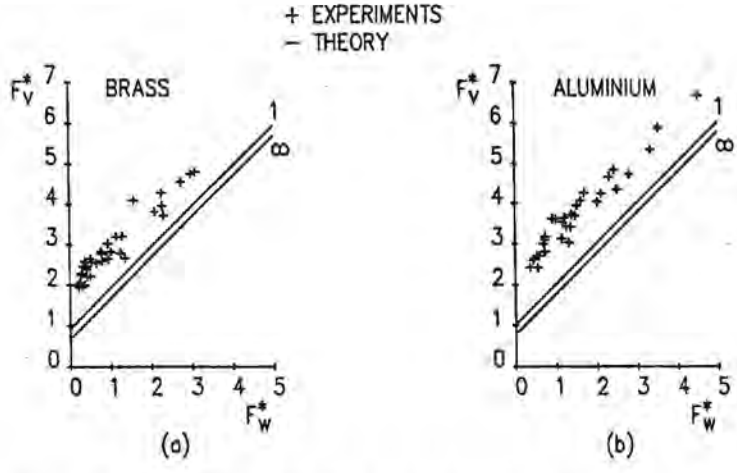

Fig.2.18. The cutting force number versus the friction force number corrected for only tool wear.

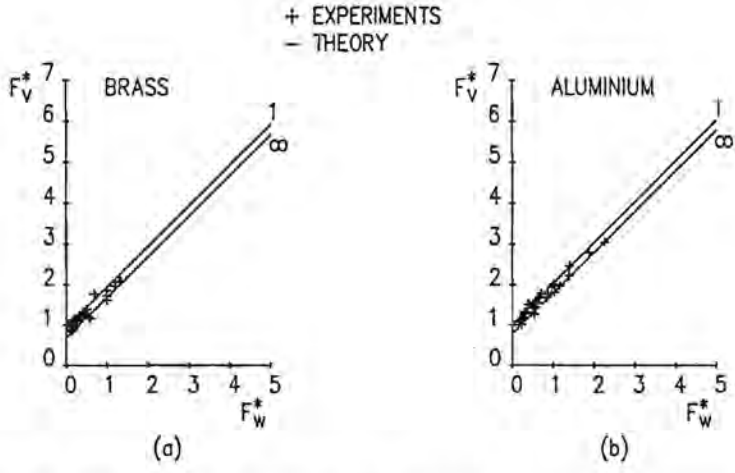

Fig.2.19. The cutting force number versus the friction force number corrected for tool wear and specific stresses.

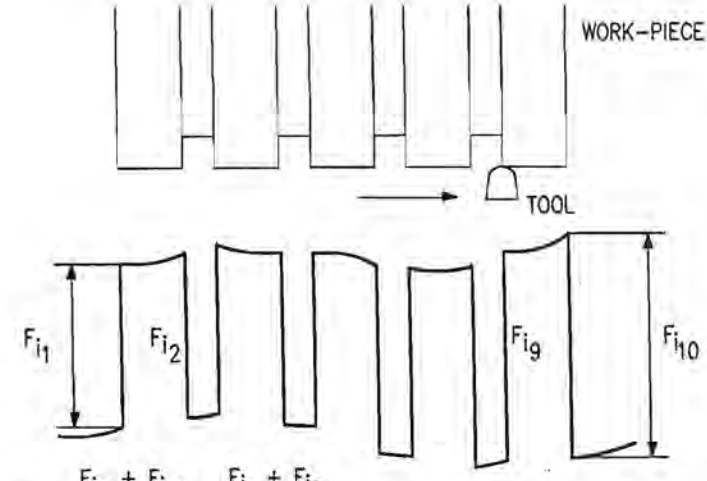

Fig.2.20. The increase of the forces due to tool wear during one measuring cycle.

Lacking the facilities to measure the material properties at very high strain rates, the C-values cannot be verified; but if a flow stress is used, which is more than double the early mentioned value of 500 N/mm^2, the simple model will give good approximations of the forces due to tool wear. Taking into consideration, the results of other investigations [2.31-2.32], it may concluded that a C-value which is twice or more than that obtained from a tensile test is not improbable.

A decrease of the n-value results in an upward parallel shift of the theoretical lines.
The equations for the theoretical lines are:

for brass: $F_v^* = F_w^* + 0.93 \quad (n_s = 1)$ (2.48)

$F_v^* = F_w^* + 0.68 \quad (n_s = \infty)$ (2.49)

for aluminium: $F_v^* = F_w^* + 1.03 \quad (n_s = 1)$ (2.50)

$F_v^* = F_w^* + 0.78 \quad (n_s = \infty)$ (2.51)

If the n-value is zero, the theoretical relationships are:

$F_v^* = F_w^* + 1.15 \quad (n_s = 1)$ (2.52)

$F_v^* = F_w^* + 0.91 \quad (n_s = \infty)$ (2.53)

An upward shift of 0.23 for brass and 0.13 for aluminium.
This means that a smaller C-value is needed in order to give good agreement between experimental results and theory (factor 1.8 for brass and 2.1 for aluminium).

2.5.4 The force relationships

The relationship $F_v^* = F_w^* + E_0^*$ is not sufficient for predicting the cutting forces, because there are two unknown variables, while only one equation is available.
A second equation is:

$$F_w^* = \mu_r . F_v^* \qquad (2.54)$$

where μ_r = the mean coefficient of friction between the tool and the work-piece on the rake face.

Fig.2.19 shows that the mean friction coefficient is not constant. However, a lot of the experimental data can be described with a constant friction coefficient, especially those for brass.
The variations can be imputed to the following errors:

- The variation in the cutting forces can be more than 20% due to variation of the feed and the depth of cut, so the corrections for tool wear may not be exact.
- Due to the difficulties associated with the measurement of the radius of the cutting edge and the stagnation point angle, a reliable estimation of the nose forces cannot be made.
  As discussed earlier, these forces cannot be neglected and will be very important if the feed and thus the chip thickness are small.
  In Fig.2.19, the results at smaller feed rates are represented by the points with high values and especially these points are exceptions to the concept of a constant friction coefficient.
  Subtraction of the nose forces, estimated with the model of Abdelmoneim, results in a downward shift of the points parallel to the theoretical lines, as the extra friction force, ΔF_w, and the extra cutting force, ΔF_v, are nearly equal.
  If a constant value for the radius of the cutting edge is used, the correction for the higher values will be larger than that for the lower values, so the points will approach a certain point.

- Every set of measurements with a new tool starts with a touch of the work-piece in order to create a reference for the next cuts. The increase of the forces during this touch can be significant due to a rapid breakdown of the tool edge, but no correction was made for it.
- As the strain rate depends upon the chip thickness and the range of the equivalent chip thickness for the conditions considered is relatively large (0.2 - 7.0 μm), the assumption that the specific stress is constant is doubtful.

Nevertheless, most of the results can be described by a constant coefficient of friction and, since the cutting conditions in single-point diamond turning are mainly restricted to high cutting speeds and a single rake angle (γ=0), the variation of the value of the coefficient of friction will be small.
The strain hardening exponent will be small at high cutting speed and the term E_o^* will approach 1. Then, the cutting forces on the rake face can be approximated with the simple relationships:

$$F_v^* = F_w^* + 1 \tag{2.55}$$

$$F_w^* = \mu_r . F_v^* \tag{2.54}$$

These can be transformed in:

$$F_v = \frac{1}{1-\mu_r} . C.A \tag{2.56}$$

$$F_w = \frac{\mu_r}{1-\mu_r} . C.A \tag{2.57}$$

The forces on the clearance face will depend mainly upon the forces due to flank wear and can be approximated with Eqs (2.44) and (2.45).

$$\Delta F_w = A_{VB}.\sigma \tag{2.45}$$

$$\Delta F_v = \mu_f.A_{VB}.\sigma \tag{2.46}$$

With the assumptions that the flow stress at the clearance face is equal to the flow stress in region 1 and that the strain hardening exponent is very small, the flow stress σ can be replaced by the specific stress C.

Consequently, the relationships for estimating the cutting forces will be:

$$F_w' = F_w + \Delta F_w = \frac{\mu_r}{1-\mu_r}.C.A + A_{VB}.C \tag{2.58}$$

$$F_v' = F_v + \Delta F_v = \frac{1}{1-\mu_r}.C.A + \mu_f.A_{VB}.C \tag{2.59}$$

An indication of the accuracy of the forces estimated with these equations is given in table 2.3, where the C-values are about double - factor 2.1 for aluminium and factor 1.8 for brass - the values obtained from the tensile tests (See section 2.5.3). The value of the friction coefficient at the rake face (μ_r) is determined from the points with low values in Fig.2.19. These points represent the dimensionless forces at high feed rates, where the influence of forces at the flank face is small. The value of the friction coefficient at the flank face is derived from Fig.2.16:

$$\mu_f = \frac{F_{v2_m} - F_{v1_m}}{F_{w2_m} - F_{w1_m}} \tag{2.60}$$

where: F_{v1_m} = cutting force at the beginning of the test

F_{v2_m} = cutting force at cutting time ≈ 150 minutes

F_{w1_m} = friction force at the beginning of the test

F_{w2_m} = friction force at cutting time ≈ 150 minutes

The width of flank wear land (VB) after 150 minutes cutting is approximated by means of a secondary electron image of the tool (Fig.2.17).

Table 2.3. The measured (m) forces at the beginning and at the end of the tests and the calculated (c) forces.

Cutting time ≈ 0.

Material	C N/mm^2	μ_r -	A μm^2	F_{w1_m} mN	F_{w1_c} mN	F_{v1_m} mN	F_{v1_c} mN
Brass	1350	0.15	100	85	24	170	159
Aluminium	1020	0.20	100	90	26	125	127

Cutting time ≈ 150 minutes.

Material	μ_f -	VB μm	b_{ce} μm	A_{VB} μm^2	F_{w2_m} mN	F_{w2_c} mN	F_{v2_m} mN	F_{v2_c} mN
Brass	0.15	2.0	105	210	290	308	205	201
Aluminium	0.20	7.0	105	735	950	776	300	277

It can be seen that the difference between the first measured (F_{wl_m}) and calculated friction force (F_{wl_c}) is considerable. This is mainly due to the bluntness of the cutting edge, already present before the tests, and the rapid breakdown of the cutting edge during the first touch of the work-piece in order to create a reference for the following cuts. The extra forces, due to this blunting of the cutting edge, were not taken into account, because of lack of facility for accurate measurements of tool wear less than 0.5 μm.
However, a tool wear (VB) of 0.5 μm will give additional friction forces of more than 50 mN for a contact width (b_{ce}) of 105 μm. Omitting this tool wear will result in large errors in the estimations of the friction force.
Another cause of extra forces on the clearance face is the elastic recovery of the work-piece material behind the cutting edge. This spring-back increases the contact area between the tool and the work-piece and hence, the cutting forces, especially the friction force. A small spring-back of 10 nm will increase the contact length by 0.1 μm and if the contact width is 105 μm, the extra contact area is 10.5 μm. The additional friction force will depend on the stress distribution on the extra contact area and can be 10 mN.
It may be clear, that the friction force cannot be predicted well, if the forces on the clearance are not taken into account.
On the contrary, the cutting forces can be estimated within 10%, which is rather good, especially when taking into consideration the fact, that the values for the friction coefficients and the specific stresses are just rough approximations. As the extra force on the clearance face with respect to the cutting force is relatively small, it is not surprising that the cutting force is well-estimated.
The forces after 150 minutes cutting are estimated within 20%, for brass even within 7%. The difference between estimated and measured values may be caused by errors in the determination of the tool wear (VB), which is not constant along the contact width b_{ce}. The values used are just rough approximations of the mean value.

2.6 Concluding remarks

1. The difference between the relationship of dimensionless forces of the model of Dautzenberg and that of Lee and Shaffer is relatively small. On the contrary, the difference is large, if the model of Dautzenberg is compared to that of Merchant.
2. Because the assumptions of Dautzenberg are the least objectionable, his model is regarded as the best to start with.
3. With only a few modifications the force relationship which has been derived for orthogonal cutting may be used for single-point diamond turning, which is a non-orthogonal process.
4. The surface energy per unit chip volume for the separation process is small with respect to the total energy per unit chip volume and can be neglected
5. The forces on the clearance face may not be neglected. Additional forces due to the blunting of the cutting edge may be more than 15% of the total forces and, due to flank wear even more than 50% of the total forces
6. The influence of the strain rate upon the material properties, namely the specific stress (C) and the strain hardening exponent (n), is considerable. The value of the specific stress in single-point diamond turning is about double the value obtained from a tensile test.
7. The cutting forces can be approximated by means of the simple relationships:

$$F_w' = F_w + \Delta F_w = \frac{\mu_r}{1-\mu_r}.C.A + A_{VB}.C \qquad (2.58)$$

$$F_v' = F_v + \Delta F_v = \frac{1}{1-\mu_r}.C.A + \mu_f.A_{VB}.C \qquad (2.59)$$

The accuracy of the estimations will depend upon the accuracy of values used for the parameters involved, namely the friction coefficient at the rake face (μ_r) and at the flank face (μ_f), the specific stress (C) and the area of contact between the work-piece and the tool at the flank face (A_{VB}), and can be better than 20%.

References

2.1. Piispanen, V.:
Lastunmuodostumisen Teoriaa.
Teknillen Aikakauslehti,27,1937,p.315-322.

2.2. Merchant, M.E.:
Mechanics of the metal-cutting process.
Journal of the Applied Physics,16,1945,p.267-318.

2.3. Lee, E.H.; Shaffer, B.W.:
The theory of plasticity applied to a problem of machining.
ASME Journal of Applied Mechanics,73,1951,p.405-413.

2.4. Stabler, G.V.:
The fundamental geometry of cutting tools.
Proc. Inst. Mech. Eng.,165,1951,p.14-21.

2.5. Shaw, M.C.; Cook, N.H.; Finnie, I.:
The shear angle relationship in metal cutting.
ASME Journal of Engineering for Industry,75B,1953,p.273-288.

2.6. Hill, R.:
The mechanism of machining: a new approach.
Journal of the mechanics and physics of solids,3,1954,p.47-53.

2.7. Okushima, K.; Hitomi, K.:
An analysis of the mechanism of orthogonal cutting and its application to discontinuous chip formation.
ASME Journal of Engineering for Industry,20B,1958,p.95-116.

2.8. Palmer, W.B.; Oxley, P.L.B.:
Mechanics of orthogonal machining.
Proc. Inst. Mech. Engrs.,173,1959,p.623-654.

2.9. Albrecht, P.:
A new development in the theory of the metal cutting process
- part 1 - The ploughing process in metal cutting.
ASME Journal of Engineering for Industry,82B,1960,p.348-358.

2.10. Kobayashi, S.; Thomsen, E.G.:
Metal cutting analysis I and II.
ASME Journal of Engineering for Industry,84B,1962,p.63-80.

2.11. Zorev, N.N.:
Metal cutting mechanics.
Oxford, Pergamon Press,1966.

2.12. Time, I.A.:
Resistance of metals and wood to cutting (Soprotivleniye metallov i dereva rezaniyu).
1870, Reference no.1 in [2.11].

2.13. Rowe, G.W.; Spick, P.T.:
A new approach to determination of the shear plane angle in machining.
ASME Journal of Engineering for Industry,89B,1967,p.530-538.

2.14. Spaans, C.:
An exact method to determine the forces on the clearance face.
Annals of the CIRP,15,1967,p.463-469.

2.15. Abdelmoneim, M.E.; Scrutton, R.F.:
Tool edge roundness and stable build-up formation in finish machining.
ASME Journal of Engineering for Industry,96B,1974,p.1258-1267.

2.16. Williams, J.E.:
Some aspects of a three zone model of machining.
Wear,48,1978,p.55-71.

2.17. Dautzenberg, J.H.; Vosmer, J.:
Cutting force relations for an arbitrary deformation model.
Proc. 2nd Conf. Irish Manufacturing Committee (Ireland),1985,
p.207-218.

2.18. Vosmer, J.
Een verspaningsmodel op basis van een vermogensbalans. (Dutch).
WPB-report,No.0019,1983.

2.19. Lo-A-Foe, T.C.G.; Dautzenberg, J.H.; van der Wolf, A.C.H.:
A model for the micro-cutting forces of non-ferrous metals.
Proc. 5th Polytechnics Symp. on Manufacturing Engineering
(Eastbourne),1986,p.346-362.

2.20. De Chiffre, L.; Wanheim, T.:
What can we do about chip formation mechanics?
Annals of the CIRP,34,1985,p.129-132.

2.21. Armarego, E.J.A.; Brown, R.H.:
The machining of metals.
New Jersey,Prentice-Hall,Inc.,1969.

2.22. Shaw, M.C.:
Metal cutting principles.
Oxford,Clarendon press,1984.

2.23. Santhanam, S.; Shaw, M.C.:
Flow characteristic for the complex stress state in metal
cutting.
Annals of the CIRP,34,1985,p.109-111.

2.24. Banerjee, S.K.:
The limit of continuity in some single phase materials during machining and its correlation with torsion testing.
Development of Production Systems, Proc. 2nd ICPR, 1974, p.89-110;

2.25. Fenton, R.G.; Oxley, P.L.B.:
Mechanics of orthogonal machining allowing for the effect of strain rate and temperature on tool-chip friction.
Proc. Inst. Mech. Engrs, 183(22), 1968-1969, p.417-438;

2.26. Dewhurst, P.:
Is the machining process uniquely defined?
Annals of the CIRP, 27/11, 1978, p.1-4.

2.27. Young, H.T.; Mathew, P.; Oxley, P.L.B.:
Allowing for nose radius effects in predicting the chip flow direction and cutting forces in bar turning.
Proc. Inst. Mech. Engrs, 202, no.C3, 1987, p.213-226.

2.28. Palmer, W.B.; Yeo, R.C.K.:
Metal flow near the tool point during orthogonal cutting with a blunt tool.
Proc. 4th MTDR Conference, 1963, p.61-71.

2.29. Connolly, R.; Rubenstein, C.:
The mechanics of continuous chip formation in orthogonal cutting.
Int. J. Mach. Tool Des. Res., 8, 1968, p.159-187.

2.30. Komanduri, R.:
Some aspects of machining with negative rake angle tools simulating grinding.
Int. J. Mach. Tool Des. Res., 11, 1971, p.223

2.31. Oxley, P.L.B.; Stevenson, M.G.:
Measuring stress/strain properties at very high strain rates using a machining test.
Journal of the Institute of Metals,95,1967,p.308-313.

2.32. Dowling, A.R.; Harding, J.; Campbell, J.D.:
The dynamic punching of metals.
Journal of the Institute of Metals,98,1970,p.215-224.

3 The dynamic behaviour of the lathe

3.1 Introduction

An important parameter in the surface generation is the behaviour of the lathe. A desired geometry of the work-piece can be obtained by setting the appropriate operational conditions. However, deviations from this geometry may arise due to forced vibrations, geometric and thermally-induced errors of the machine elements and cutting forces. Dimensional errors of the machine tools can be reduced by (a) increasing the precision of the components, (b) using materials with a low thermal expansion coefficient, (c) eliminating residual inaccuracies in the materials and (d) an optimal assembly of the components.

The deviations due to forced vibrations, cutting forces and their variations may be reduced by (a) eliminating or reducing the exciting forces, (b) avoiding the coincidence of frequencies of exciting forces and natural frequencies of the machine tools and (c) increasing the stiffness and the damping of the elements. For this it is necessary to know the sources, amplitudes and frequencies of the vibrations as well as the properties of the elements.

A precision lathe is usually composed of a spindle with hydro- or aero-static bearings, one or two slide systems, a drive system including the motor, an oil and/or air supply system and a tool holder.

Forces are excited in (a) the drive system by unbalance of the motor and errors in the adjustment of motor to shaft of the spindle, (b) the oil or air supply system (pump ripple), (c) the foundations and (d) the cutting process. The transfer of these forces to the position of the tool and the work-piece will depend on the properties of the machine elements. These can be represented by a transfer function which shows the natural frequencies, the dynamic stiffnesses and the damping of the components.

If the amplitude and the frequency of the exciting forces and the transfer function of the components are known, then the deviations from the desired geometry can be determined. If these deviations exceed the tolerances - which is frequently the case nowadays, due to the rapid succession of upgradings of the requirements -, then the amplitude of the exciting forces should be reduced and/or the stiffness and damping of the components should be increased. Usually, it is not necessary to improve the properties of all the elements. Only the weak elements should be replaced by elements with a higher stiffness and/or damping. However, this cannot always be done, due to limitations of material properties and/or dimensions of the elements. Then further improvement of the behaviour of the machine should be achieved by optimizing the assembly of the components. It can be done by trial-and-error, but this is very time consuming and rather expensive. It is more efficient to do this by means of reliable numerical models.

A convenient expedient for determining the behaviour of the machine is modal analysis. Therefore, this method will be used for determining the weak elements in the available precision lathe. The components of this lathe will be described in the next section. The experimental set-up and results of the modal analysis will be discussed in section 3.3. In section 3.4, the attention will be directed to the displacements of the tool relative to the work-piece due to potential forced vibrations. The weak components will be considered and modifications in order to improve their dynamic behaviour will be looked for by means of a numerical model (section 3.5).

3.2 The precision lathe

The main components of the lathe (Fig.3.1), which is constructed at the Philips Centre for manufacturing Technology, are a spindle, a carriage, a motor and an oil supply system. Further details of these will be given in the next sections.

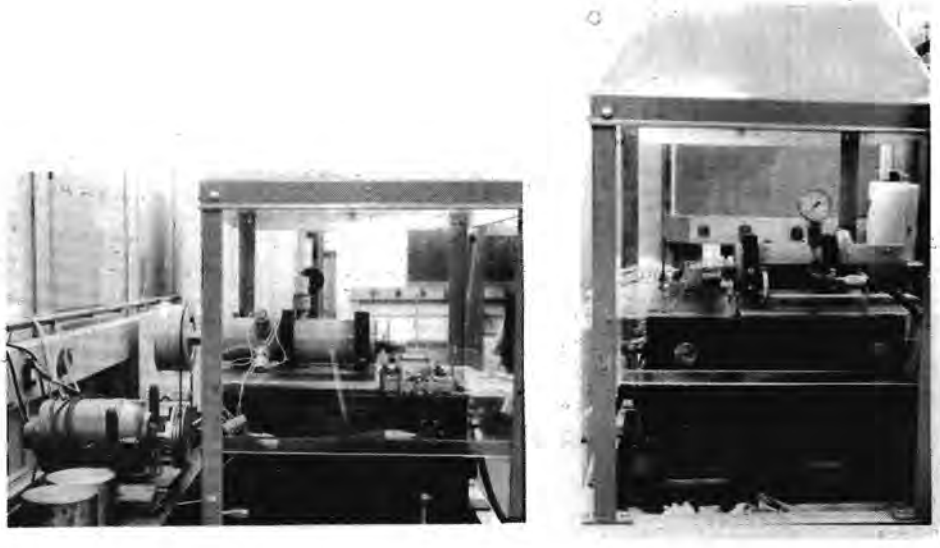

Fig.3.1. The precision lathe.

3.2.1 The spindle

The spindle is a hydraulic unit with a shaft, three hydrostatic bearings (two radial and one thrust) and a cylinder (Fig.3.2). It is mounted on a base which is fixed on an oil reservoir. This reservoir is also the base for the carriage. A pulley is fixed on the backside of the shaft and is rotated by a DC-motor via two belts. The shaft can also make a controlled hydraulic travel, of which the speed is adjusted by means of valves on the backside of the cylinder and the direction is controlled by a few electromagnetic valves on the cylinder.

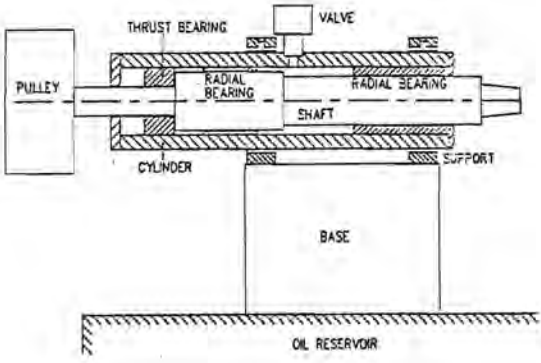

Fig.3.2. The spindle of the lathe.

3.2.2 The carriage

The carriage (Fig.3.3) consists of an active and a passive hydraulic unit, which are connected by two beams, on which a plate with the toolholder is mounted. It is connected to the oil reservoir with two clamps on the active and one joint on the passive unit. The structure is then statically determined. The active unit consists of a cylinder and a piston rod, which can be displaced by controlling the oil flow to one side of the cylinder with a control valve. The rotation of the rod of the active unit is suppressed by the passive unit.

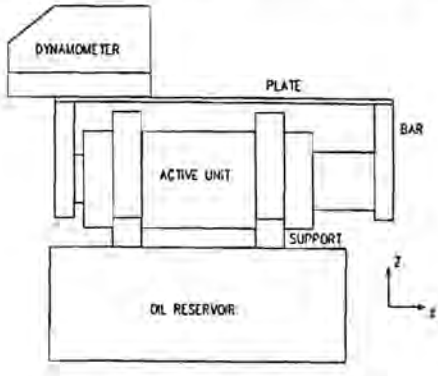

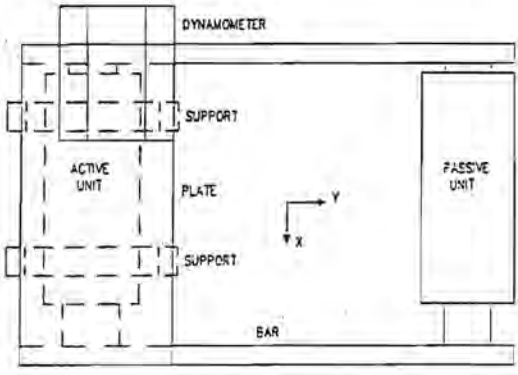

Fig.3.3. The carriage of the lathe.

3.2.3 The oil supply system

The oil supply system (Fig.3.4) comprises a motor, two pumps, a water cooling system and a reservoir. The supply lines are provided with filters against the contamination of the oil, accumulators for reducing the pressure ripples introduced by the pumps and pressure-relief valves to ensure that the operating pressure stays within the desired limits.

If there is a dangerous pressure drop in the supply lines, e.g. caused by leakage, the electric motor for driving the pumps and the motor for driving the shaft of the spindle are switched off by hydraulic switches.

Before the oil from the hydraulic units (spindle and carriage elements) returns back to the main reservoir, it is gathered in another reservoir at the base of the spindle and the carriage.

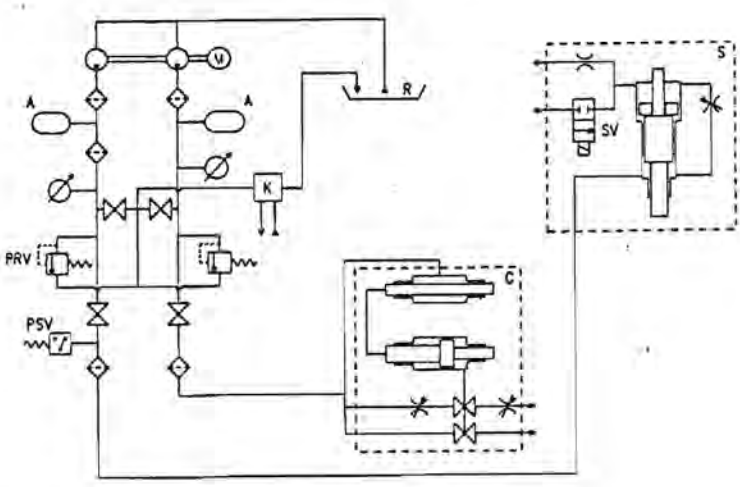

Fig.3.4. Diagram of the hydraulic system.
A accumulator. K water-cooling system. PRV pressure relief valve. PSV hydraulic swith. R oil reservoir. SV electro-magnetic control valve. C carriage. S spindle.

3.2.4 The driving system

The shaft of the spindle is driven by a DC-motor via belts. The range of the rotational speed of the motor is 0 to 3000 rpm.

The structural behaviour of this lathe has been determined by modal analysis. The experimental set-up and the results are discussed in the following section.

3.3 Modal analysis

Modal analysis refers to an experimental or analytical procedure for describing the behaviour of linear mechanical structures.
The analysis aims to define the basic deformation shapes, the so-called 'mode shapes', of a mechanical structure. Each of these basic patterns appears when exciting the structure at one of its natural frequencies.
Together with the other modal parameters, namely the natural frequencies and the damping coefficients, these shapes will determine the resulting deformation of the structure due to any kind of externally applied dynamic load. The relationships between the applied forces, the modal parameters and the resulting displacements are presented in the appendix A.1. A force at degree of freedom j of a linear structure with viscous damping will give a displacement at degree of freedom i according to the following equation:

$$x_i(i\omega) = H_{ij}(i\omega) * F_j(i\omega) = \sum_{k=1}^{n_d} \left[\frac{R_{k,ij}}{i\omega - p_k} + \frac{R^*_{k,ij}}{i\omega - p^*_k} \right] * F_j(i\omega) \quad (3.1)$$

where

$x_i(i\omega)$ = Fourier transform of displacement $x_i(t)$
$F_j(i\omega)$ = Fourier transform of force $F_j(t)$
$H_{ij}(i\omega)$ = transfer function of forces at freedom j to displacements at degree of freedom i, also referred to as frequency response
ω = angular velocity
n_d = number of degrees of freedom

$$R_{k,ij} = \frac{\Psi_{ik}\Psi_{jk}}{a_k} = \text{residue} \quad (3.2)$$

Ψ_{ik} = component i of mode vector Ψ_k
a_k = scaling constant

$$p_k = -\zeta_k\omega_k \pm \omega_k\sqrt{(\zeta_k^2 - 1)} = \text{pole} \quad (3.3)$$

ω_k = undamped eigenfrequency
ζ_k = damping ratio
The asterisk denotes the complex conjugate.

The equations show that the modal parameters can be determined from the frequency responses. This is the basis for the experimental modal analysis, of which the main activities are the measurement and the analysis of the frequency responses.
The experimental procedure for a modal analysis consists of the following steps, namely [3.1]:

1. The definition of the frequency range of interest and the grid of points to be measured on the structure.
2. Choice of the measuring equipment and set up of the measurements.
3. Input of the structure geometry in the computer.
4. Measurement and disk storage of the frequency responses.
5. Computation of the resonance frequencies and associated damping ratios.
6. Computation of the modal shapes.
7. Generation of the animated mode shape display.

Further details and the performance of these steps on the precision lathe will be given in the following sections.

3.3.1 The definition of the frequency range of interest

The frequency range of interest depends upon the frequencies of the forced vibrations in the motor, the foundation, the oil supply system and the cutting process.
The rotational speed of the motor ranges from 0 to 3000 rpm, so the range of 0 to 50 Hz should be considered.
The metal forming presses in the neighbourhood of the precision lathe may cause pulses with a range of a few hundred Hz.
The pump ripple in the oil supply system has a frequency of 480 Hz.
The frequencies of cutting force variations depend upon the surface topography and the structure of the work-piece, the feed velocity, the depth of cut and the rotational speed. The frequency range may be very large; for example, if an inclusion with a length of 1 micron is encountered during cutting with a cutting speed of 10 m/s, then a cutting force variation will occur with a duration of 0.1 μs and, thus a frequency range of 10 MHz.

But, the energy content of these variations will be small and, as mechanical systems tend to have much of their vibration energy contained in the relatively narrow range of 0 to a few KHz, the influence of force components at higher frequencies will be small. A preliminary examination showed that the frequency response will be small at frequencies above 1500 Hz (See Fig.3.5). Therefore, the attention will be restricted to frequencies less than 1500 Hz.

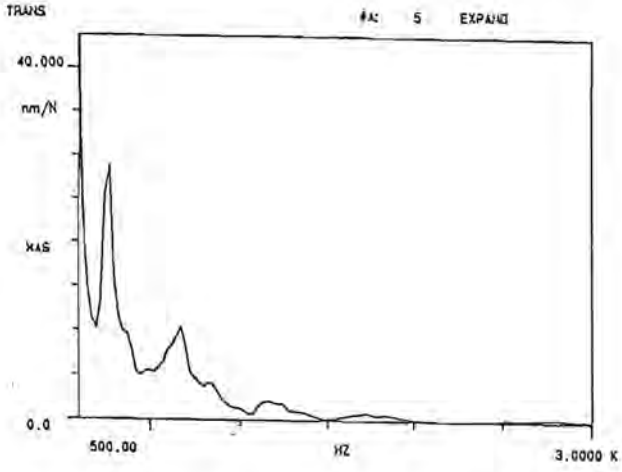

Fig.3.4. A transfer function of the lathe (typical example).

3.3.2 The grid of the points to be measured on the structure

There are no firm rules for the determination of the grid of points to be measured. If a large number of points is taken the measurements will be time consuming. However, if the measuring points are too far apart some important modes cannot be measured accurately. Therefore, the number of points is chosen to be as small as possible, but still sufficient for an accurate measurement of the modes which may have a significant influence upon the displacements of the tool and the work-piece.

The grid of points to be measured will also depend upon the accessibility to the points by the available devices for measuring the response or exciting the structure. Since it is not possible to put devices on some points of the complex structure of the precision lathe, a simplified geometry of the structure will be chosen. This geometry is depicted in Fig.3.6 and the separate components are shown separately in Fig.3.7.
The number of points to be measured is 72.

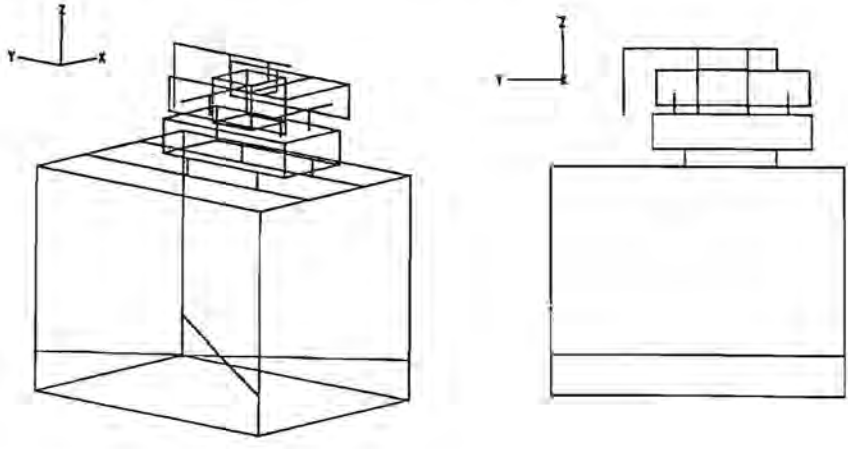

Fig.3.6. Geometric model of the lathe.

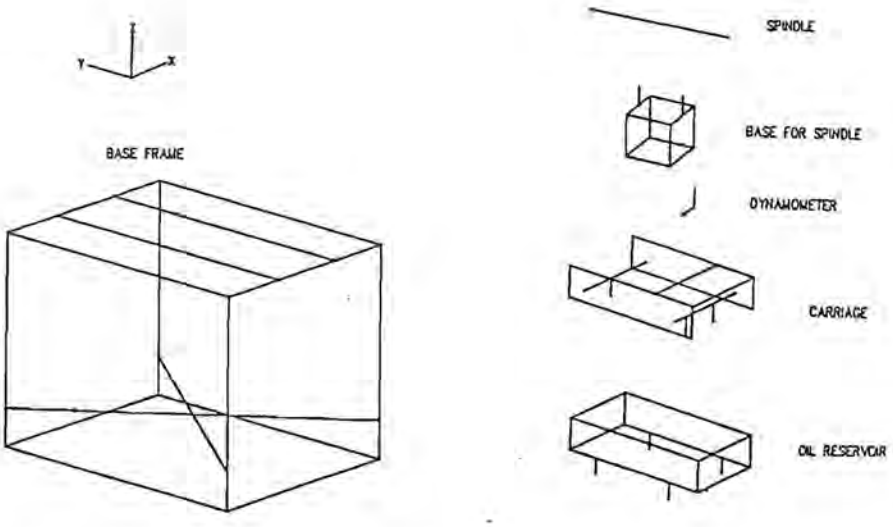

Fig.3.7. The components of the lathe.

3.3.3 The experimental set-up

The basic instrumentation for determining the frequency responses and the modal parameters consists of :

a. an exciter device,
b. measuring instruments,
c. an interface and
d. a computer.

3.3.3.1 The exciter device

The structure can be excited by means of a hammer or an electrodynamical or hydraulic shaker. The testing with a hammer has the advantage that the equipment requirements and the set-up and fixturing time are the least of all the testing methods. But, it has disadvantages too, which are caused by the pulse like nature of the input signal.

This signal has a high peak with a short duration and will overdrive the system while putting little total energy into it. As a result, non-linear response is exaggerated while the signal to noise ratio for the entire measurement is low.
Since the methods for estimating the modal parameters are based on the assumption that the system is linear, non-linear response will results in poor estimates of the modal parameters.
Despite of these disadvantages, a hammer has been used for the measurements because of the large number of points to be measured and the facts, that the available shakers do not fit between the points of most interest, namely the tool holder and the work-piece, and that the devices for measuring the responses cannot be fixed easily to all the points.
In order to obtain good results, much care should be taken in the set-up and procedure of the measurements. The first consideration is the choice of a proper impactor. The characteristics of the impactor determine the magnitude and the duration of the force pulse which, in turn, determine the magnitude and content of the pulse in the frequency domain. The two characteristics of most importance are the weight and the tip hardness. The frequency content of a pulse is inversely proportional to the weight of the impactor and proportional to the hardness of the tip. Since the weight also determines the magnitude of the force pulse, the impactor is usually chosen for its weight and then, the tip hardness is varied in order to achieve the desired pulse time duration. A hammer with a weight of about 0.5 kg and two tips with different hardness were chosen for the measurements. In order to restrict the non-linear effects, the magnitude of the pulse should be kept below a certain limit. If the magnitudes are equal, a pulse with a long duration will have a larger energy content than a short one (Figs.3.8 and 3.9). Hence, a soft tip will give a better signal-to-noise ratio. As this tip did not cover the whole frequency range of interest - the signal level at frequencies higher than 200 Hz will be too low (Fig.3.9a) -, a harder tip (Fig.3.9b) was used for measuring the responses at higher frequencies.

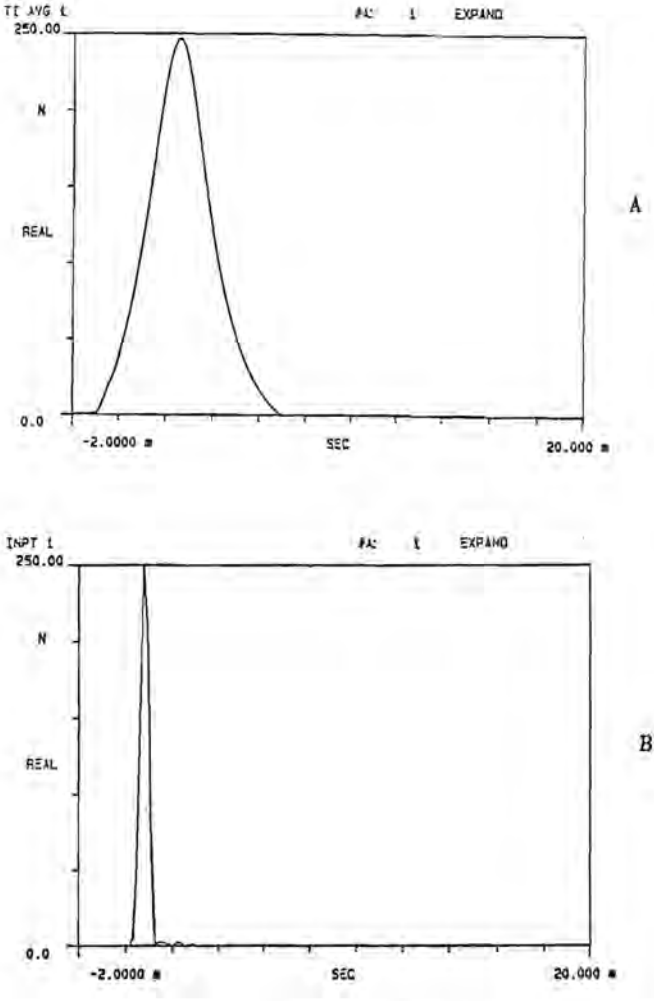

Fig.3.8. The impulse signals in time domain of a hammer with a soft tip (A) and with a hard tip (B).

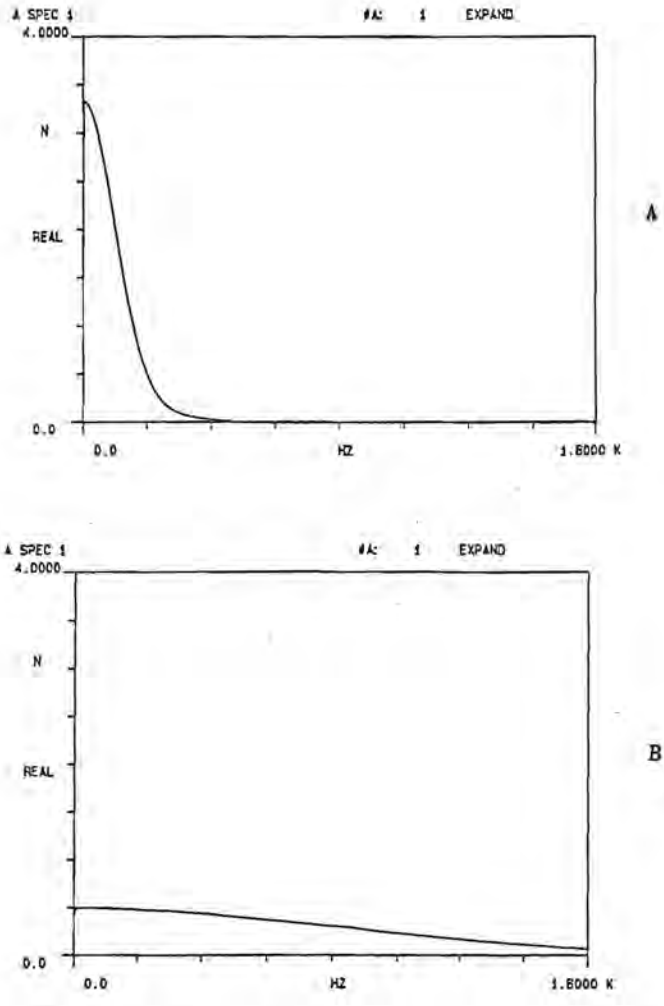

Fig.3.9. The impulse signals in frequency domain of a hammer with a soft tip (A) and with a hard tip (B).

3.3.3.2 The measurement transducers

At least two transducers are required to obtain calibrated frequency response measurements: a force transducer and a response transducer. A Kistler 9311 load cell with a sensitivity of 3.65 pC/N was used for transducing the forces. This cell was mounted between the hammer body and the hammer tip.
The responses were measured by a Brüel & Kjær 4381 accelerometer with a sensitivity of 10 pC/ms^{-2} and a frequency range of 10 KHz.

3.3.3.3 The amplifiers

The signals of the accelerometer and the load cell are amplified by Kistler 5007 charge amplifiers, which contain low-pass filters in order to prevent aliasing errors. Overload of signal is recognizable. This is important, because it is desirable to have the amplitude of the force and response signals as high as possible with respect to the input range of the equipment in order to minimize the noise to signal ratio, and variations in the impacting can frequently cause overloading. If this is not detected, then estimates of the frequency response will be poor.

3.3.3.4 The analysis system

A HP 5423A Structural Dynamics Analyzer [3.2], [3.3] has been used for analysing the signals. It consists of an input, a processing and a display section.
Both input channels have an amplifier with various ranges, in order to maximize signal strength into the Analog-to-Digital Convertor (ADC). The ranges are selected via keyboard entry. Before the signals are digitized, they will pass through anti-aliasing filters.

The processing section is a computer system for performing the subsequent data manipulations, such as:

a. Discrete finite Fourier transformations.
   The computational time for these is considerably reduced by a hardware implemented Fast Fourier Transform (FFT) [3.4].
b. Averaging, which reduces the noise-to-signal ratio.
c. Windowing.
   For impact testing, a force window for the input signal and an exponential window for the output signal can be used. The force window should garantee that the time record of the exciting force is just the impact with the structure and, that any stray signals, being noise or caused by movement of the hammer, after hitting the structure is ignored.
   The exponential window is useful when the structure is lightly damped and the response signal does not fully decay at the end of the time record.
   In this case, the signal is frequently not periodic in the time record and leakage will occur in the frequency response measurement. The exponential window reduces the signal at the end of the time record and, consequently, it minimizes the amount of leakage. It is also useful when the noise-level is high in case of a sufficiently damped structure.
d. Calculation of several functions in both time and frequency domain namely the auto and cross correlation and spectrum, the transfer and coherence function.
e. Computation of the modal parameters.
f. Mathematical operations, including differentiation and integration. These are useful in transforming displacements, velocities and accelerations.

3.3.3.5 The measurement states.

Table 3.1 and 3.2 show the settings for the measurements with a soft hammer tip and with a hard hammer tip, respectively.

Table 3.1. The measurement state for the measurements with a soft hammer tip.

MEASUREMENT :	TRANSFER FUNCTION
AVERAGE :	5 , STABLE
SIGNAL :	IMPACT , TM= 2, FM= 50.00 m
TRIGGER :	INTERNAL , CHNL 1

CENT FREQ :	0.0 HZ	ΔF :	390.625 mHZ
BANDWIDTH :	100.000 HZ		
TIME LENGTH :	2.56000 S	ΔT :	2.50000 mS

CHAN #	RANGE	AC/DC	DELAY	CAL (EU/V)
# 1	10 V	DC	-2.50000 mS	50.0000
# 2	1 V	DC	-2.50000 mS	5.00000

Table 3.2. The measurement state for the measurements with a hard hammer tip.

MEASUREMENT :	TRANSFER FUNCTION
AVERAGE :	5 , STABLE
SIGNAL :	IMPACT , TM= 2, FM= 10.00 m
TRIGGER :	INTERNAL , CHNL 1

CENT FREQ :	0.0 HZ	ΔF :	8.25000 HZ
BANDWIDTH :	1.80000 KHZ		
TIME LENGTH :	180.000 mS	ΔT :	158.250 µS

CHAN #	RANGE	AC/DC	DELAY	CAL (EU/V)
# 1	5 V	DC	-2.50000 mS	100.000
# 2	2.5 V	DC	-2.50000 mS	20.0000

In order to reduce noise, the number of averages is taken to be 5. A force window has been applied. However, the exponential window was omitted, because some modes were closely spaced and these modes would be coupled, if an exponential window would be applied. For example, it is difficult to distinquish the mode at 240.5 Hz in Fig.3.10a, since it is coupled to the mode at 259.7 Hz.

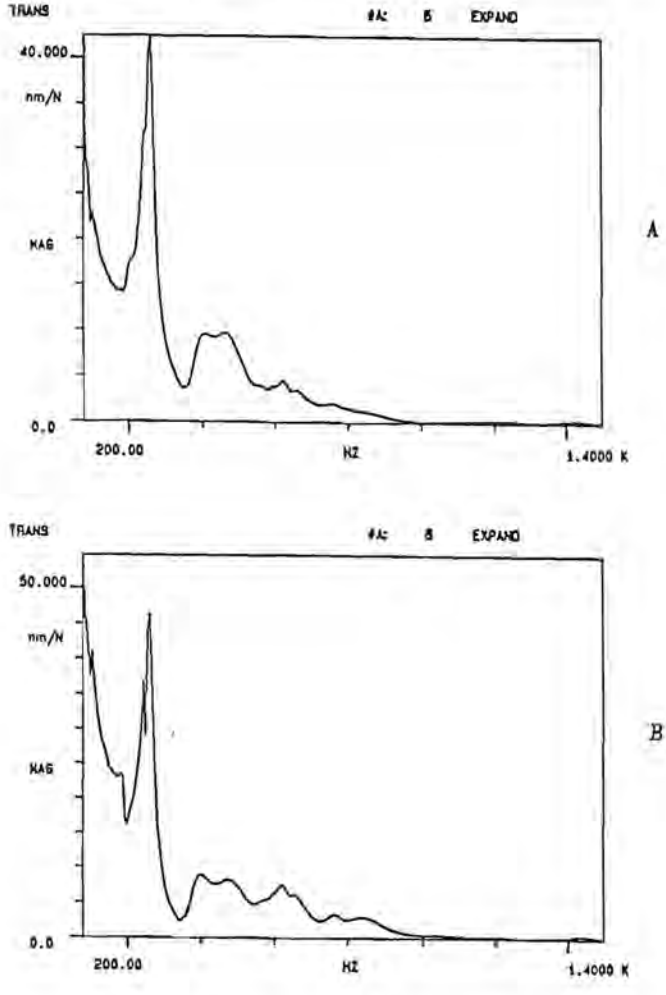

Fig.3.10. A transfer function of the lathe with application of an exponential window (A) and without application of the exponential window (B).

Besides, the response signals decayed substantially in the sampling window and the noise level is relatively low (Fig.3.11), too.

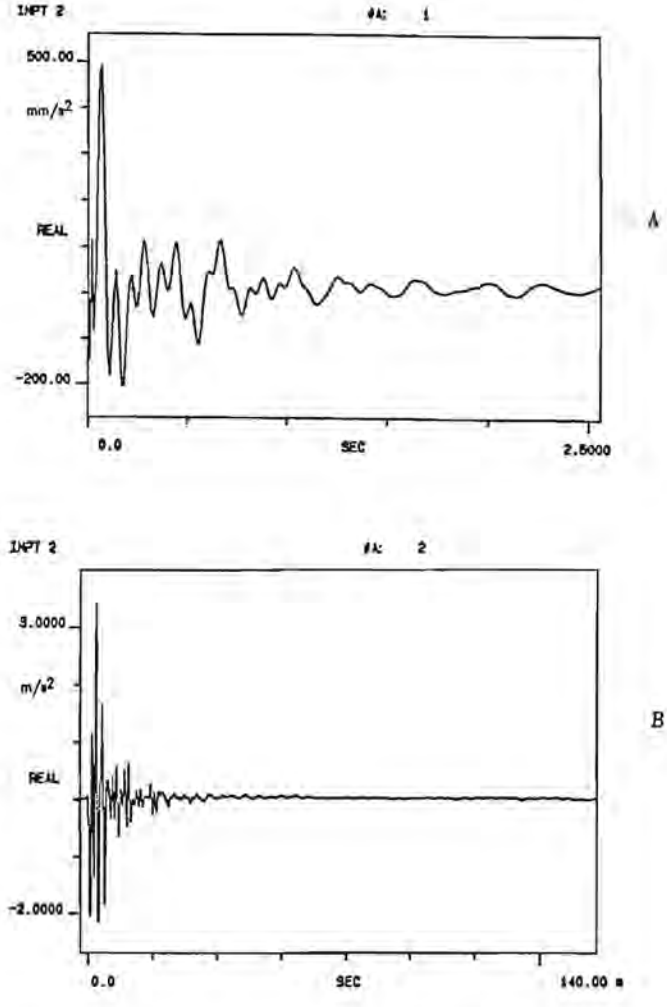

Fig.3.11. The response signals of the lathe after hitting with a soft tip (A) and with a hard tip (B).

The internal trigger mode ensures that data sampling begins at a pre-determined point, which can be selected in terms of voltage and slope. This is useful for impact testing as the data should be taken only when the input impuls is present. A pre-trigger delay is used to ensures that the leading edge is not missed.
As the resonance frequencies of the most important modes are less than 1600 Hz, the upper limit of the frequency range is chosen to be this frequency.
The ranges of the amplifiers (Range for the Analyzer and Cal for the charge amplifier) are selected in such a way that maximum signal-to-noise ratio is achieved without instrumentation overload.

3.3.4 Frequency responses

According to Eq.3.1 the frequency response or transfer function is defined as the ratio of the Fourier transform of the output on the transform of the input:

$$H(i\omega) = \frac{X(i\omega)}{F(i\omega)} \tag{3.4}$$

Instead of computing this ratio directly, the Analyzer determines first the crosspower spectrum between the input and the output (G_{XF}) and the autopower spectrum of the input (G_{FF}) and then calculates the ratio of these spectra:

$$H(i\omega) = \frac{X(i\omega)F^{*}(i\omega)}{F(i\omega)F^{*}(i\omega)} \tag{3.5}$$

where * denotes the complex conjugate.
The advantage of this form can be seen by considering the practical measurement situation illustrated in Fig.3.12, where M and N represent the noise at the input and output measurement point, respectively.

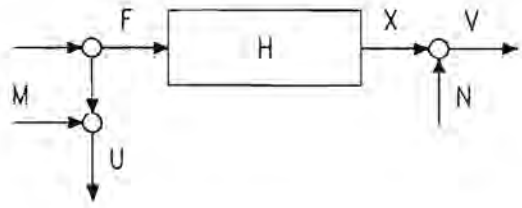

Fig.3.12. General single input/output measurement situation.

When computing the ratio directly, the expression for the measured frequency response is:

$$H'(i\omega) = \frac{V(i\omega)}{U(i\omega)} = \frac{X(i\omega) + N(i\omega)}{F(i\omega) + M(i\omega)} \qquad (3.6)$$

In this form, the measured frequency response will be a good approximation of the true frequency response of the structure only if the measurement noise at both the input and output measurement point is small relative to the input and the output signal.
When using the cross and autopower spectrum, the expression for the measured frequency response becomes:

$$H'(i\omega) = \frac{V(i\omega)U^*(i\omega)}{U(i\omega)U^*(i\omega)} = \frac{G_{XF}(i\omega) + G_{XM}(i\omega) + G_{NF}(i\omega) + G_{NM}(i\omega)}{G_{FF}(i\omega) + G_{FM}(i\omega) + G_{MF}(i\omega) + G_{MM}(i\omega)} \qquad (3.7)$$

where G_{IJ} = crosspower spectrum between the signals I and J

If the noise signals M and N are noncoherent with each other and with the input signal F(t), then the cross spectrum terms involving M and N in Eq.3.7 will average to zero, yielding:

$$H'(i\omega) = \frac{G_{XF}(i\omega)}{G_{FF}(i\omega) + G_{MM}(i\omega)} = \frac{H(i\omega)}{1 + \dfrac{G_{MM}(i\omega)}{G_{FF}(i\omega)}} \qquad (3.8)$$

where $H(i\omega)$ is the desired true frequency response function.

Now, for a good approximation of the frequency response function $H(i\omega)$, the only condition to be fulfilled is that the noise-to-signal ratio at the input measurement point ($G_{MM}(i\omega)/G_{FF}(i\omega)$) should be small.

The cross-spectrum can also be used for computing the coherence function (γ^2_{UV}), which is defined by:

$$\gamma^2_{UV} = \frac{G_{UV}(i\omega)G^*_{UV}(i\omega)}{G_{UU}(i\omega)G_{VV}(i\omega)} \qquad (3.9)$$

The coherence function is a measure of the power in the output signal caused by the input. It will equal 1, if there is no measurement noise and, equal zero when the signals are totally uncorrelated. Low values of the coherence function will also be observed when the structure is non-linear.
The coherence functions depicted in Fig.3.13 show a good coherence of the signals at most frequencies. Low coherence is to be seen at (1) low frequencies of less than 1 Hz, due to the low frequency cut-off of the amplifiers and the frequency resolution of the analyzer, (2) 50 Hz due to electrical noise and (3) high frequencies (> 1200 Hz), due to a decrease in signal level of the input (Fig.3.9) and thus a decrease in signal-to-noise ratio.

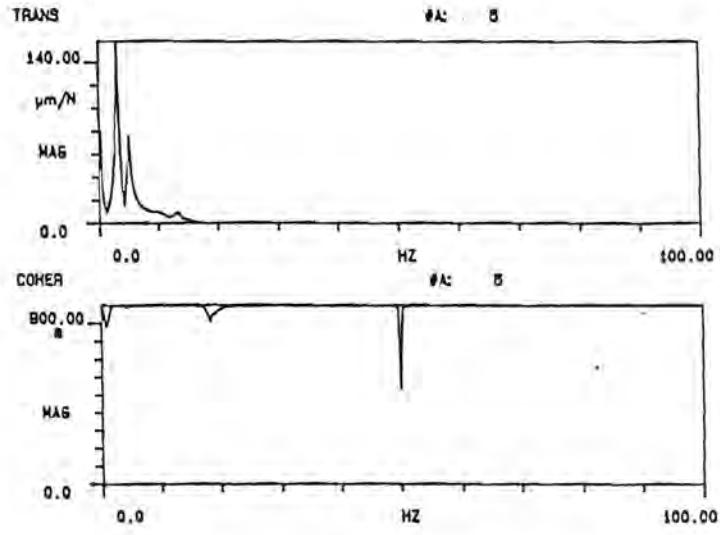

A

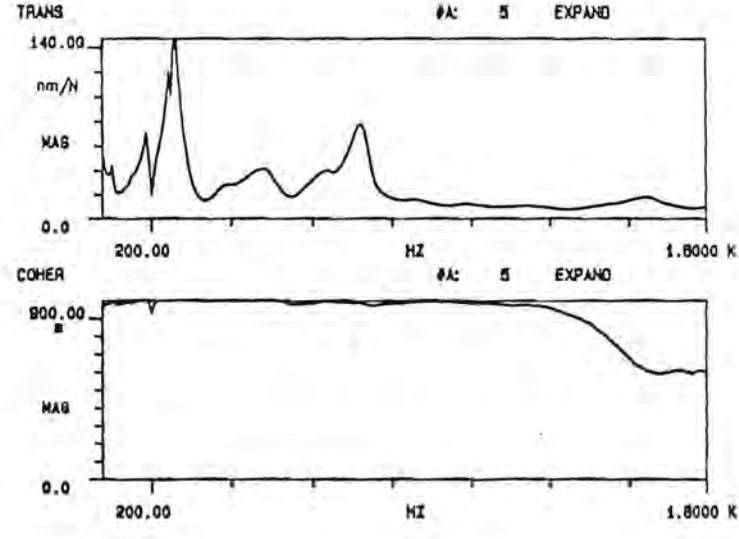

B

Fig.3.13. *Transfer functions and corresponding coherence functions when using a soft tip (A) and a hard tip (B)*

3.3.5 The resonance frequencies and the damping ratios

The resonance frequencies and the corresponding damping ratios are determined from the frequency responses. Modal analysis assumes that the structure is linear. With this assumption, the frequency and damping for a mode are constant over the entire structure. Then, these can be identified from any single measurement in the data set. Of course, those measurements, where the modes are well-defined, are chosen. For example, the frequency response depicted in Fig.3.13a can be used for the identication of the first resonance frequency of 3.1 Hz.

Because of its speed and ease of use, the analyzer uses a single mode curve fitting method for identifying the modal parameters. This method treats the data in the vicinity of a modal resonance peak as if they are solely due to a single mode of vibration.

The mathematical model of the transfer function for this is:

$$H^1_{ij}(i\omega) = \frac{R_{k,ij}}{i\omega - p_k} + \frac{R_{k,ij}}{i\omega - p_k} = \frac{2U_{k,ij}(i\omega-\delta_k) - 2V_{k,ij}\upsilon_k}{\delta_k^2 - 2i\omega\delta_k - \omega^2 + \upsilon_k^2} \qquad (3.10)$$

where $U_{k,ij}$ = real part of the residue
$V_{k,ij}$ = imaginary part of the residue
δ_k = damping coefficient
υ_k = damped natural frequency

In case of a large amount of mode coupling, the estimates will be erroneous, due to a considerable overlapping of data from other modes. In order to take account of this, residual terms are added to Eq.(3.10):

$$H_{ij}(i\omega) = H^1_{ij}(i\omega) + A_1\omega + A_0 \qquad (3.11)$$

A least square error fitting is performed on the data according to:

$$E = \sum_{n}^{m} |h_p - H_{ij}(i\omega_p)|^2 = \text{minimum} \qquad (3.12)$$

where nm = interval to be fit

h_p = p^{th} data value

$H(i\omega_p)$ = fit function at the p^{th} frequency

The identified frequencies and corresponding damping ratios are listed in Table 3.3. It can be seen that the natural frequencies are well-distributed over the frequency range of interest.

Table 3.3. The identified resonance frequencies and corresponding damping ratios.

Mode no.	Frequency [Hz]	Damping [%]	Mode no.	Frequency [Hz]	Damping [%]
1	3.1	6.5	8	240.5	3.9
2	4.9	7.0	9	259.7	3.6
3	9.8	2.1	10	375.6	1.8
4	13.3	2.0	11	631.2	6.2
5	21.9	4.5	12	733.4	3.1
6	87.5	6.2	13	846.9	5.9
7	202.6	2.9	14	992.4	8.7

The low values for the frequencies indicate that the lathe contains some weak elements, which can be located by means of the mode shapes. These shapes will be discussed in next section.

3.3.6 The mode shapes

The mode shapes are determined from the residues. These can be estimated by the same curve fitting process as for the natural frequencies and damping ratios.

The residues and the mode shapes for the k^{th} mode are related by the expression:

$$R_{k,ij} = \frac{\Psi_{ik}\Psi_{jk}}{a_k} = \text{residue} \qquad (3.2)$$

where a_k = scaling constant

Ψ_{ik} = i^{th} component of the mode vector for mode k

The residues for n_d modes ($k = 1..n_d$) can be determined from a single frequency response H_{ij}. According to Eq.(3.2) one row ($i = 1..n_d$) or one column ($j = 1..n_d$) of the matrix of frequency responses, H, is sufficient for identifying the mode shapes. Eq.(3.2) also indicates that one row or one column of residues can be used directly as a mode shape, since the difference between the vector of residues, r_k, and the mode vector, Ψ_k, is only a scale constant Ψ_{ik}/a_k or Ψ_{jk}/a_k.

The estimated mode shapes are depicted in the Figs.3.14 to 3.27. Figs.3.14 to Fig.3.27 show that the low natural frequencies (< 25 Hz) are due to the low stiffness of the rubber isolators, on which the lathe is placed.

The motions of the lathe for these frequencies can be regarded as rigid body motions. However, Fig.3.15 shows large relative motions of some components.

These are mainly due to errors in the measurements, since some points of the complex structure are difficult to hit properly. However, great differences in inertia will also give rise to considerable relative motions.

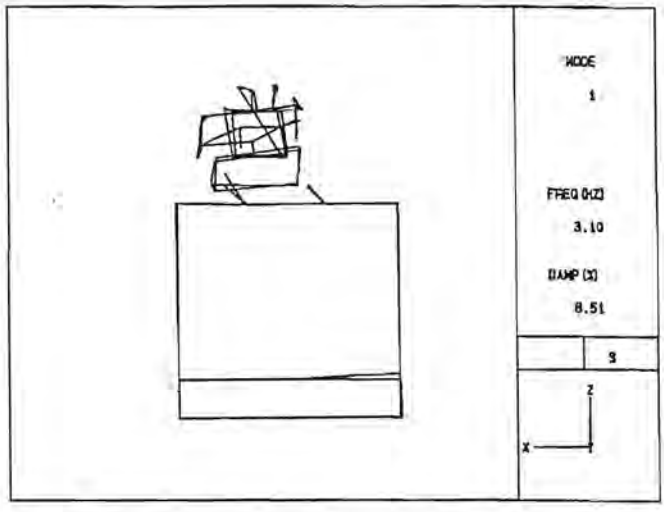

Fig.3.14. Rigid body mode (displacement in x-direction) of the lathe.

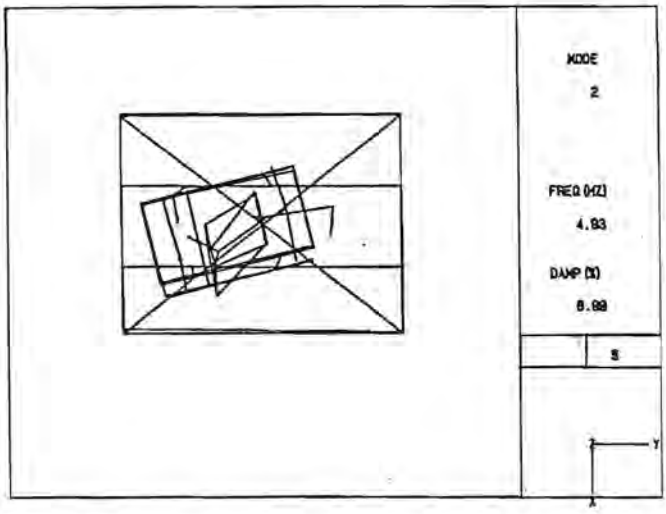

Fig.3.15. Rigid body mode (rotation about an axis in z-direction) of the lathe.

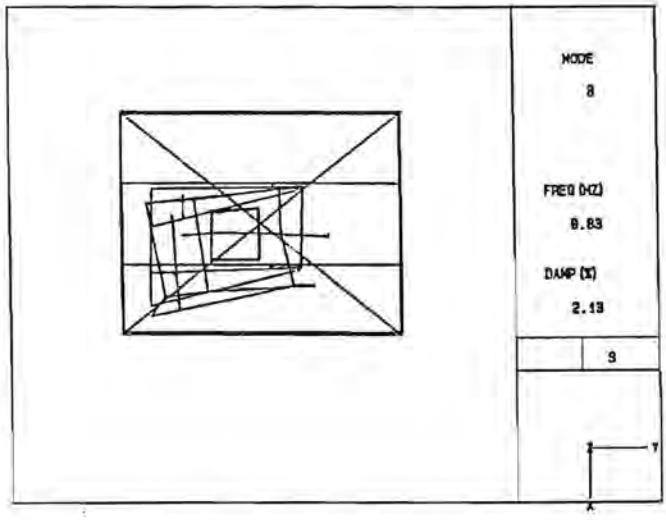

Fig.3.16. Rigid body mode (rotation about an axis in the z-direction) of the lathe.

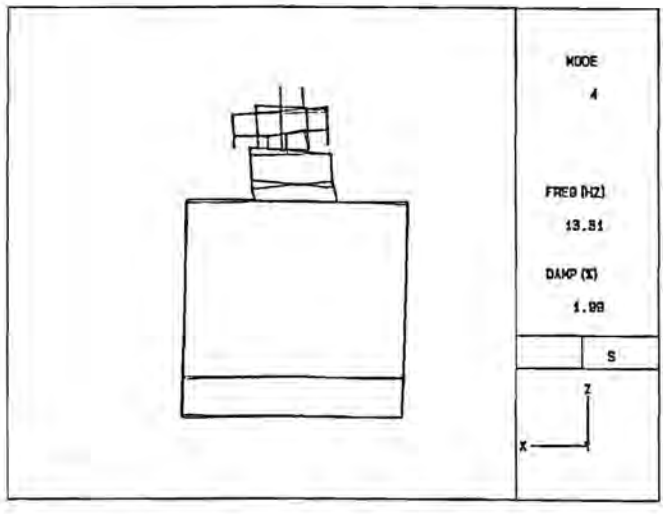

Fig.3.17. Rigid body mode (rotation about an axis in the y-direction) of the lathe.

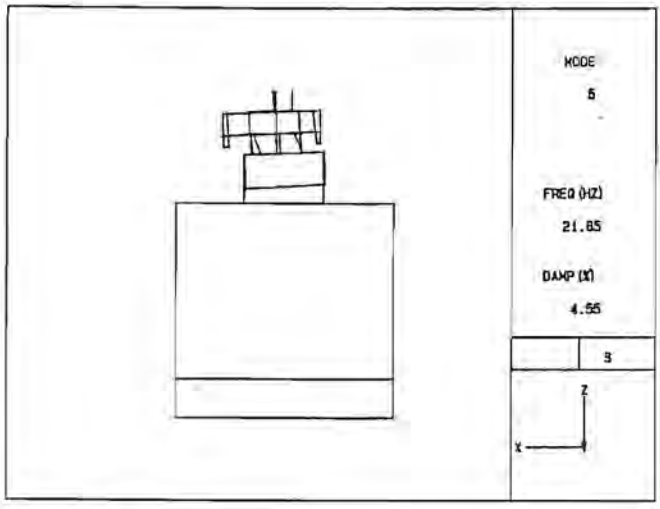

Fig.3.18. Rigid body mode (rotation about an axis in the y-direction) of the lathe.

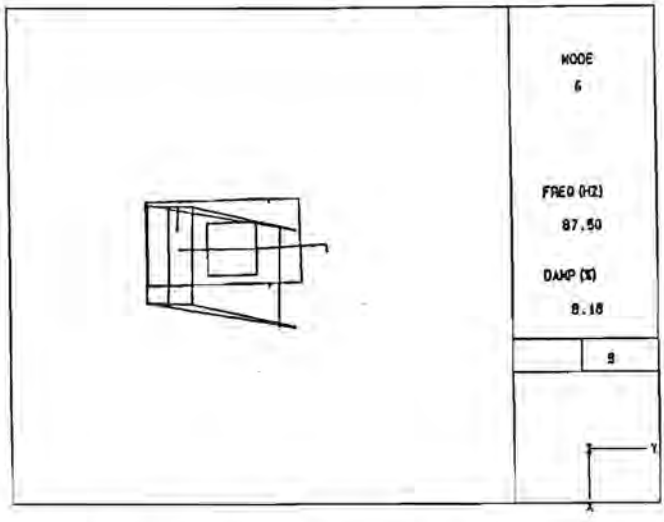

Fig.3.19. Bending mode of the beams of the carriage.

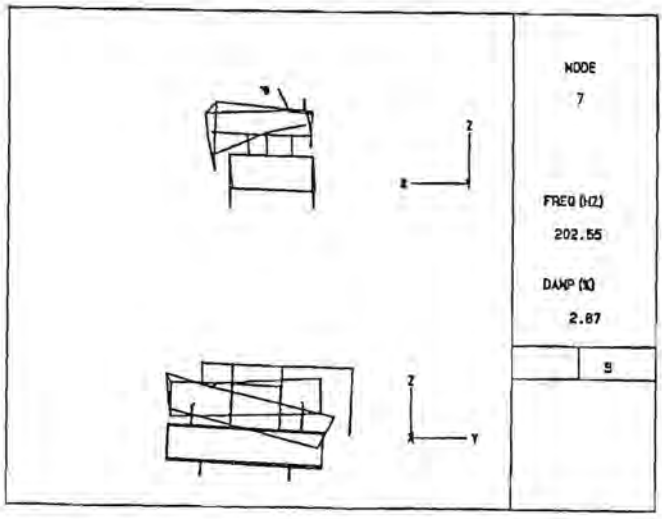

Fig.3.20. Rotation of the passive unit about an axis in the y-direction.

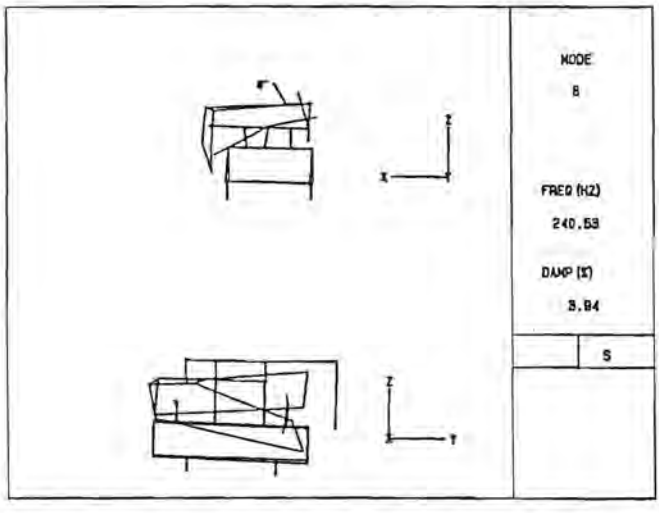

Fig.3.21. Rotation of the passive unit about an axis in the y-direction.

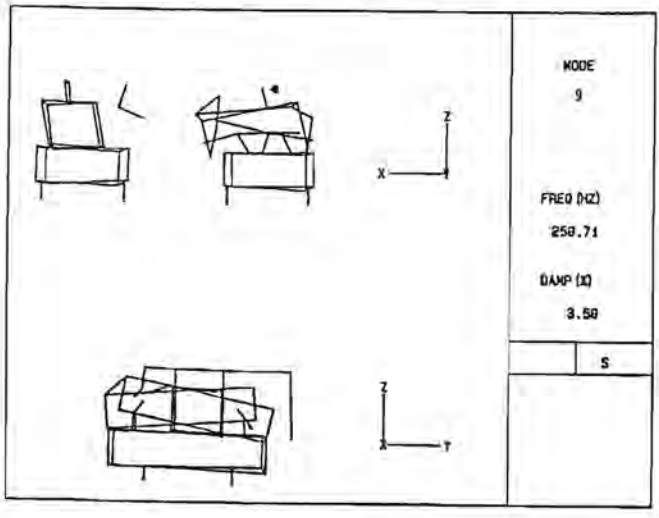

Fig.3.22. Rotation of the passive unit about an axis in the y-direction and displacements of the active unit and the spindle in the x-direction.

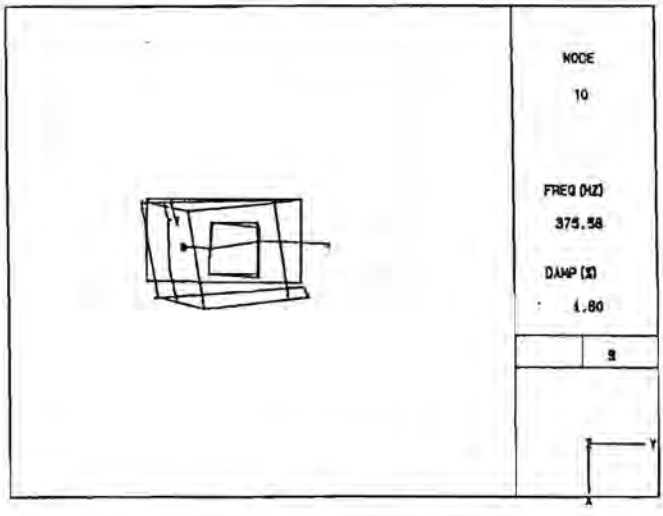

Fig.3.23. Rotation of the carriage about an axis in the z-direction.

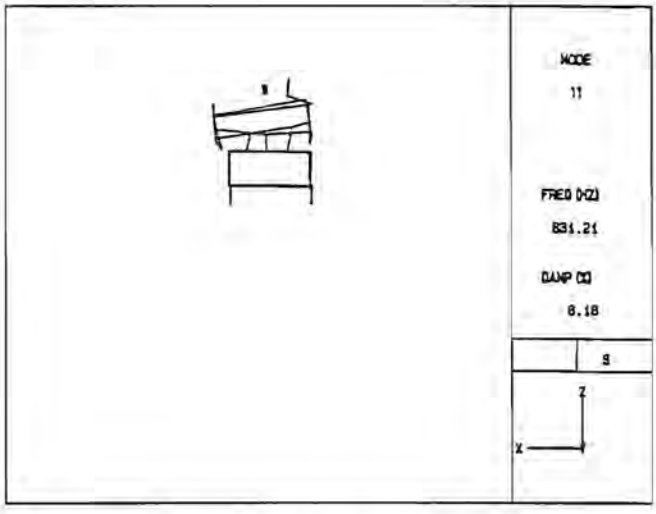

Fig.3.24. Rotation of the active unit about an axis in the y-direction.

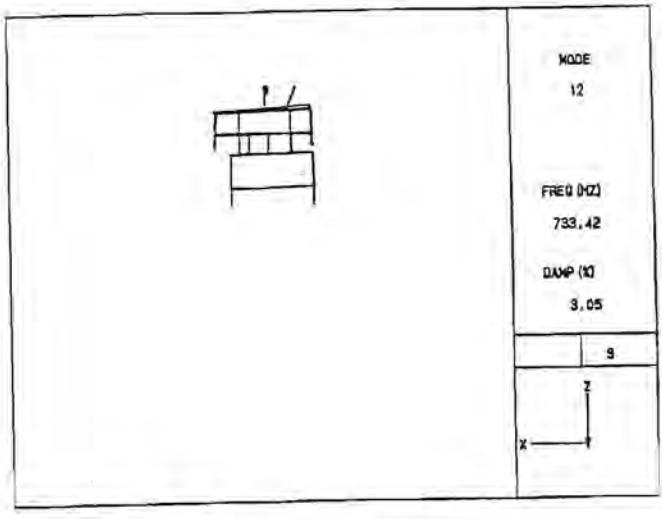

Fig.3.25. Bending mode of the dynamometer.

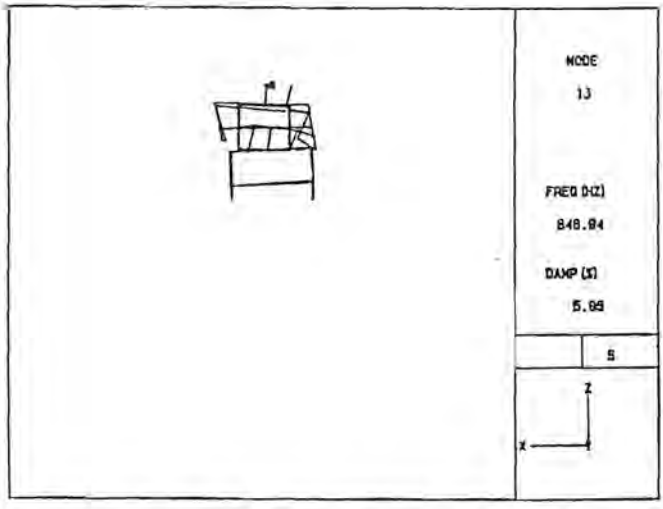

Fig.3.26. *Torsional mode of the beams of the carriage.*

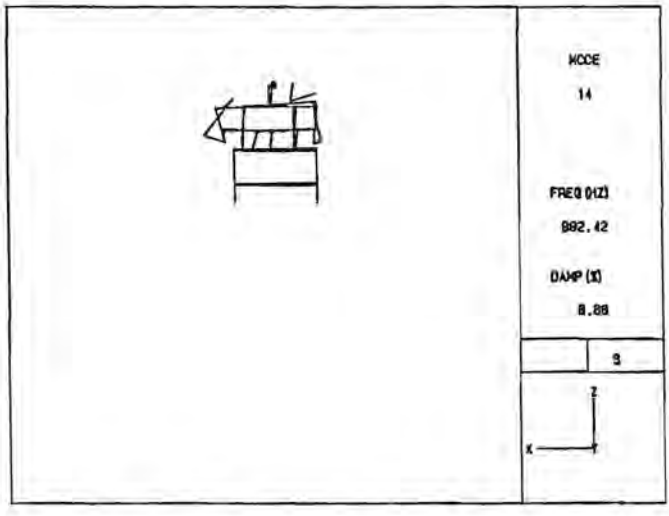

Fig.3.27. *Torsional mode of the beams of the carriage.*

The components in x-direction of the modal vectors for the tool and the workpiece are listed in Table 3.4. From this, it can be seen that the differences are relatively large. If the structure is excited at one of the natural frequencies, then the absolute displacements of the tool or the work-piece will be large and, since the relative displacements are more or less proportional to these absolute displacements, these may be considerable.

Table 3.4. The components in x-direction of the modal vectors for resonance frequencies less than 50 Hz.

Mode no.	Frequency	Component of modal vector	
		Tool	Work-piece
	Hz	10^{-3}	10^{-3}
1	3.1	22.4	26.3
2	4.9	4.4	3.6
3	9.8	2.0	0.8
4	13.3	0.7	0.9
5	21.9	2.1	2.1

For example, if the spindle is driven at a number of rotations of 3.1 (corresponding to the natural frequency of mode 1), then the amplitude of the vibrations of the tool is about 300μm (Fig.3.28) and the amplitude of the relative motion will be $300 \times \frac{26.3-22.4}{22.4} = 52$ μm. This approximation of the relative motions by means of mode shapes is unreliable, since the errors in the mode shapes may be more than 5%. This can result in errors in the relative motions of nearly 100%. Nevertheless, it indicates that the relative displacements may be very large when exciting at one of the natural frequencies. Therefore, exciting forces with frequencies equal to one of the natural frequencies should be avoided by chosing the appropiate operational conditions.

A detailed discussion about the displacements of the tool with respect to the work-piece will be given in the next section.

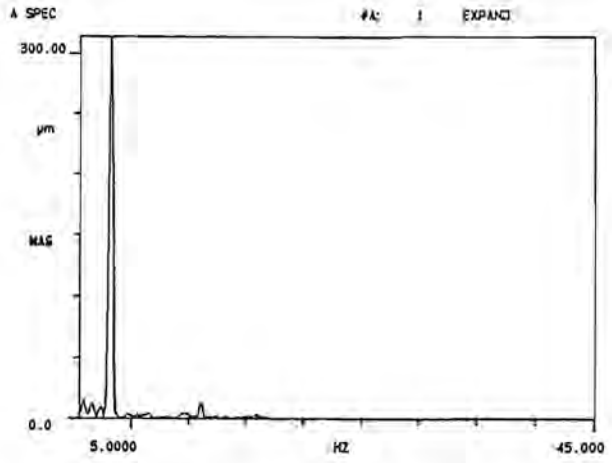

Fig.3.28. Autopower spectrum of the displacement of the tool when the spindle is driven at a number of rotations of 3.1.

The Figs.3.19 - 3.27 show that resonances at higher frequencies (> 50 Hz) are mainly due to weak elements in the carriage. The shaft of the passive unit is not fixed in the x-direction and the stiffness of the beams, which connect the active and the passive unit, is low. Therefore, a bending mode of the beams in the x-direction at a relative low frequency of 87.5 Hz is observed. The passive unit is connected to the base by a single joint, which does not resist rotations about an axis in the y-direction (modes at 202.6, 240.5 and 259.7 Hz). These rotations of the passive unit will lead to torsional modes of the plate, on which the toolholder is fixed, and these torsions may result in large displacements of the tool. Even if the rotations are small, the displacements of the tool may be considerable, since the distance between the tool and the plate is relatively large (about 70 mm).

An indication of the large displacements is the magnitude of the component of the mode vector for the tool (Table 3.5). This magnitude is very large with respect to that of the work-piece.

Table 3.5. The components in x-direction of the modal vectors for resonance frequencies higher than 200 Hz.

Mode no.	Frequency	Component of modal vector	
		Tool	Work-piece
	Hz	10^{-6}	10^{-6}
1	202.6	59.4	-8.0
2	240.5	51.6	6.8
3	259.7	59.7	-37.9

At the frequency of 259.7 Hz (Fig.3.22), there are also vibrations of the active element and the spindle in x-direction. The vibrations of the spindle are out of phase with respect to those of the active element and with that, the tool. Consequently, large roughness values will be obtained when exciting at the frequency of 259.7 Hz. The low value of 259.7 Hz indicates that the stiffness of the supports of both the spindle and the active element is moderate.
The moderate stiffness of the supports of the active element is also the cause of the rotations of the whole carriage about an axis in the z-direction at 375.6 Hz (Fig.3.23) and of the active element about an axis in the y-direction at 631.2 (Fig.3.24) and 846.9 Hz (Fig.3.26). The mode at 733.4 Hz (Fig.3.25) is a vibration of the tool in the x-direction. Torsion of the beams, which connect the active and the passive element, will be observed when exciting at 846.9 and 992.4 Hz (Fig.3.27).

3.3.7 The weak elements

The modal shapes show several weak elements in the structure, namely:

1. the joints of the active and passive element of the carriage,
2. the beams which connect the elements of the carriage,
3. the supports of the spindle and
4. the toolholder.

These elements should be modified when the displacements of the tool with respect to the work-piece due to potential exciting forces are untolerable.

Estimations of these displacements will be given in the next section.

3.4 The displacements of the tool with respect to the work-piece

The displacements of the tool with respect to the workpiece, in the following text referred to as relative displacements, can be calculated in the frequency domain by multiplying the exciting force by the difference of the frequency response at the tool and that at the work-piece. This difference can be determined (1) by measuring the frequency responses separately with one accelerometer and, then taking the difference of the responses or (2) by measuring it at once by means of two accelerometers.

The first method has several disadvantages:

1. Since the impacting is done by hand, the input signals for the two measurements may not be identical and erroneous estimates of the relative frequency response may be obtained due to non-linear effects.
2. The relative frequency response may be only a few percent of the separate one. As the errors in the separately measured responses may be of the same order of magnitude or even larger, the estimate of the relative frequency response, being the difference of two separately measured responses, will be very unreliable.

Since the relative displacements are very small, the method with two accelerometers will only be suitable, if their sensitivity is very high. However, the sensitivity of the available accelerometers was only 1.8 pC/ms^{-2}. Consequently, the noise-to-signal was untolerably high.

Therefore, the use of an optical sensor has been considered.

This Compact Disc optical pick-up system was developed at the Philips Research Laboratories in Eindhoven for geometrical measurements, especially for the surface roughness measurements of smooth surfaces.

A schematic diagram of the sensor is shown in Fig.3.29.

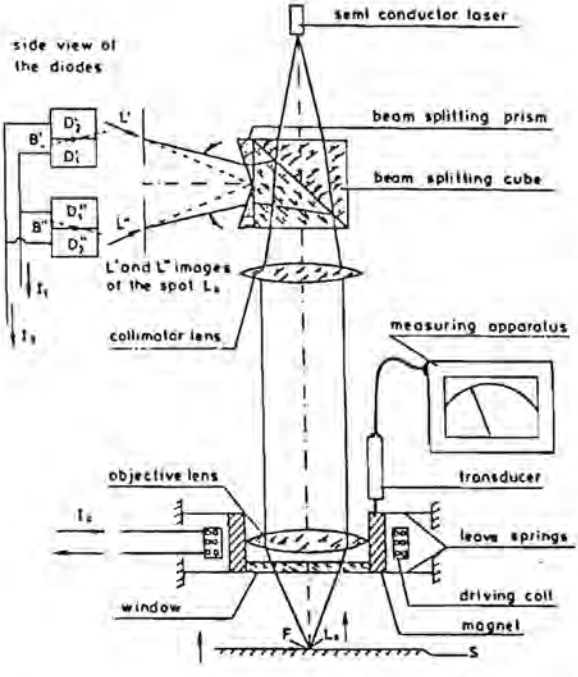

Fig.3.29. Schematic diagram of the optical sensor.

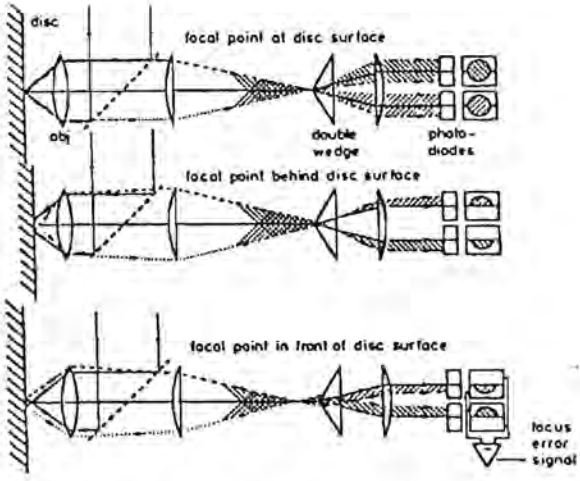

Fig.3.30. Focus error detection system using the foucalt double wedge system.

A displacement of the surface in the z-direction results in a focus error, which is detected by means of a Foucault-double wedge system (Fig.3.30) [3.5]. The sensor can be used in two modes, namely:

1. The dynamic mode.
   The position of the objective lens is controlled by means of the focus error signal and the lens is displaced until the focal point is at the surface. The displacement is measurement by an inductive sensor which is coupled to the lens. The range of displacement in this mode is 500 μm and the frequency range is about 600 Hz.
2. The static mode.
   The objective lens is fixed and the displacement of the surface is determined directly from the focus error signal. The range of displacement is 2 μm and the frequency range is 1.5 kHz.

The signal from the optical sensor is amplified by a Hottinger Baldwin measuring bridge, type KWS/3S-5, with a bandwidth of 1 kHz.

Fig.3.31a shows that the total noise level of this optical measuring system is considerable (about 15 nm). However, for almost every frequency, the separate component is less than 1nm, which is acceptable (Fig.3.31b).

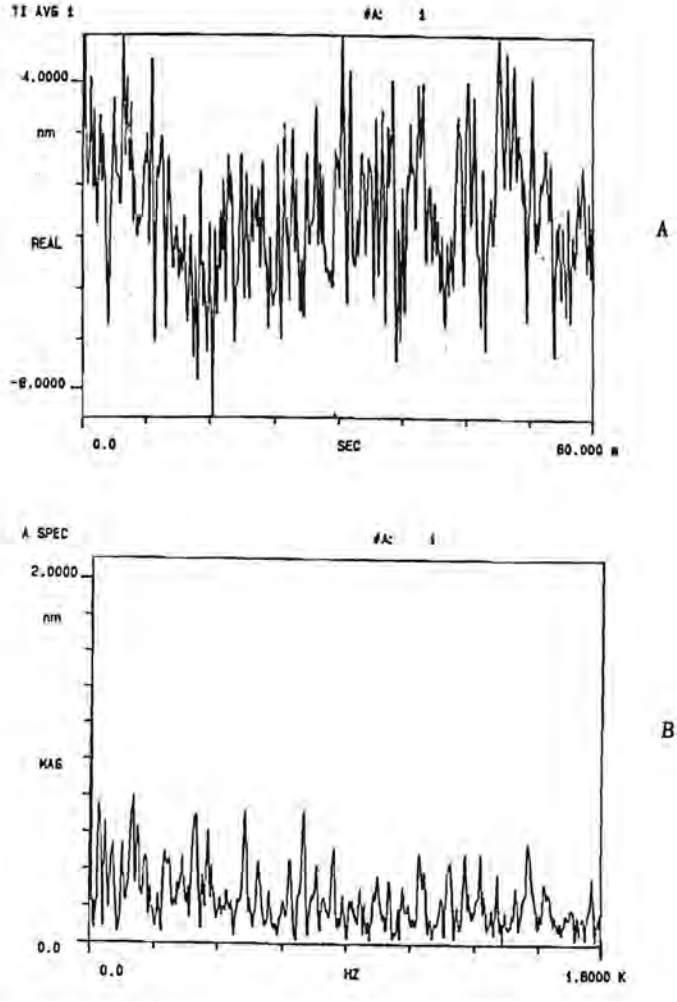

A

B

Fig.3.31. The noise signal of the optical pick-up system in the time (A) and the frequency (B) domain.

The important exciting forces are the cutting forces and those acting at the foundation and the driving system. An estimation of the relative displacements due to these forces will be made in the following sections.

3.4.1 The displacements due to forces at the foundation

Fig.3.32 shows that the lathe is well-isolated from vibrations of the foundation. The compliance of about 5 nm/N at the resonance frequencies of 9.8 and 13.3 Hz may not be neglected. However, the force components will be small (< 0.5 N), even when stamping the feet in the neighbourhood of the lathe, and the relative displacements will be less than 10 nm.

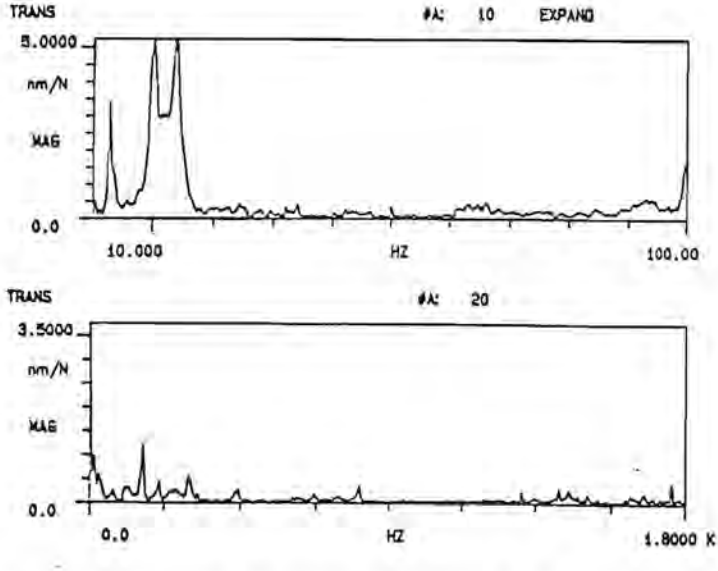

Fig.3.32. The transfer function of forces at the foundations to displacements of the tool relative to the work-piece in x-direction.

3.4.2 The displacements due to forces at the driving system

The relative frequency response to a force on the pulley of the spindle is shown in Fig.3.33. The force variations in the y-direction are much smaller than those in the x-direction and the z-direction. Therefore, the y-direction will not be considered.
The compliances at the natural frequencies are considerable (> 100 nm/N when exciting at x-direction and > 50 nm/N when exciting in the z-direction).
The force variations are caused by vibrations of the motor, variation of belt thickness and slip of the belts. The driving force for rotating the shaft of the spindle depends upon the rotational speed and ranges from 10 to 50 N.
Slipping of the belts may cause force variations in the order of magnitude of 1 N. Hence, the relative displacements of the tool can be more than 0.1 μm.
Force variations due to vibrations of the motor and variation of the belt thickness are one order of magnitude smaller, but the relative displacements may still be untolerable when exciting at a natural frequency.

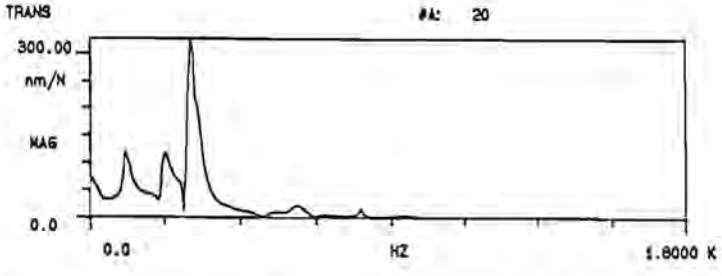

Fig.3.33a. The transfer function of forces on the pulley in x-direction to displacements of the tool relative to the work-piece in x-direction.

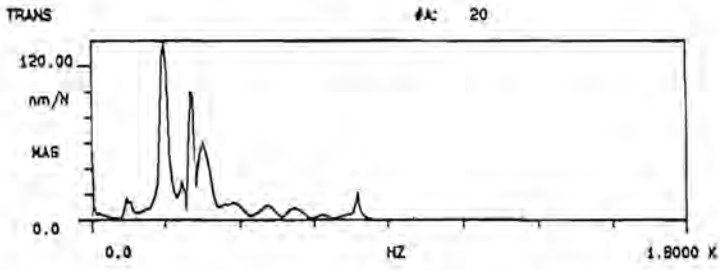

Fig.3.33b. The transfer function of forces on the pulley in z-direction to displacements of the tool relative to the work-piece in x-direction.

3.4.3 The displacements due to the cutting forces

Cutting forces are acting on the work-piece as well as on the tool, but in opposite direction. Therefore, the frequency response is now taken to be the difference of the frequency responses to excitations in the same direction at the tool and at the work-piece.
The resulting response is depicted in Fig.3.34, which shows that the compliance is about 120 nm/N for frequencies less than 100 Hz and about 300 nm/N at the natural frequencies of 202.6, 240.5 and 259.7 Hz.

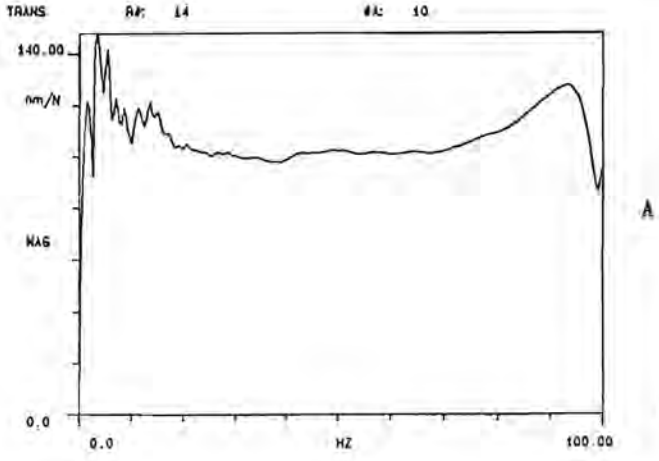

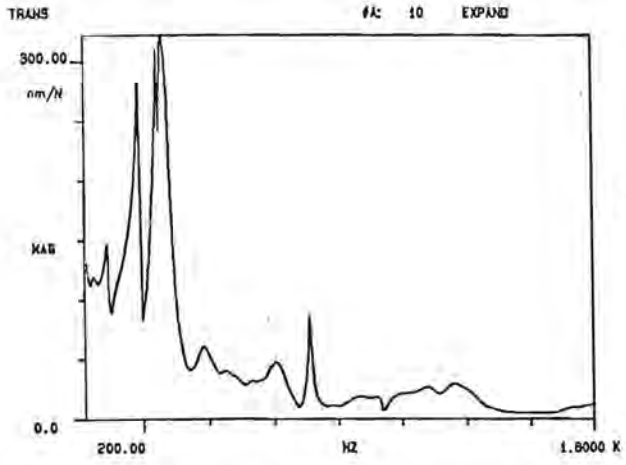

B

Fig.3.34. *The transfer function of cutting forces to displacements of the tool relative to the work-piece in the x-direction.*

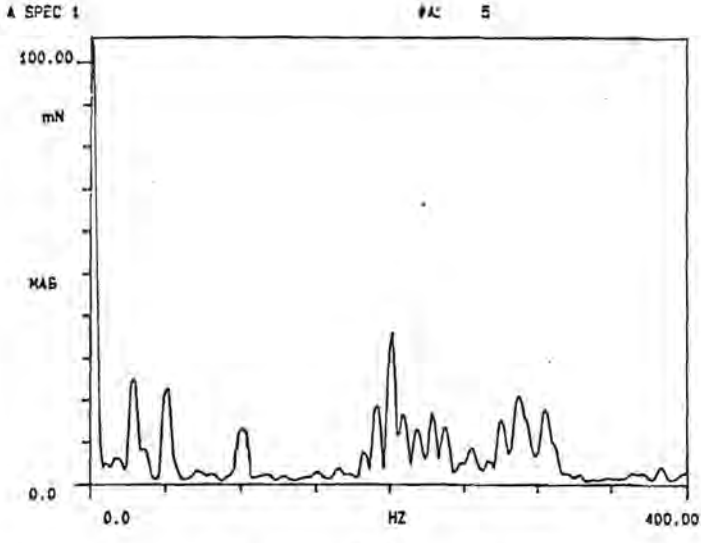

Fig.3.35. *Autopower spectrum of the cutting forces.*

The amplitude of force variations can be more than 20 mN (Fig.3.35) and, if the frequency is one of the mentioned natural frequencies around 200 Hz, the relative displacements will be more than $2*20*300*10^{-3}$ = 12 nm.
At frequencies less than 100Hz, the magnitude is about 5 nm.
Fig.3.35 shows that there may be more than one significant component. Consequently, the relative displacements may become untolerable (> 50 nm).

From these considerations, it may be concluded that the relative displacements can be untolerable under the existing conditions. Therefore, it is desirable to modify the weak elements of the lathe. This can be done efficiently by means of a numerical model, which will be discussed in the next section.

3.5 The numerical model

The analytical procedure involves the determination of the mass, stiffness and damping matrices from the geometry and the material properties of the components. This is not easy for a complex structure such as the precision lathe. Therefore, the structure of the lathe is mathematically simulated by a simple network of a few beam, mass, spring and damping elements.
After the simplification of the structure, the coordinates to be considered are numbered. Then, the system matrices are assembled from the element matrices by transforming these from the local to the global axes and adding together the coefficients corresponding to the same nodal coordinates (the direct method [3.6]).
The mass and stiffness matrix of a beam element can be easily determined by means of well-known relationships [3.6]. On the contrary, it is difficult to determine or even to estimate absolute structural damping. Therefore, the following solution has been chosen.

Since the amount of damping normally present in structural systems is relatively small, its effect is neglected in the calculation of the natural frequencies and the mode shapes. Hence, the structure is in first instance regarded as being undamped and the eigenproblem is solved. In order to estimate the transfer function, the structure is assumed to be proportionally damped and the transfer function is determined according to the following equation (See appendix A.1):

$$H_{ij}(i\omega) = \sum_{k=1}^{n} \frac{\Psi_{ik}\Psi_{jk}}{-\omega^2 m_k + i\omega c_k + k_k} = \sum_{k=1}^{n} \frac{\Psi_{ik}\Psi_{jk}}{m_k(-\omega^2 + 2i\omega_k\zeta_k + \omega_k^2)} \qquad (3.13)$$

The stiffness of spring elements can be determined from the properties of the components, but most of the components have a complex geometry and usually, it is difficult to determine the stiffness of such a geometry accurately by means of a simple or even advanced method. Since the modal analysis has been performed experimentally, it is in the first instance better to estimate the stiffness values from the experimental results by means of an iteration method.

The procedure for this is described by the following steps:

1. Assumption of feasible values for the stiffnesses.
   These values can be calculated by means of simple methods.
2. Calculation of the eigenvalues, the modal shapes and several frequency responses.
   The procedure for solving the eigenproblem is described in appendix A.2.
   The values of the damping ratios, which are needed for the calculation of the frequency responses, are based on the experimental results.
3. Comparison of the calculated and the measured values.
4. Repetition of the modification of the stiffness values and step 2 and 3 until good agreement between the measured and the calculated values is obtained.
5. Modification of the model if the agreement is still bad after applying all of the possible combinations of stiffness values.
6. Repetition of step 1 to 5 until the agreement is good.

The starting model of the structure may be too simple and can fail to describe the real structure accurately. Therefore, step 5 and 6 are included in the procedure.
The iteration method has been performed on the carriage and the spindle. The results will be mentioned in the next section.

3.5.1 The models for the carriage and the spindle

The program for determining the modal parameters is written in Turbo Pascal and the available memory size for data is limited to 64K. Therefore, the oil reservoir, which is the base of both the carriage and the spindle, is assumed to be very stiff and these components are considered separately. However, this assumption may not be true and may lead to the absence of effects of mutual influencing in the separate considerations. Therefore, it should be kept in mind, that a poor agreement between the measured and the calculated results can be imputed to this assumption instead of a wrong model of the component.

3.5.1.1 The carriage

Fig.3.36 shows the simplified configuration of the carriage, which consists of ten beam elements, one mass element and three spring elements. The elements 1, 2 and 3 correspond to the shaft of the active unit and elements 5 and 6 represent the shaft of the passive unit. The segments 4 and 7 are the bars, which connect the active and the passive unit and the frame for the dynamometer is idealized by the segments 8, 9 and 10. The bearings and the supports of the active unit are modelled by the spring elements 11 and 12, and the support of the passive unit by spring element 13. A mass element at point 8 represents the mass of the dynamometer.
Each of the nine nodal points have six coordinates.

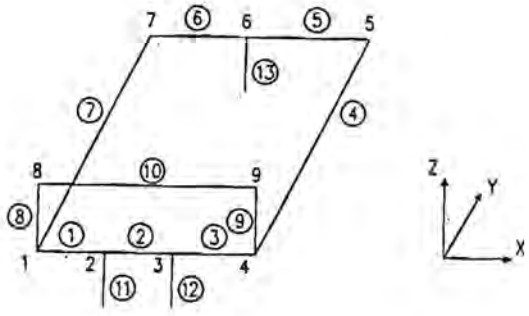

Fig.3.36. *The model of the carriage.*

The final natural frequencies and corresponding mode shapes obtained from the iteration method are depicted in Fig.3.37 and several transfer functions are shown in Fig.3.38.

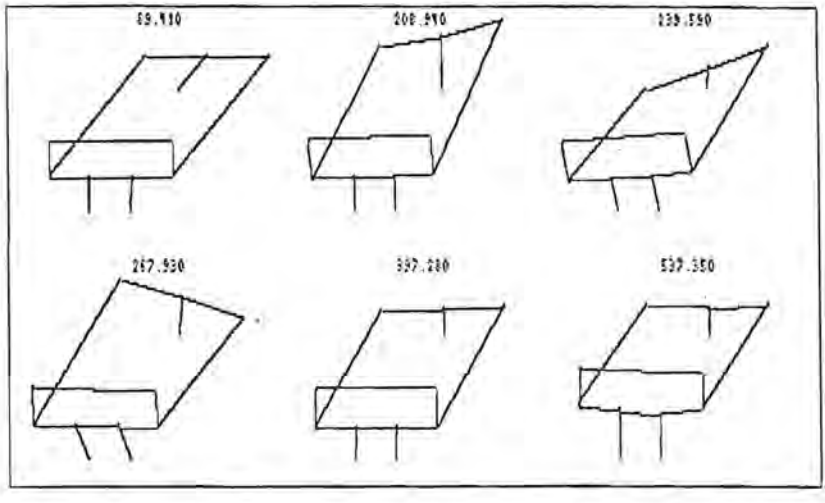

Fig.3.37. *The calculated natural frequencies and the corresponding mode shapes of the carriage.*

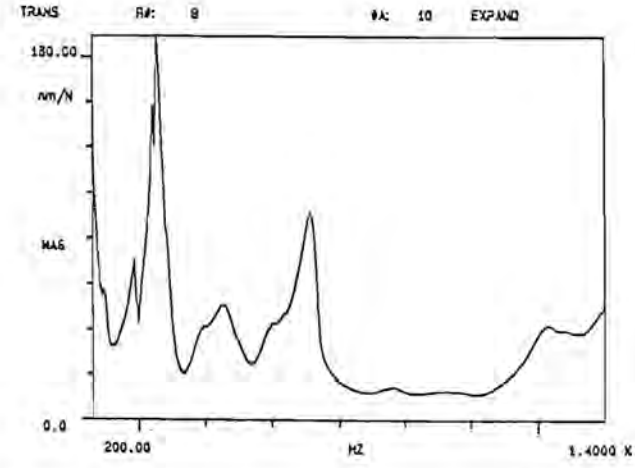

Fig.3.38a. The measured transfer function of forces at point 8 (tool) to displacements at point 8.

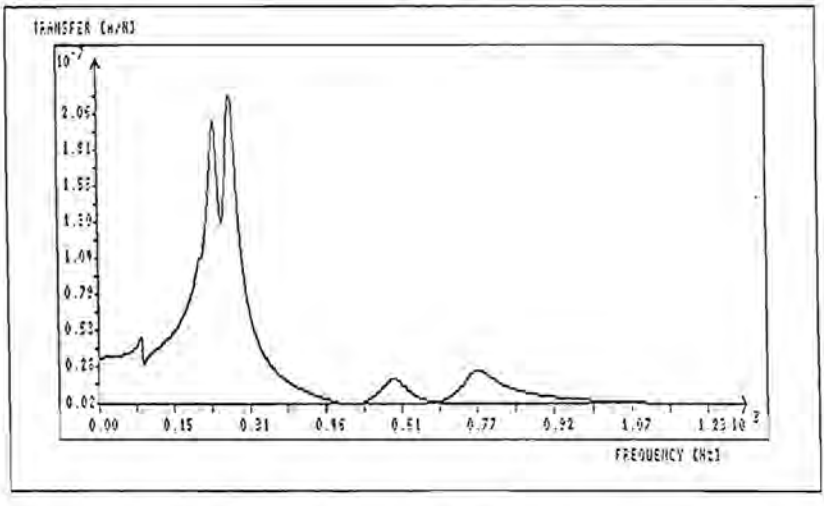

Fig.3.38b. The calculated transfer function of forces at point 8 (tool) to displacements at point 8.

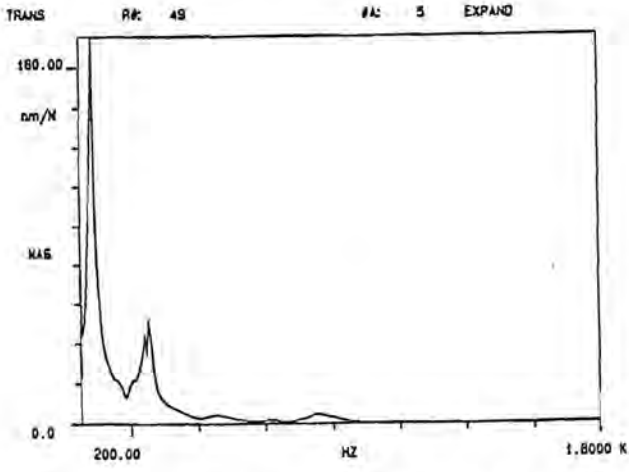

Fig.3.38c. *The measured transfer function of forces at point 5 (shaft of the passive unit) to displacements at point 8 (tool).*

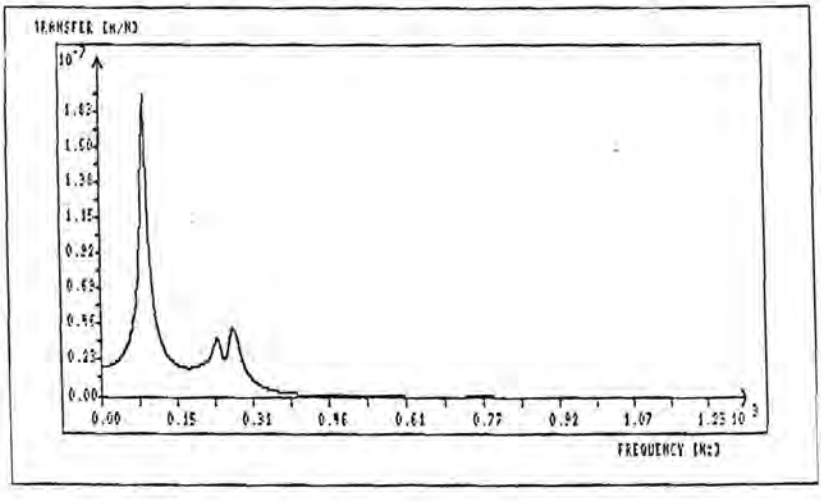

Fig.3.38d. *The calculated transfer function of forces at point 5 (shaft of the passive unit) to displacements of point 8 (tool).*

In order to get a good correspondence between experimental and calculated results, one modification of the model has had to be made. In the starting model, it is assumed that shafts are firmly connected to the bars, but, in fact, the connection is made by means of slender bolts. Since the influence of this weak connection is mainly restricted to rotations of the bar about the axis of the shaft, it is simulated by decreasing the torsional stiffness of the elements 1, 3, 5 and 6.

If this modification is omitted, then the mode shapes at the frequencies of about 200, 240 and 260 Hz will be obtained at higher frequencies (Fig.3.39) and the dynamic compliances will differ considerably from the measured compliances (Fig.3.40).

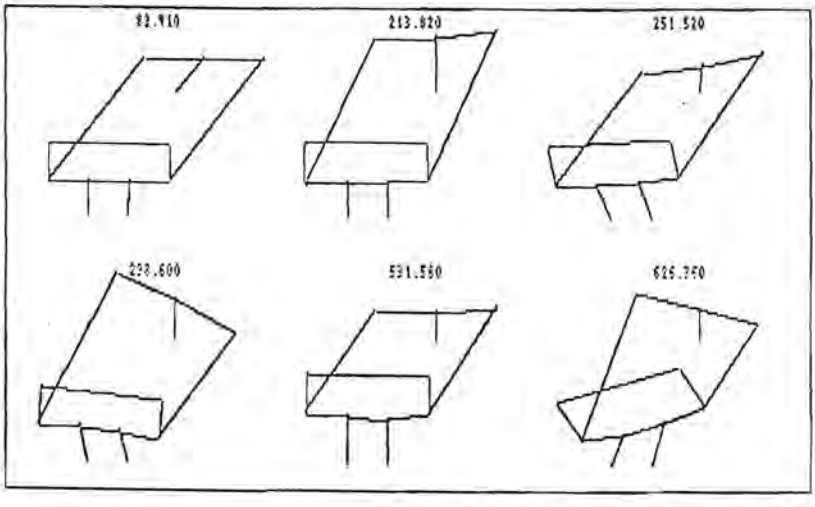

Fig.3.39. The calculated natural frequencies and the corresponding mode shapes of the carriage with rigid couplings of the bar and the shafts.

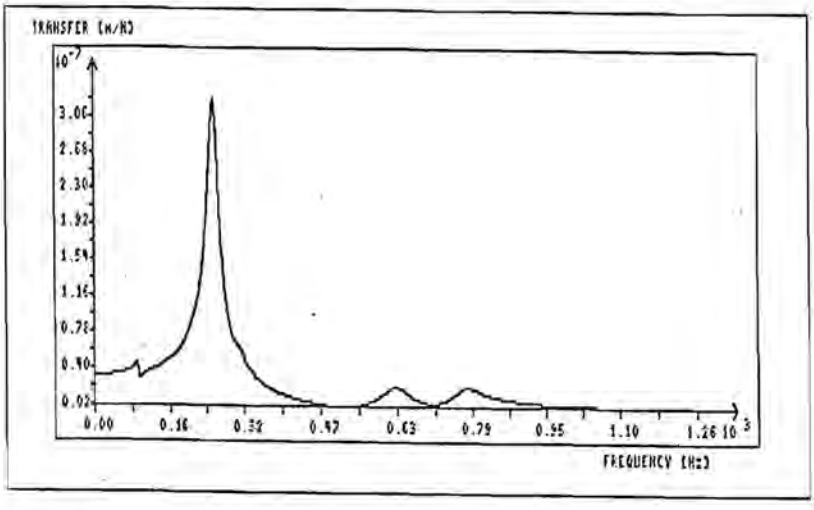

Fig.3.40. The calculated transfer function of forces at point 8 (tool) to displacements at point 8 for a carriage with rigid couplings of the bars and the shafts.

The dynamic compliances at the natural frequencies of about 89, 209, 240 and 268 Hz are rather high and and may give rise to untolerable displacements (See section 3.4). Therefore, modifications of the construction should be looked for, in order to minimize the compliances at the natural frequencies.
The low value of 89 Hz for the first natural frequency is due to the relatively large length and the small moment of inertia of the bars, which connect the active and the passive unit. Hence, the value can be increased by applying shorter and/or thicker bars. The shortening of the bar is limited by the presence of the base for the spindle and is not desirable, since it may yield larger position errors of the tool due to geometric errors of the passive unit. The thickening of the bars increases the natural frequencies, but may not result in a lowering of the dynamic compliance. For example, when the thickness is taken to be double the present value, the compliance can be more than three times the present value (Fig.3.41).

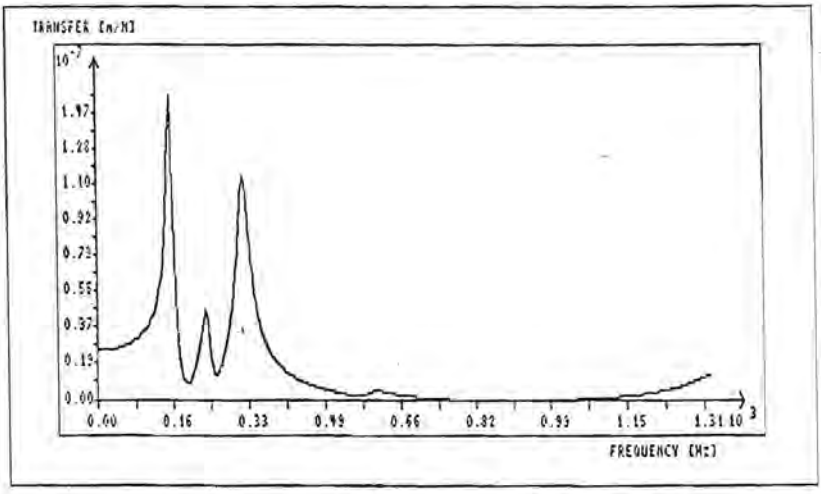

Fig.3.41. The calculated transfer function of forces at point 8 (tool) to displacements at point 8 for a carriage with thicker bars (0.04 m).

This is due to an extra motion of the active unit, which is transferred from mode 3 to mode 1 as a result of the alteration of the stiffness and mass of the bars (Fig.3.42).

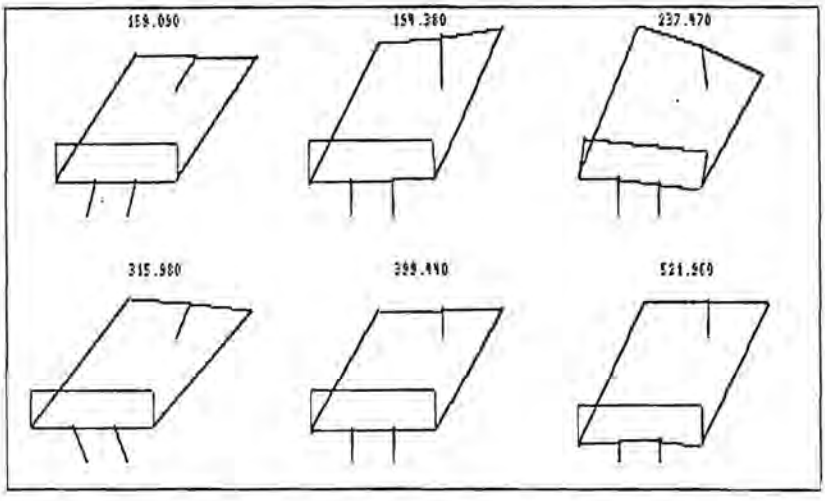

Fig.3.42. The calculated natural frequencies and the corresponding mode shapes of a carriage with thicker bars.

In spite of the large increase of the dynamic compliance, this modification should be kept in mind, because it reduces the compliances at other frequencies.
The mode at about 209 Hz is caused by the low stiffnesses of the support of the passive unit and the connections of the bars and the shafts. A low value of $1.75*10^7$ N/m in the z-direction for the stiffness of the support of the passive unit is obtained from the iteration procedure. This may not be exact but, since the passive unit is not firmly fixed to the base (ball joint), it is not improbable that it will approach the real value.
A stiff support can be used, but then the structure will be statically over-determined and this may lead to undesirable bending and twisting during displacement of the carriage. Besides, it will not result in considerable reductions of the dynamic compliances.

A rigid coupling between the bars and the shafts will reduce the rotation of the bars about the axis of the shaft of the active unit, but will not affect the dynamic compliance at about 209 Hz (Fig.3.40).
The modes at about 240 and 268 Hz are combinations of displacements of the active unit in the x-direction and rotations of the passive unit about an axis in the y-direction. In the model, the stiffness between the shaft and the cylinder and the stiffness of the supports of the active unit in x-direction are combined and represented by one value at point 3. This value is about $5*10^7$ N/m, which is not low, but can be increased by applying stiffer supports and/or by increasing the stiffness between the shaft and the cylinder.
As this stiffness is approximately proportional to the active area of the piston, the increase of the stiffness can be accomplished by enlarging this area and, thus, the dimensions of the shaft.
Increasing the combined stiffness to $7.5*10^7$ N/m will result in reductions of the dynamic compliances, except for mode 4 (Fig.3.43). The rotations of the passive unit can be restricted by using another joint, but then the structure will be over-determined. Hence, other solutions should be looked for in order to minimize the influence of these rotations.
As mentioned earlier, the dynamic compliances at mode 3 and 4 can be strongly reduced by applying thicker bars (Fig.3.41). The influence of the rotations can also be affected by using rigid couplings between the bars and the shaft.
A combination of a higher stiffness of the active unit in x-direction ($7.5*10^7$ N/m), thicker bars (0.04 m instead of 0.02 m) and rigid couplings will give dynamic compliances less than 85 nm/N (Fig.3.44), which is less than 50% of the present values.

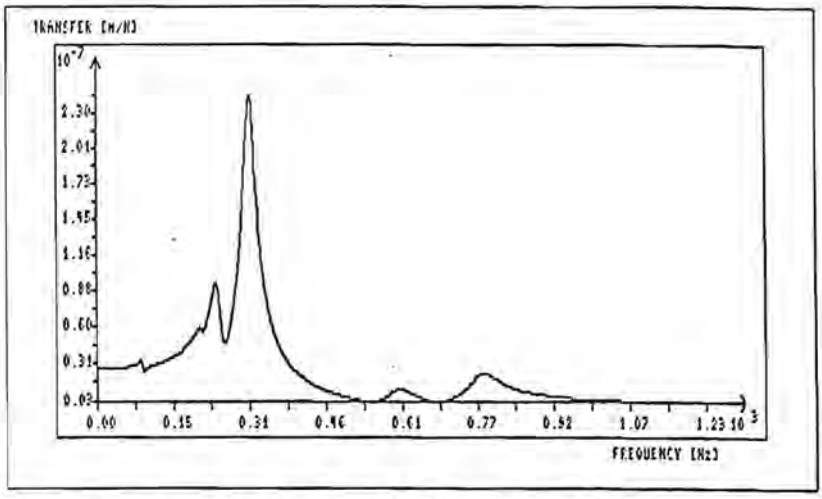

Fig.3.43. The calculated transfer function of forces at point 8 (tool) to displacements at point 8 for a carriage with a stiffness of $7.5*10^7$ N/m between the shaft and the supports of the active unit.

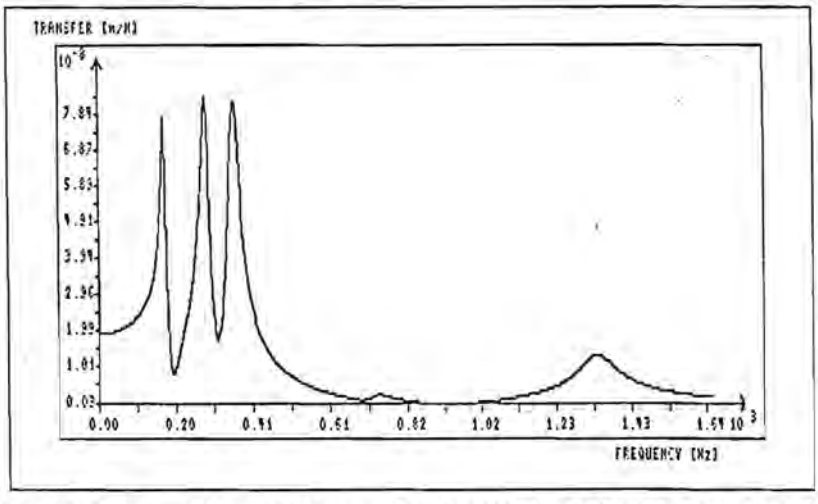

Fig.3.44. The calculated transfer function of forces at point 8 (tool) to displacements at point 8 of a carriage with thicker bars, higher stiffness between the shaft and the supports of the active unit and rigid couplings of the bars and the shafts.

A further reduction can be achieved by increasing the damping. For example, by immersing most parts of the carriage in an oil-bath. If the damping ratios are increased by 1%, then the dynamic responses will be less than 70 nm/N.
Other modifications, such as changing the length of the bars or the shafts, will not lead to remarkable improvements of the behaviour of the carriage.

3.5.1.2 The spindle

The model for the spindle is shown in Fig.3.45 and it consists of 5 beam elements, 4 spring elements and 2 mass elements. Element 1 represents the cylinder and the elements 2, 3, 4 and 5 correspond to the shaft.
The supports are modelled by the spring elements 6 and 7 and the bearings by the spring elements 8 and 9. Mass elements at point 3 and 7 represent the work-piece and the pulley.
Since the attention is restricted to the behaviour in the x-direction, each of the eight nodal points will have only 2 coordinates.

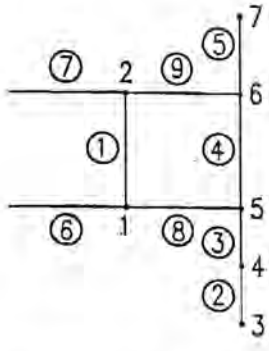

Fig.3.45. The model of the spindle.

The final natural frequencies and corresponding mode shapes obtained from the iteration procedure are shown in Fig.3.46.
A transfer function is depicted in Fig.3.47.

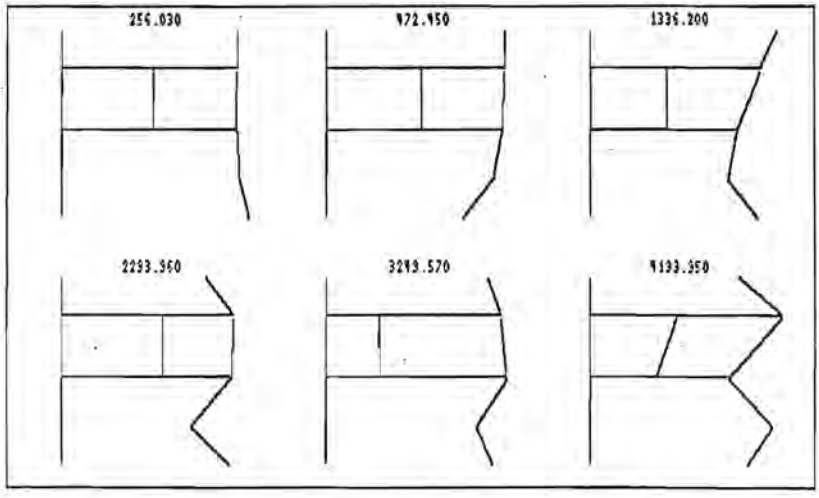

Fig.3.46. The calculated natural frequencies and the corresponding mode shapes of the spindle.

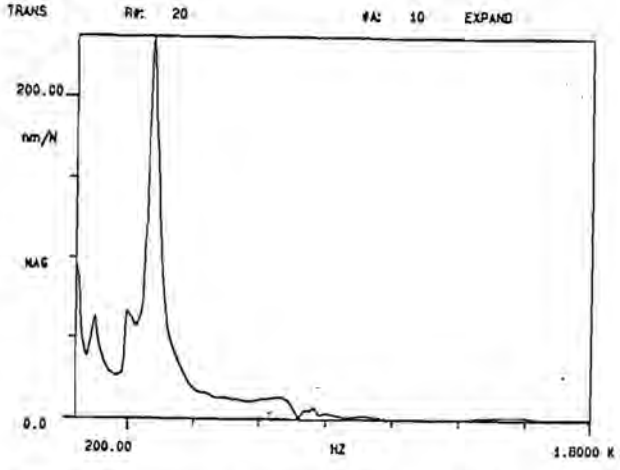

Fig.3.47a. The measured transfer function of forces at point 3 (pulley) to displacements of point 7 (work-piece).

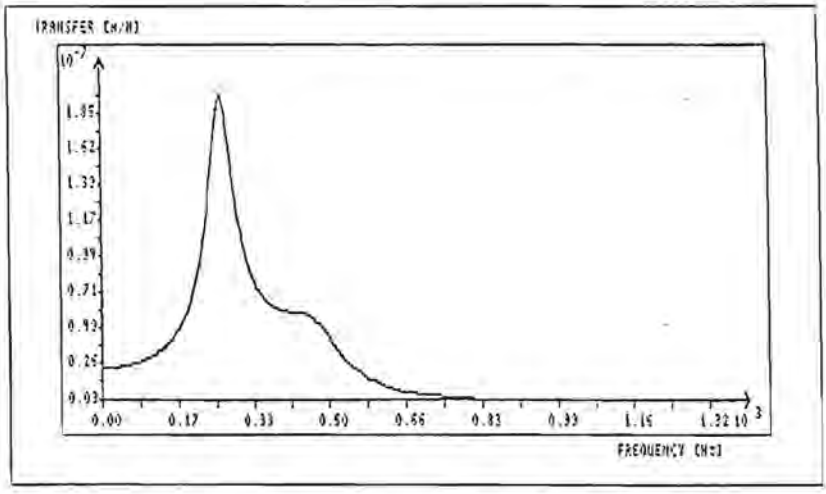

Fig.3.47b. The calculated transfer function of forces at point 3 (pulley) to displacements at point 7 (work-piece).

The mode shape and the dynamic compliance at 268 Hz can only be obtained if the stiffness of the supports is about $2*10^7$ N/m. This value is very low and, as the stiffness of the supports and the base are normally much higher (> $5*10^7$ N/m), this must be due to bad connections of the components. However, the parts, which can be examined without dismantling the construction, did not show any irregularities.
Anyway, the stiffness can certainly be increased. If it is increased to $5*10^7$ N/m, then the dynamic compliance will be reduced by 50% to about 90 nm/N (Fig.3.48).

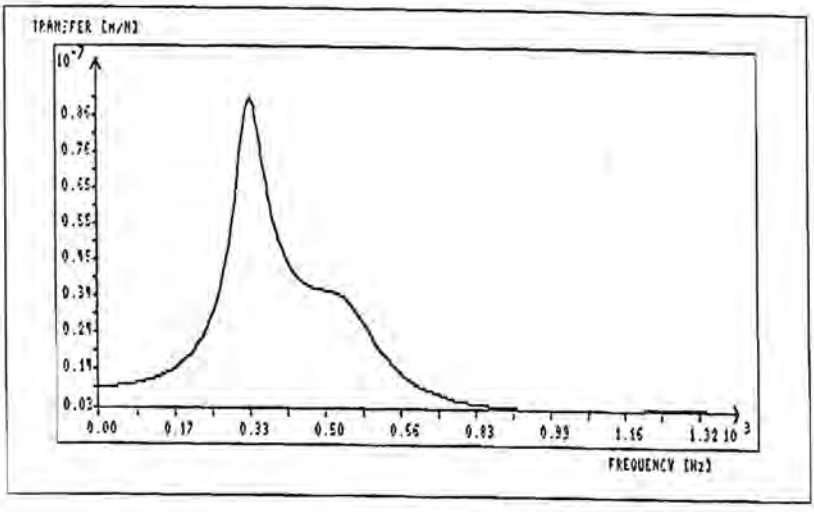

Fig.3.48. The calculated transfer function of forces at point 3 (pulley) to displacements at point 3 (work-piece) for a spindle with a higher stiffness ($5*10^7$ N/m) of the supports

Another improvement of the dynamic behaviour of the spindle may be the application of a long slender shaft for driving the spindle (Fig.3.49).

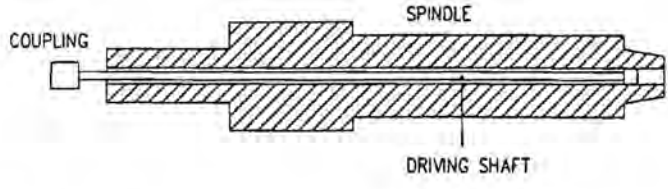

Fig.3.49. The slender shaft for driving the spindle.

This shaft will be weak for bending, but sufficiently stiff for torsion in order to drive the spindle. Force variations due to slip of belts are avoided and the low stiffness for bending will give a small transfer of vibrations of the motor to the work-piece.
For example, when the diameter of the shaft is 6 mm and the length is 500 mm the compliance at the coupling of the motor to the shaft is about 3 mm/N. The transfer of forces at this coupling to displacements of the work-piece is about 10 nm/N, so a displacement of 1 mm of the motor will give a displacement of about 10/3 = 3.3 nm of the work-piece, which is rather small. However, these are values for static displacements.
The transfer of forces at the low natural frequency of 6.4 Hz of the shaft will be more than 100 nm/N when the damping ratio is less than 5%. Hence, vibrations of the motor at this frequency can give unacceptable vibrations of the work-piece. Therefore, these frequencies should be avoided by chosing the appropriate rotational speed of the motor or the shaft should be well-damped by immersing it in grease.

3.6 Conclusions

1. The structural behaviour of the lathe is not optimal.
2. The weak elements are:
   a. the joints of the active and passive element of the carriage;
   b. the beams which connect the elements of the carriage;
   c. the supports of the spindle and
   d. the tool holder.
3. The displacements of the tool with respect to the work-piece, due to variations in forces on the pulley and cutting forces, can be untolerable (> 50 nm).
4. The behaviour of the lathe can be improved by means of a simple numerical model, which makes use of experimental data.

5. The influence of force variations can be reduced by (a) increasing the thickness of the bars which connect the active and the passive unit of the carriage, (b) increasing the stiffness between the shaft and the cylinder of the active unit, (c) using stiffer couplings between the bars and shafts of the units of the carriage, (d) increasing the stiffness of the supports of the spindle and (e) applying a slender shaft for driving the spindle. These modifications may lead to reductions of even 50%.

References

3.1. Proceedings of the 8th International Seminar on Modal Analysis. Leuven, September 1983.

3.2. User's Guide 5423A Structural Dynamics Analyzer, Volume 1. Hewlett Packard Company 1979.

3.3. The Fundamentals of Signal Analysis. Hewlett Packard Application Note 243.

3.4. E.O. Brigham: The Fast Fourier Transform. Prentice Hall, 1974.

3.5. G. Bouwhuis, J.J.N. Braat: Applied Optics 17, 1983 ,p.1993.

3.6. M. Paz: Structural Dynamics, Theory and Computation. Van Nostrand Reinhold Company, 1985.

4 SURFACE ROUGHNESS IN SINGLE-POINT DIAMOND TURNING

4.1 Introduction

The aim of metal cutting with a diamond tool is to give a fine finish to products of which the average peak-to-valley height (R_z) should be less than 0.1 μm and can be even 0.01 μm. This is very accurate, but can be achieved nowadays. However, as the understanding of the cutting process is still insufficient, the optimal cutting conditions are not well-defined yet.

The surface generation is a combination of several processes with many interactions between the parameters involved in cutting.

It starts with the separation of chip material from the work-piece material. The parameters of importance for the surface quality are the position and the form of separation. These depend upon the position of the tool with respect to the work-piece, the geometry of the cutting edge of the tool and the properties of the work-piece material.

The position of the tool with respect to the work-piece, which will be referred to as relative position, is determined by the operational settings of the lathe and their variations. These settings are the rotational speed, the depth of cut and the feed velocity. Their variations are due to (1) geometric and thermally induced errors of the machine elements, (2) vibrations and (3) cutting forces.

These forces are determined by the areas of contact between the work-piece and the tool (Chapter 2) and by the stress distributions over these areas. These, in their turn, depend upon the relative position, the geometrical characteristics of the tool and the work-piece, the deformations and the mechanical properties of the work-piece material.

The form of separation depends upon (1) the shape of the cutting edge of the tool, (2) the spacing, shape and size of the micro-voids and (3) the orientations of the cristallites [4.1]. Usually, the end point of separation does not coincide with a point at the cutting edge and consequently the surface profile will not be an exact 'fingerprint' of the shape of the cutting edge.

Deviations of this shape are due to micro-voids, inclusions, alternative slip of the work-piece material, built-up edges and Spanzipfels. Micro-voids and inclusions can cause large dimples (Fig.4.1) and scrathes (Fig.4.2) on the surface and alternative slip will yield slip steps (Fig.4.3). As deformation is easier in certain glide planes the form of these steps will depend upon the orientations of the cristallites. The gradual growth and rapid decay of the size of the built-up edge causes a sawtoothed surface (Fig.4.4).

Fig.4.1. The dimple formation model.

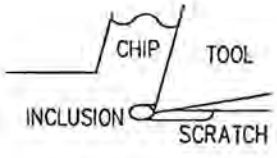

Fig.4.2. The scratching of an inclusion.

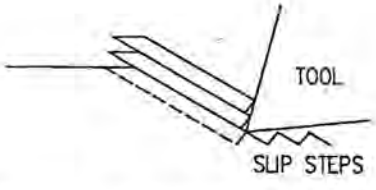

Fig.4.3. Alternative slip of the work-piece material resulting in slip steps.

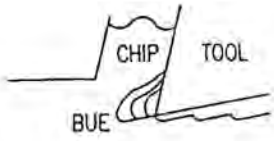

Fig.4.4. The sawtoothed surface caused by the built-up edge.

The Spanzipfel [4.2] is the portion of material left behind on the surface due to the existence of a minimum undeformed chip thickness below which a chip will not be formed (Fig.4.5).

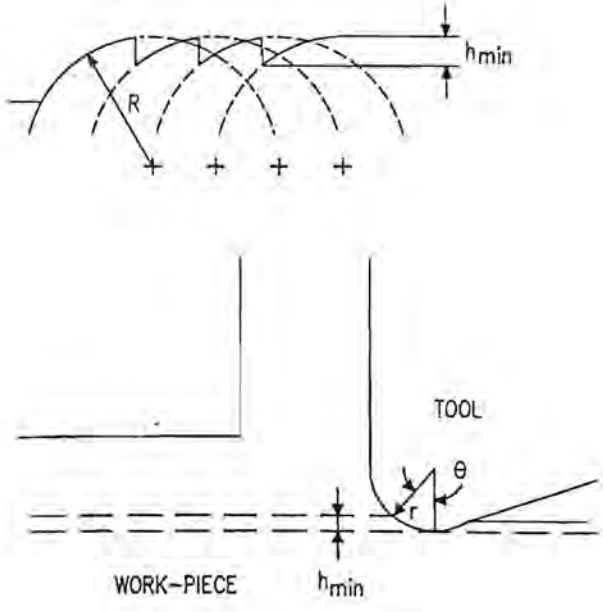

Fig.4.5. The Spanzipfel due to the existence of a minimum depth of cut (h_{min}).

SURFACE ROUGHNESS

The surface roughness, caused by the waviness of the tool edge and the early mentioned factors, can be more than 0.1 μm. This would be untolerable for most of the products made by single-point diamond turning. Fortunately, the separation process is followed by a sliding process at the clearance face, which smoothes the surface. The amount of smoothing depends upon the geometry of the tool and will be small, if the tool is sharp and the clearance angle is large. Then, the contact area between the tool and the work-piece material is small and most irregularities will not be smoothed-off. This can be avoided by applying a tool with two clearance angles, of which the first one is about zero degree or even negative. A tool with flank wear will look like such a tool and consequently, it will give a larger amount of burnishing than a sharp tool. This is the reason why a worn tool may produce smoother surfaces than a sharp tool.

The amount of burnishing has also an upper limit. If it is larger than necessary, then the height levels of the crystal grains will differ. This is due to the different crystallographic orientations of the grains.

After the burnishing the material springs back. This spring-back is determined by the forces on the clearance face and the Young's Modulus, which depends upon the crystallographic orientation of the grain. Different orientations will give different spring-backs [4.3] and thus difference in height levels (Fig.4.6). If the area of contact between the tool and the work-piece at the clearance face increases, the forces and, consequently, the difference in height level increases too.

Another contribution to surface roughness is the side flow of the material (Fig.4.7) [4.4].

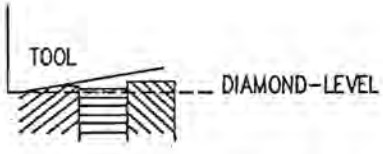

Fig.4.6. The surface roughness caused by the anisotropy of material behaviour.

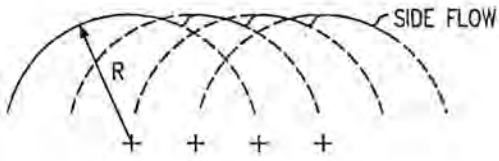

Fig.4.7. Side flow of the work-piece material.

It is clear that the surface generation is a complex process involving many interacting factors. Therefore, simple relationships for predicting the surface topography, such as the following, may not be very exact.

$$R_t = \frac{f^2}{8R} \qquad (4.1)$$

where f = feed
R = tip radius of the tool

A model, which includes the most important interactions between the parameters and the influences of these factors upon the surface roughness, will give more accurate predictions. Such a model is useful for optimizing manufacturing operations, including the development of a simple machine tool condition monitoring. Existing methods used for condition monitoring involve the use of expensive vibration analyzers with skilled personnel to assess the results and to make a judgement of the machine tool capability, while the machine has to be taken off production for some time. This can be omitted, if it is possible to distinguish among the types of deviation from the ideal shape at the surface of a work-piece. Then, the type, magnitude and location of machine tool errors can be extracted from the surface of the work-piece and the condition monitoring can be done by means of an in-process measurement of the surface finish without stagnation of the production process. Another advantage of this method of monitoring will be the detection of machine-tool detoriation before it is detrimental.

A model for estimating the surface roughness will be discussed and evaluated in the following sections. This model will also be used for simulating the influence of several types of machine tool errors upon the surface texture. These simulations must reveal whether it is possible to distinguish among type of errors and how surfaces should be analyzed in order to obtain reliable information about the machine tool condition.

4.2 The model

The model is a computer model which uses an iterative process for determining the displacements of the tool with respect to the work-piece, which are caused by the operational settings of the machine and their variations due to vibrations, geometric errors and cutting forces [4.5].
The following parameters are included in the model:

a the operational settings of the machine:
- the number of revolutions;
- the feed velocity;
- the depth of cut;

b the geometric characteristics of the cutting tool:
- the tool radius;
- the radius of the cutting edge;
- the flank wear;
- the waviness of the cutting edge;

c the properties of the work-piece:
- the specific stress;
- the surface topography;

d the coefficient of friction on the flank and on the face;

e vibrations transferred from sources of vibration such as the motor to the tool and work-piece;

f the stiffnesses between work-piece and cutting tool.

The model can be developed for simulating several cutting operations. However, since the important characteristics of surface generation can be determined from simple plain turning tests, it is not necessary to consider all kind of operations. Therefore, the attention will be restricted to plain turning.
One parameter of importance for the surface profile along a line parallel to the axis of the work-piece is the position of the tool with respect to the work-piece at the moment that the cutting edge crosses this line. In order to calculate this position after i revolutions of the work-piece, the following steps are performed:

1. Computation of the time t_i for i revolutions of the work-piece. It depends upon the rotational speed and is derived via an iteration process from the following relationship:

$$i = \int_0^{t_i} \left(n_o + \sum_{j=1}^{m} n_j . \sin(\omega_{nj} t + \varphi_{nj})\right) . dt \qquad (4.2)$$

where n_o = average number of revolutions

n_j = amplitude of the j^{th} variation in the number of revolutions

ω_{nj} = radial frequency of the j^{th} variation in the number of revolutions

φ_{nj} = phase of the j^{th} variation in the number of revolutions

2. Calculation of the position of the tool due to the operational settings and their variations (Fig.4.8).
The x-position (Xo_i) is determined by means of the following equation:

$$Xo_i = \int_0^{t_i} v_f(t) . dt \qquad (4.3)$$

where v_f = the feed velocity.

The relationship for the y-position (Yo_i) is :

$$Yo_i = R_w + R - b(t_i) \tag{4.4}$$

where R_w = radius of the work-piece
R = tip radius of the tool
b = depth of cut

The expressions for the feed velocity and the depth of cut are similar to that for the number of revolutions:

$$v_f(t) = v_{fo} + \sum_{j=1}^{m} v_{fj}.\sin(\omega_{vj}t + \varphi_{vj}) \tag{4.5}$$

$$b(t) = b_o + \sum_{j=1}^{m} b_j.\sin(\omega_{bj}t + \varphi_{bj}) \tag{4.6}$$

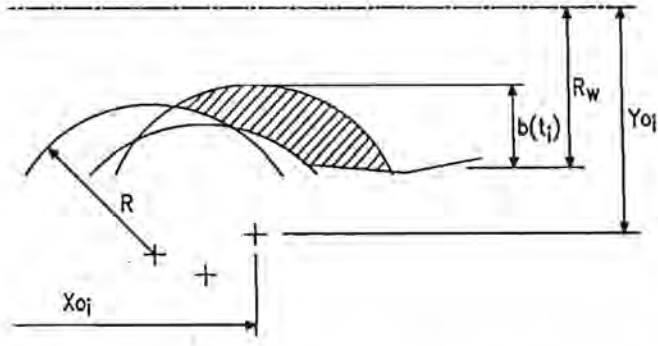

Fig.4.8. The position of the tool with respect to the work-piece and the undeformed chip section without correction for the influence of the cutting forces.

3. Calculation of the cutting forces.
The displacements of the tool relative to the work-piece due the cutting forces are not included in the determination of the position (Xo_i.Yo_i).
In order to correct for these displacements the cutting forces should be determined. These are calculated by means of the relationship derived in chapter 2.

$$F_w' = F_w + \Delta F_w = \frac{\mu_r}{1-\mu_r}.C.A + A_{VB}.C \tag{2.58}$$

The cutting force F_v' will give displacements in the z-direction and is not important for the determination of the x-y position. Therefore, this force is not taken into account.
The area of the undeformed chip section (A) depends upon (Fig.4.8):

+ positions of the tool relative to the work-piece in the i^{th} and preceding revolution(s);
+ the depth of cut;
+ the surface profile of the work-piece before cutting;
+ the profile of the cutting edge;

The relationships for the force components in x- and y-direction are:

$$F_x = F_w'.\sin(\kappa) \tag{4.5}$$

$$F_y = F_w'.\cos(\kappa) \tag{4.6}$$

The direction of chip flow is assumed to be from the middle of the width of contact between the cutting edge of the tool and the work-piece to the middle of the tool.

4. Determination of the additional displacements due to the cutting forces.
The additional displacements ΔX_{f_i} and ΔY_{f_i} are calculated by multiplying the force components by the compliances between the work-piece and the tool. These displacements are changing the position of the tool with respect to the work-piece and with that, the area of the undeformed chip section (Fig.4.9) and, thus, the cutting forces. Therefore, the calculation of the area of the undeformed chip section, the cutting forces and subsequent displacements is repeated until the difference between the positions calculated in two successive iteration steps is less than 0.1 nm.

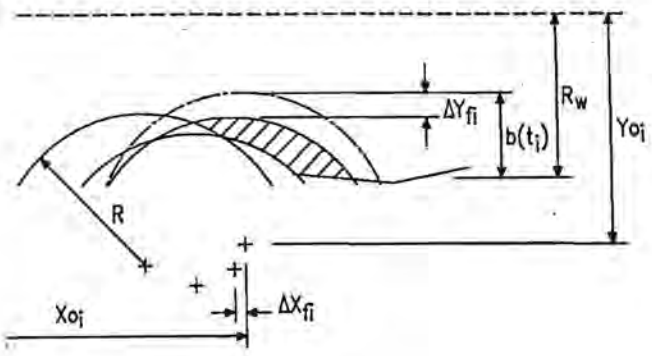

Fig.4.9. *The position of the tool relative to the work-piece and the undeformed chip section corrected for the influence of the cutting forces.*

The final position and the profile of the cutting edge are used for determining the surface profile.
It should be remarked that the history of cutting forces and displacements in the time interval of one revolution is missing in the calculations. Consequently, the influence of parameters, which cause highly frequent force variations, such as impurities of the work-piece material, cannot be simulated. Besides, the assumption is made that the phase between the force and the displacement is zero, which is only true for a limited range of conditions. Hence, the method may give poor estimations. Therefore, turning tests have been carried out in order to evaluate the model. The experimental set-up and the results are described in the following section.

4.3 Experiments

In order to evaluate the model, turning tests with aluminium and brass were carried out on the precision lathe. The experiments also included the determination of the magnitude of the input parameters. Firstly, the operational settings, namely the rotational speed, the feed velocity and the depth of cut, will be considered.

The test conditions were:
- number of revolutions : 300 - 2400 rpm
- feed velocity : 50 - 300 μm/s
- depth of cut : 5 - 20 μm

Besides the mean value, the variations of these settings should be known.
An examination of the rotational speed showed that the variation of the time per revolution of the work-piece was less than 1%. The time per revolution was measured by means of the optical sensor and the HP 5423A Structural Dynamics Analyzer (See Chapter 3 for description of these instruments).
A small groove was made along the surface of the work-piece in order to create a reference for the measurements.
A variation of less than 1% of the rotational speed will result in a variation of less than 1% in the feed rate. By means of Eq.(4.1) it can be derived that this variation will give an alteration of the surface roughness (R_t-value) of less than 2%:

$$R_t = \frac{(f+\Delta f)^2}{8R} = \frac{(f+0.01f)^2}{8R} \approx 1.02\,\frac{f^2}{8R} \qquad (4.7)$$

As this is rather small and the facilities for an accurate measurement of the amplitude and frequency of the variations were lacking, these variations were not included in the calculations.

The variation in the feed velocity was analyzed by means of a Brüel & Kjær 4381 accelerometer. An autopower spectrum of the feed velocity is depicted in Fig.4.10. It shows remarkable components at 3.1 Hz with an amplitude of about 10 μm/s and at 10.8 Hz with an amplitude of about 20 μm/s.

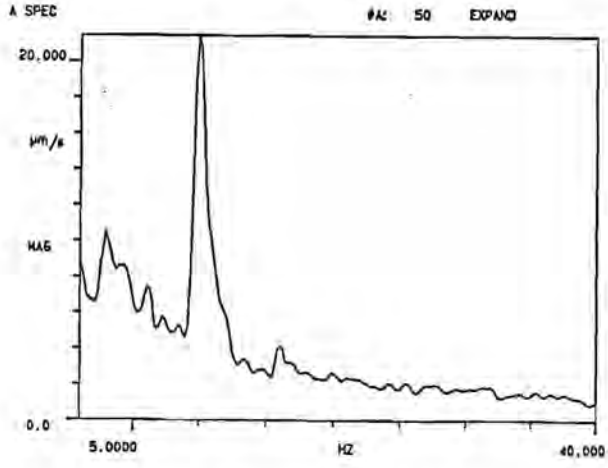

Fig.4.10. Autopower spectrum of the feed velocity.

The depth of cut is influenced by the vibrations of the tool and the work-piece, transferred from the motor, the foundation and the hydraulic system, and by the misalignment of the carriage and the spindle.
The optical sensor was also used for measuring the vibrations of the work-piece with respect to the tool. The displacements of the work-piece with respect to the tool as a function of time, at a number of revolutions of about 600 rpm, is shown in Fig.4.11.

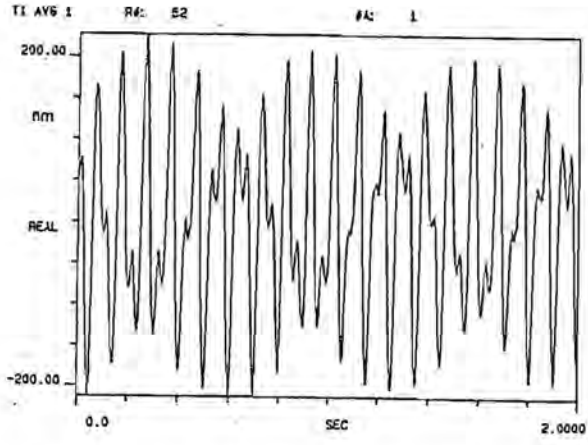

Fig.4.11. The displacement of the work-piece relative to the tool as function of the time.

The main components are a vibration with an amplitude of about 150 nm and a frequency of about 10 Hz and a vibration at 1.5 Hz with an amplitude of about 30 nm. These vibrations are mainly due to instabilities in the driving system and in the hydraulic units (bearings) of the spindle. The frequency of 10 Hz corresponds to the rotational speed of the work-piece and the displacements at this frequency will result in roundness errors of the work-piece. With respect to the surface roughness along a line parallel to the axis of the work-piece, the vibration at 1.5 Hz is more important. The amplitude and frequency of this low frequent vibration depend upon the rotational speed and will be larger, if the rotational speed is higher. At a rotational speed of 2400 rpm, the amplitude is about 150 nm and the frequency is about 4.5 Hz.
Since the results of alignment tests are missing, in the first instance the influence of misalignments is not included in the calculations.

The next input parameter is the geometry of the tool, especially the profile of the cutting edge and subsequent profiles along the clearance face.
These profiles were measured by means of the optical sensor on an apparatus of which a schematic diagram is shown in Fig.4.12. This apparatus has a measuring range of 150 mm in horizontal direction and 100 mm in vertical direction [4.6]. The positioning accuracy is about 0.1 μm in both directions.

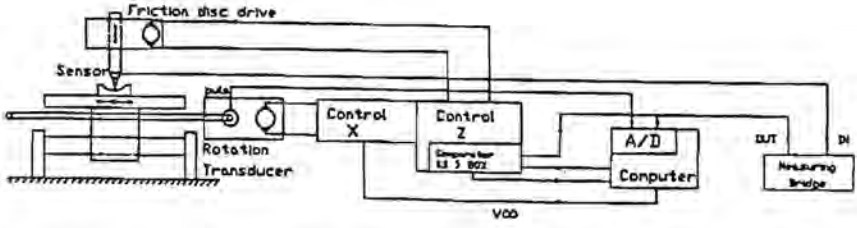

Fig.4.12. Schematical representation of the roughness and shape measuring equipment.

Fig.4.13a shows a measured profile of a tool with a tip radius of approximately 1 mm. This radius can be determined from the measured profile by means of the following equation :

$$R = \frac{4y^2 + x^2}{8y} \qquad (4.8)$$

where R = tip radius
y = height of the profile
x = length of the profile

A few components of the waviness of the tool edge can be determined from the measurements too, by means of filtering and Fourier Transform. Fig.4.13b shows the autopower spectrum of the filtered signal, which has a significant peak at about 15 cycles/mm, corresponding to a wave length of 67 μm. The amplitude of this component is about 0.08 μm.
In the experiments a tool with a tip radius of 0.2 mm was used too.

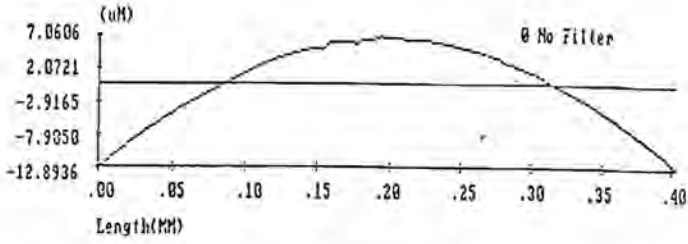

Fig.13a. The profile of the cutting edge of the tool with a radius of about 1 mm.

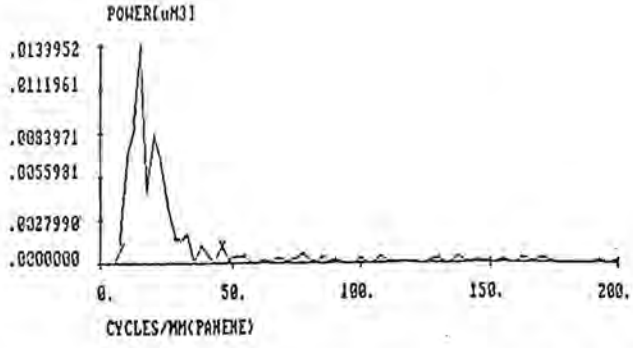

Fig.4.13b. The autopower spectrum of the filtered profile of the cutting edge.

The input values for the specific stress (C) and the friction coefficient between the tool and the work-piece (μ_r), which are needed for calculating the cutting forces, are based on the results of the experiments described in chapter 2. The value for the specific stress is about twice the value obtained from tensile tests and the friction coefficient is about 0.2.

In order to determine the additional displacements of the tool relative to the work-piece caused by cutting forces, the dynamic compliances between the work-piece and the tool should be known. These are shown in Fig.4.14 and Fig.4.15. The method for determining the frequency responses are described in chapter 3. The compliance in y-direction is approximately constant and about 120 nm/N.
That in x-direction varies strongly and the error in the additional displacement X_{f1} may be large, if the compliance is taken to be constant.
However, for most cutting conditions the variation in forces in this direction and consequently, the error in X_{f1} is small. When a constant compliance of 40 nm/N is assumed and the magnitude of the force variation is 25 mN, which is extremely high, the maximum error in X_{f1} is 1 nm.
This will hardly influence the roughness in the y-direction.

A

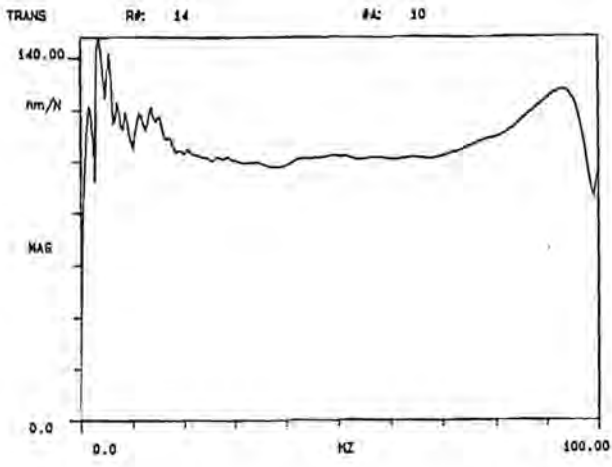

B

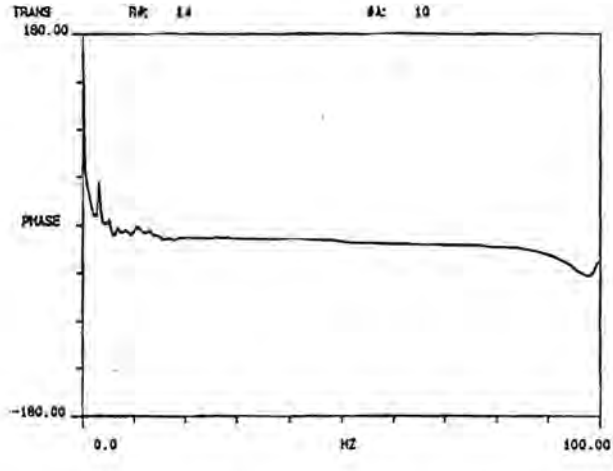

Fig.4.14. The magnitude (A) and phase (B) of the transfer function of cutting forces to displacements of the tool relative to the work-piece in y-direction.

A

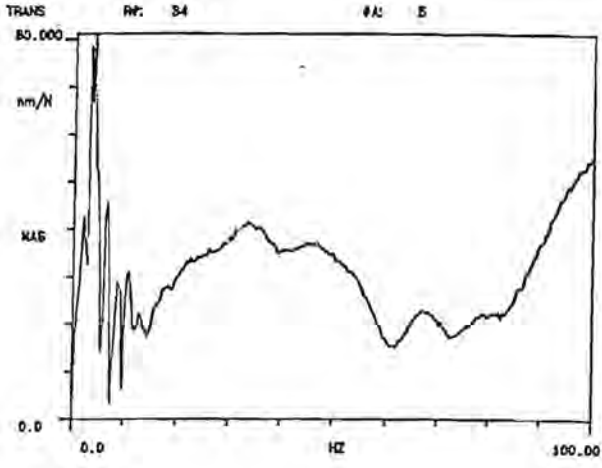

B

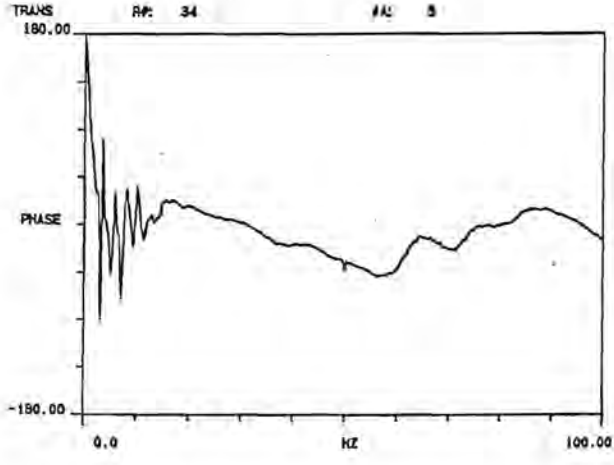

Fig.4.15. *The magnitude (A) and phase (B) of the transfer function of cutting forces to displacements of the tool relative to the work-piece in x-direction.*

SURFACE ROUGHNESS

The equipment for measuring the tool geometry was also used for measuring the surface roughness. Both optical and stylus techniques were available.

The noise level of the optical pick-up system is about 15 nm and the minimum spatial wavelength is about 3.5 μm [4.7]. The surface slope should be less than 10 degrees in order to reflect a sufficient amount of light to the photo diodes.

If the surface slope is steeper, the focus error cannot be detected. This will result in undesirable drift of the signal and, thus, large errors in the measured profile.

The accuracy of the measurement with the stylus instrument (Talysurf) depends upon the stylus loading, the radius of the tip, the included angle of the stylus, the slopes of the irregularities and the hardness of the work-piece material. For single-point diamond turned surfaces, where the slope is mostly less than 3^{o}, the measuring error due to the dimensions and the indentation of the stylus will be less than 20 nm (Appendix 4.A).

The tip radius is about 2 μm. Hence, the lateral resolution is about 1.4 μm (Appendix 4.A).

If the slopes of the surface irregularities are less than 10 degrees, the difference in the measured roughness value between the optical and the stylus instrument will be less than 20%. However, if the slopes are steeper, the drift of the signal of the optical instument can cause errors with a magnitude of even more than 0.5 μm (Fig.4.16) and the difference will be more than 100%.

For this reason, only the stylus instrument has been used.

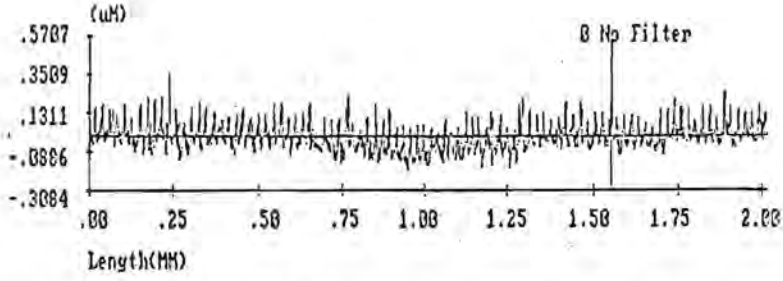

Fig.4.16. The surface profile measured by means of the optical sensor.

4.4 Comparison of calculated and measured profiles.

A satisfactory agreement between experimental and numerical results is illustrated in Figs.4.17 to 4.21. The differences between the calculated and measured roughness values (R_t, R_a and R_q) are less than 10% in most instances.

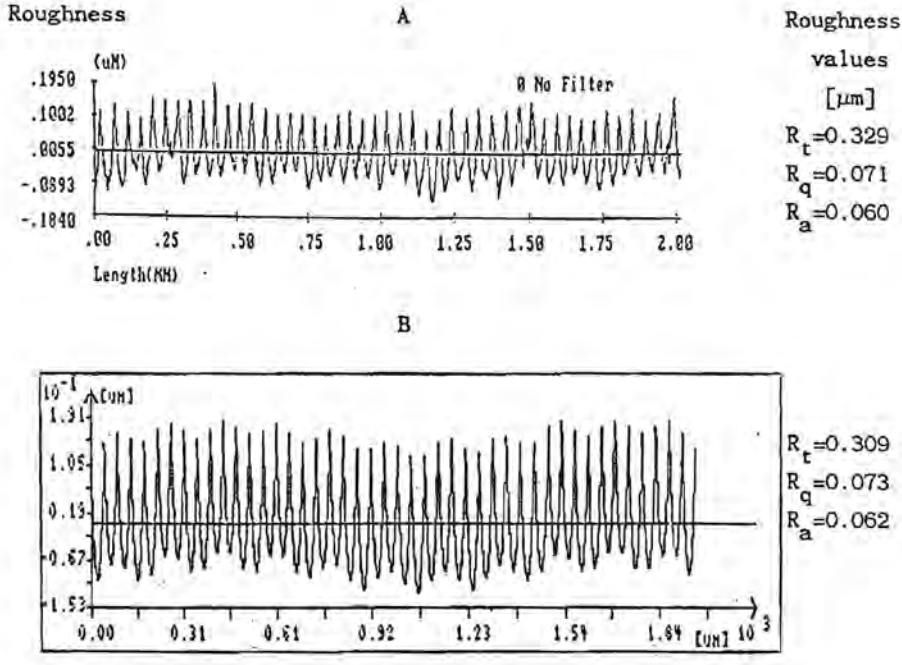

Fig.4.17. The measured (A) and calculated (B) surface profiles of a brass work-piece.

Feed velocity	:	200 μm/s;
Number of revolutions	:	300 rpm;
Tool radius	:	1.0 mm;
Depth of cut	:	10 μm.

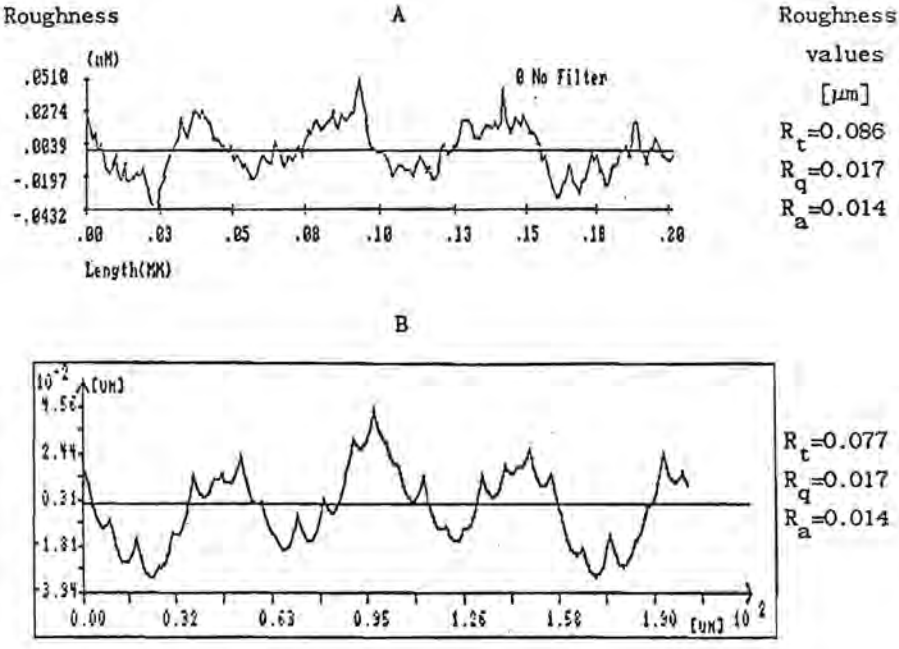

Fig.4.18. *The measured (A) and calculated (B) surface profiles of a brass work-piece.*

Feed velocity : 60 μm/s;
Number of revolutions : 600 rpm;
Tool radius : 1.0 mm;
Depth of cut : 5 μm.

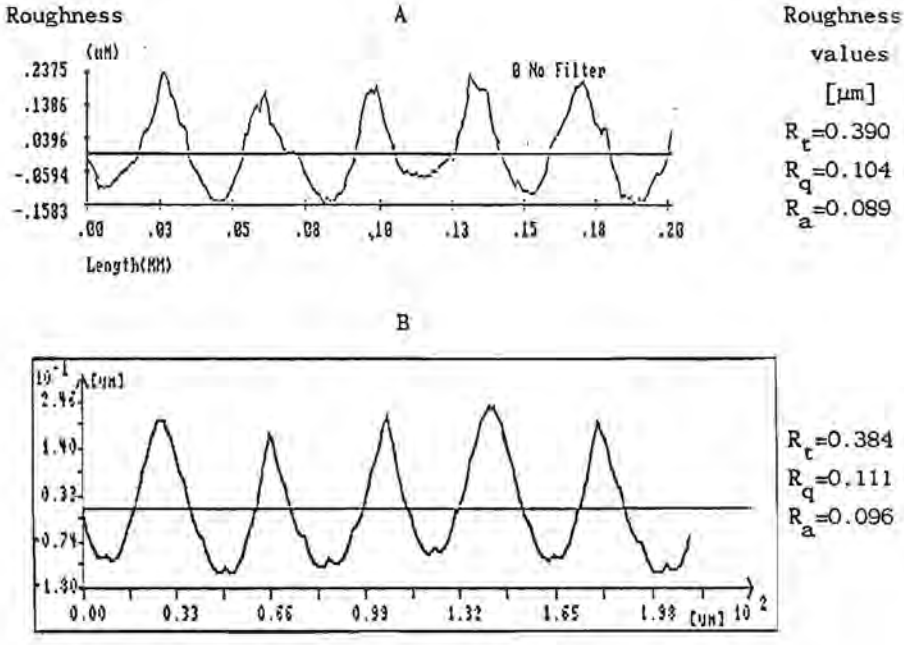

Fig.4.19. The measured (A) and calculated (B) surface profiles of an aluminium work-piece.

Feed velocity	:	170 μm/s;
Number of revolutions	:	2400 rpm;
Tool radius	:	0.2 mm;
Depth of cut	:	10 μm.

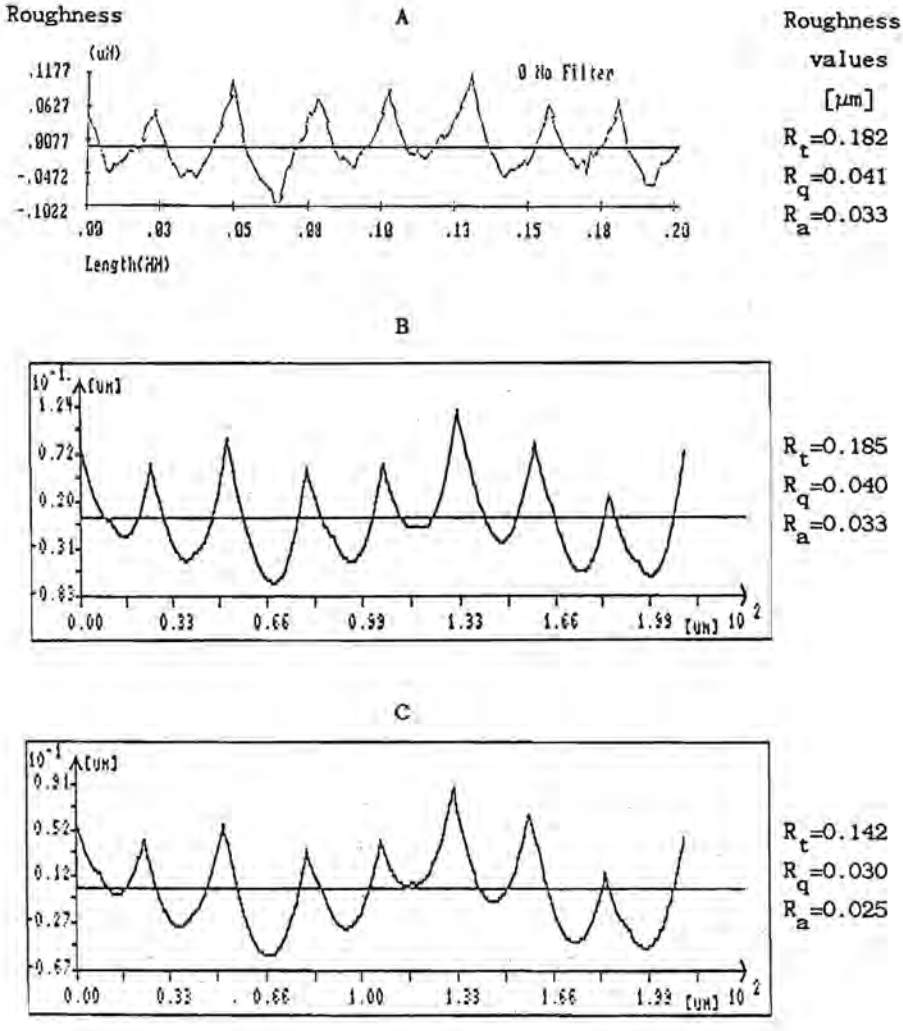

Fig.4.20. The measured (A) and calculated surface profiles of a brass work-piece with (B) and without (C) a wavy tool edge.

Feed velocity : 120 µm/s;
Number of revolutions : 2400 rpm;
Tool radius : 1.0 mm;
Depth of cut : 10 µm.

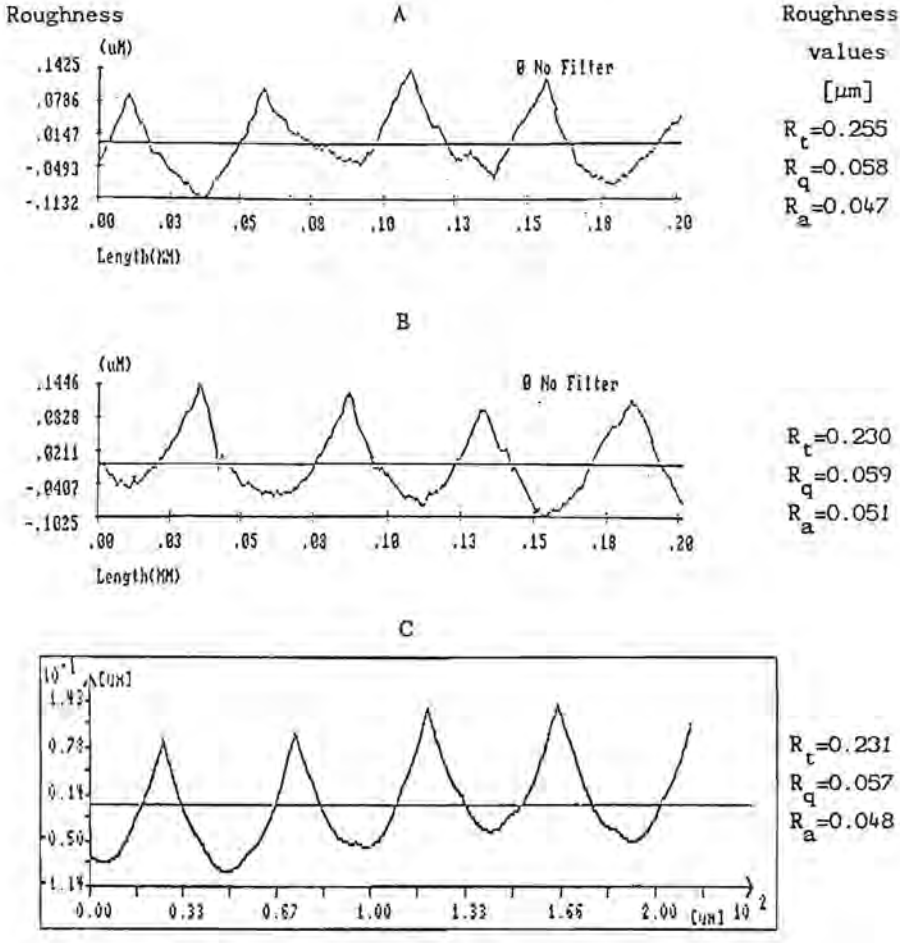

Fig.4.21. The measured surface profile of a brass (A) and an aluminium (B) work-piece and the calculated profile (C).

Feed velocity : 220 μm/s;

Number of revolutions : 2400 rpm;

Tool radius : 1.0 mm;

Depth of cut : 20 μm.

The deviations can be imputed to the omission of several features, including the following:

a Additional variations of the operational settings.
The main components of the variations, which occurred whilst measuring the behaviour of the lathe, were included in the calculations. Small components and other fluctuations that could have occurred when machining the test-pieces, due to, for example, slipping of the belts, were not taken into account.

b Metallurgical properties of the work-piece material.
Any roughness due to voids and impurities, as well as, anisotropic material behaviour were omitted from the calculations.
The size of the voids and the impurities can be larger then 10 nm, consequently, the depth of the dimples and the scrathes caused by these imperfections of the work-piece material may be considerable. However, since the dimensions and the positions of these and the levels, where they are cut by the tool, are not predictable, it will be difficult to include their influence on the surface roughness in the calculations. Besides, the complexity of the problem is increased by the influence of the burnishing process at the clearance face on the dimple and scratch formation.
A rough approximation of the order of magnitude of the roughness due to anisotropic elasticity of the work-piece material can be obtained by a simple calculation of the elastic recovery, due to the release of the same load, of two crystals with the same height, but different orientations.
The elastic strain in the crystal due to the load can be calculated from:

$$\epsilon = \frac{\sigma}{E} \qquad (4.9)$$

where: ϵ = elastic strain
σ = stress on the crystal
E = Young's modulus of the crystal

The elongation of the crystal is determined by multiplying the strain by the height.
A feasible value of the stress (σ) is that of the mean stress on the clearance face, which is about double the specific stress (See chapter 2).
Therefore, a value of 1000 N/mm^2 will be used for the calculations.
The Young's modulus of an aluminium crystal is in the lattice direction [100] about 63000 N/mm^2 and in the lattice direction [111] about 75000 N/mm^2. If the height of the crystals is 10 μm, the difference in elongation of two crystals oriented in the above mentioned directions will be about $\left[\frac{1000}{63000} - \frac{1000}{75000} \right] * 10 =$ 0.025 μm = 25 nm. This means that, if the size of the crystals is large, it may be necessary to include the influence of the anisotropic material behaviour. However, this will be cumbersome, due to the large number of crystals to be considered.

The imperfections and the anisotropy in the crystals give rise to variations of the cutting forces too. These may result in variations of several nanometres in the surface profile, if the components at the natural frequencies of the machine tool are large.

c Roughness of the work-piece before cutting.
The initial roughness of the work-piece will cause force variations, which will alter the final roughness. A initial roughness of several microns (R_t-value) may cause force variations with an order of magnitude of 10 mN. It results in variations in the surface profile with a magnitude of several nanometres.
An example will be given in section 4.6.

d The Spanzipfel and the side flow.

The contributions of the Spanzipfels and the side flow to the surface roughness were not taken into account, because of the complexities associated with their determination.
The Spanzipfel is determined by the minimum depth of cut and the geometry of the undeformed chip section. The minimum depth of cut depends on the geometry of the area of transition from the rake face to the clearance face and on the stress distributions around this area. Since these parameters are not easy to determine, it is difficult to quantify the minimum depth of cut. Several investigations [4.8-4.10] showed that if the rake angle of the tool is less than about -75° a chip will not be formed and if a tool with a rounded edge (Fig.4.5) is used the angle, which indicates the level of the minimum depth of cut (θ), will be about 15°. This means that for an edge radius (r) of 0.1 μm, the minimum depth of cut is about 3 nm. In the experiments, the radius was larger, due to a rapid break down of the edge. Hence, the minimum depth of cut could be consirable (> 10 nm). But, the portion of material which is not formed into a chip will flow beneath the tool and will be plastically deformed by the clearance face. It may be expected that the height of the Spanzipfel will be reduced. The problem in determining the contribution to the surface roughness is that the reduction rate is not known. According to the principle of volume invariancy from plasticity theory, the level of the material behind the rubbing area should be the same as just before the cutting edge, provided that there is no side flow. However, the Spanzipfel is formed in a region where side flow may not be neglected and, since the dimensions are very small and most materials will contain micro-voids, the principle of volume invariancy is questionable.

The contribution of side flow is even more difficult to model, because of the extra degree of freedom. Now the material can flow under the tool, to the side or in the chip flow direction (Fig.4.22). Besides, there is a lack of geometrical constraint.

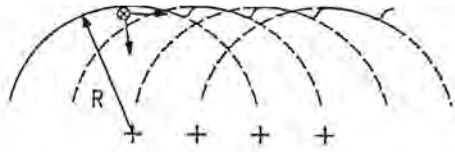

Fig.4.22. The directions of material flow in the neighbourhood of the Spanzipfel.

e Progress of the wear of the tool during machining.

Due to an increase of the tool wear during machining the test-pieces the actual profile of the cutting edge was different from the measured profile.

Another source of error could have been the value used for the phase angle of the sine wave in the calculations. This value cannot be predicted, so it has been approximated by a trial and error method. Hereby, the measured profile has been taken as reference. Since there are several variations, it is not easy to determine all values exactly.

This way of calculating the profiles is not a prediction any more, but it has been applied in order to indicate the potential accuracy of the calculations, which is rather high, since the difference between calculated and measured values is less than 10 %. This means that, at least in the range of surface roughness considered (peak-to-valley height 50 - 400 nm), good approximations of the surface profile can be made by means of the model and that the influence of parameters, which were not taken into account, was small.

Therefore, this model is very suitable for simulating the influences of diverse parameters. This will be done after an analysis of the measured profiles.

4.5 Analysis of the surface profiles

As can be seen in Fig.4.17, the roughness component due to the feed dominates when the feed rate is large (40 μm/r), but this component becomes less important when the feed rate is reduced (6 μm/r in Fig.4.18) and is difficult to see, if the amplitude of the vibrations increases at all (Fig.4.19). In Fig.4.19, the marks look like feed marks but in fact they were caused by vibrations with an amplitude of 150 nm and a frequency of 4.5 Hz. Together with the feed velocity this frequency will determine the wavelength according to:

$$\lambda = v_f/f \qquad (4.10)$$

where λ = wavelength of the marks on the surface
v_f = feed velocity
f = frequency of the vibration

In Fig.4.19, the wavelength is 170/4.5 = 38 μm. A smaller wavelength, which is accomplished by increasing the frequency or reducing the feed velocity, or a tool with a larger tip radius will give a smaller amplitude of the waveform of the surface profile (Fig.4.20). Since the amplitude of the vibration was about 150 nm, a peak-to-valley height of about twice the amplitude would be expected, but, actually, this height is 180 nm instead of 300 nm. This is not surprising when taking into consideration the fact that, due to overlapping, the surface profile is only determined by the upper positions of the tool. (Fig.4.23).

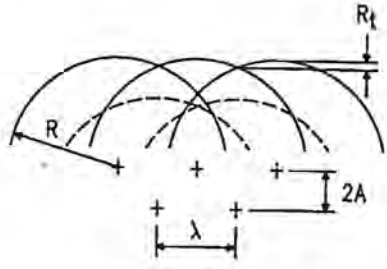

Fig.4.23. The generation of the surface profile when the amplitude of the vibration is large and the wave length is small.

It looks like cutting with a feed which is equal to the wavelength of the vibration. When no other vibrations are involved, the peak-to-valley height can be estimated from the following relationship:

$$R_t = \lambda^2/8R \qquad (4.11)$$

where R = tip radius of the tool

Thus, even if the amplitude of the vibration is large, smooth surfaces can be obtained by chosing a large tool radius and a small feed velocity.

Another important factor is the waviness of the cutting edge of the tool. Omitting this waviness (amplitude 80 nm and wavelength 67 μm) results in the estimated profile shown in Fig.4.20c with roughness values which are at least 20% less than those for the measured profile.

The influence of cutting forces upon surface roughness appeared to be quite small. Variation of the cutting forces by increasing the depth of cut or using other materials (Fig.4.21) did not affect the surface roughness remarkably. The differences in the surface profiles shown in Fig.6 are mainly due to differences in the phase angles of the wave forms.
The order of magnitude of the variations of cutting forces is 10 mN and the compliance between the work-piece and the tool is about 0.1 μm/N, so the roughness due to variations of the cutting forces is only a few nanometres.

4.6. Simulation of the influence of diverse parameters

A machine tool monitoring system, that is based on the surface roughness of the work-piece [4.11-4.12], will be very useful for the optimum utilisation of machine and cutting tools, if it is possible to distinguish among type of errors.

Then, the source of the error may be easily located. Consequently, the time needed for the inspection by means of vibration analysers and/or the alignment test can be strongly reduced. This results in an increase in productivity.

The influence of some parameters will be simulated by means of the numerical program. These simulations must reveal whether each type of error will give a distinct feature on the surface.

Fig.4.24 shows the so-called 'ideal' turned surface profile at the following conditions:

- number of revolutions 1500 rpm
- feed velocity 250 μm/s
- depth of cut 10 μm
- tool radius 1 mm
- no variations in the operational settings and the profile of the cutting edge

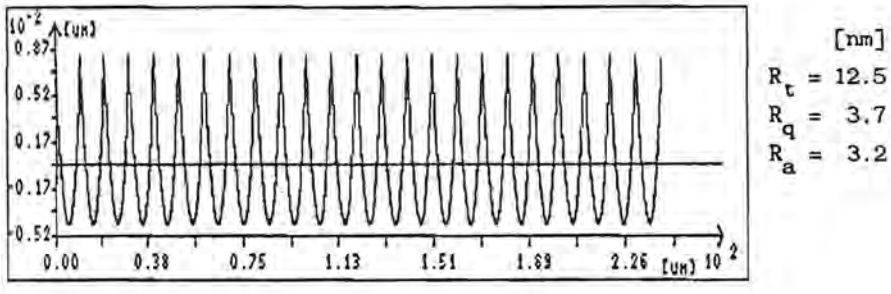

Fig.4.24. The 'ideal' turned surface profile.

A variation in the rotational speed with an amplitude of 5% of the mean value and a frequency of 5 Hz will result in the profile depicted in Fig.4.25.

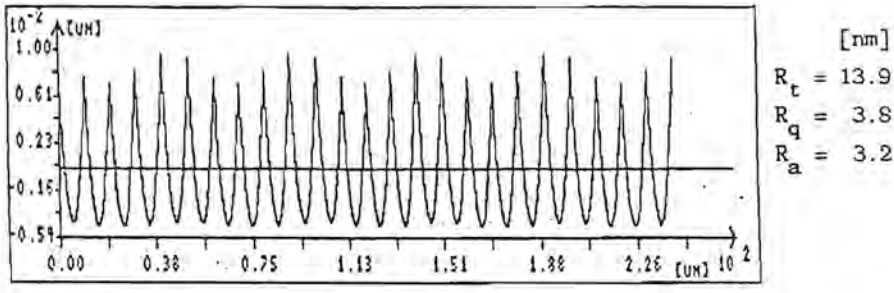

Fig.4.25. The surface profile when the rotational speed varies with an amplitude of 5% of the mean value and a frequency of 5 Hz.

The particular feature of this profile is that the valleys remain on the same levels while the peaks are varying.
A similar profile is obtained when a variation in the feed velocity with an amplitude of 5% of the mean value and a frequency of 5 Hz is introduced (Fig.4.26). This means, that it will be difficult to distinguish errors introduced by variations in the rotational speed from those due to instabilities of the feed velocity.

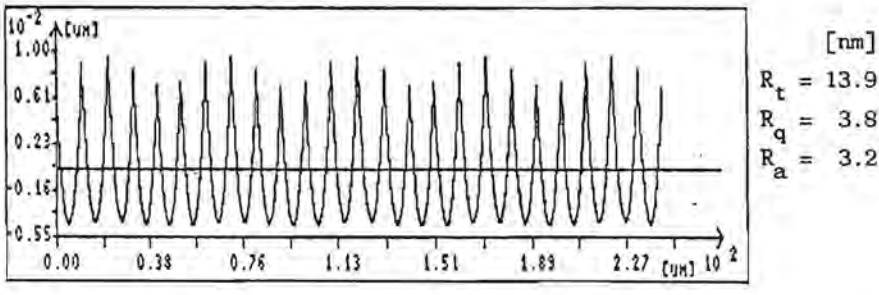

Fig.4.26. The surface profile when the feed velocity varies with an amplitude of 5% of the mean value and a frequency of 5 Hz.

When the depth of cut is varied by a vibration of the tool relative the work-piece with an amplitude of 5 nm and a frequency of 5 Hz, the profile will be as shown in Fig.4.27.

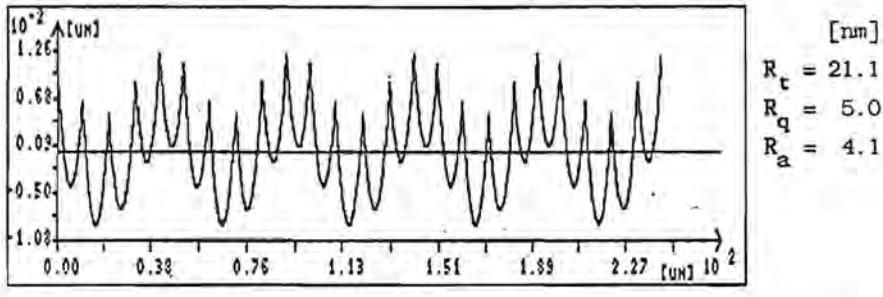

Fig.4.27. The surface profile when the depth of cut varies with an amplitude of 5 nm and a frequency of 5 Hz.

Now, both the peaks and the valley are varying in height level. So, this type of error can be distinguished from errors which are caused by feed or rotational speed variations. However, the vibration of the tool can be in both vertical (z) and horizontal (y) direction and may be caused by several factors, including the variation in the cutting forces due to variation in the properties of the work-piece and instabilities in the driving system and hydraulic units. Therefore, it is not possible to attribute this type of error to a certain cause of the variation in the depth of cut without additional information. This may be the magnitude and/or the frequency of the variation. The magnitude of variations in the depth of cut, due to variations in the cutting forces and vibrations of the tool in vertical (z) direction, is usually much smaller than those due to vibrations in the horizontal (y) direction. This can be shown by means of the following examples.

A rather large variation in the cutting forces can be simulated by introducing a waviness of the surface of the work-piece before cutting with a large amplitude. When this amplitude is 5 μm and the wavelength is 50 μm, the variation in the friction force is about 65 mN and the variation in the surface is less than 5 nm (Fig.4.28) for a compliance between the work-piece and the tool of 100 nm/N.

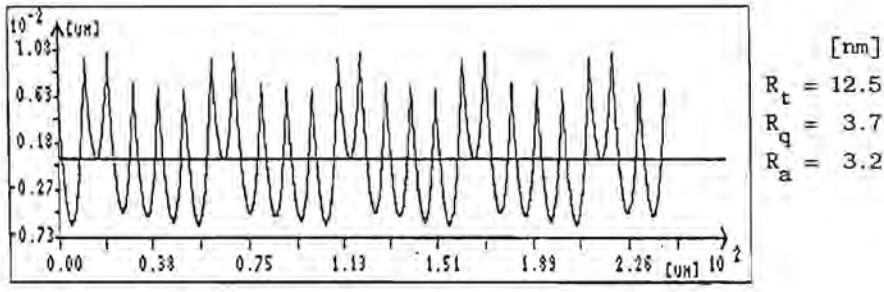

Fig.4.29. The surface profile when the initial profile of the work-piece varies with an amplitude of 5 μm and a wave length of 50 μm.

A vibration in the vertical (z) direction will result in a variation of the radius of the work-piece and, consequently, in the surface profile according (See Fig.4.29):

$$y(t) = \sqrt{[R_w^2 + (Z.\sin(\omega_z t))^2]} - R_w \qquad (4.12)$$

where R_w = radius of the work-piece
Z = amplitude of the vibration in z-direction
ω_z = radial frequency of the vibration in z-direction

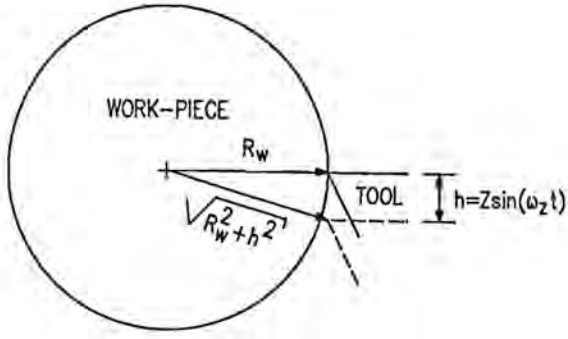

Fig.4.29. The variation of the radius of the work-piece due to a vibration in the z-direction.

The term containing the square root can be expressed in Taylor series. If the amplitude is very small with respect to the radius of the work-piece ($Z \ll R_w$), then higher order terms can be neglected and Eq.4.12 becomes:

$$y(t) = \frac{Z^2}{2R_w}.\sin^2(\omega_z t) = \frac{Z^2}{4R_w}.(1 - \cos(2\omega_z t)) \qquad (4.13)$$

This means that a vibration in the z-direction with an amplitude Z and a frequency ω_z will give a variation in the surface profile in the y-direction with an amplitude of $\frac{Z^2}{4R_w}$ and a frequency of $2\omega_z$. In practice, the radius of the work-piece is much larger than the amplitude Z and the magnitude of the variation in the y-direction due to the vibration in z-direction will be very small. For example, if the radius of the work-piece is equal to 10 mm and the amplitude (Z) is 10 μm, which is extremely large, then the amplitude of the variation in the y-direction will be 100/40000 μm = 2.5 nm.

Since the influence of variation in cutting forces and vibrations in the z-direction is small, a considerable variation in the depth of cut can be attributed to a vibration in the y-direction.

The influence of tool wear, in particular the fretting and chipping of the tool edge, can be simulated by adding a short term waviness to the profile of the edge. Fig.4.30 shows the profile of the surface turned by a tool which contains a waviness with an amplitude of 5 nm and a wavelength of 3 μm.

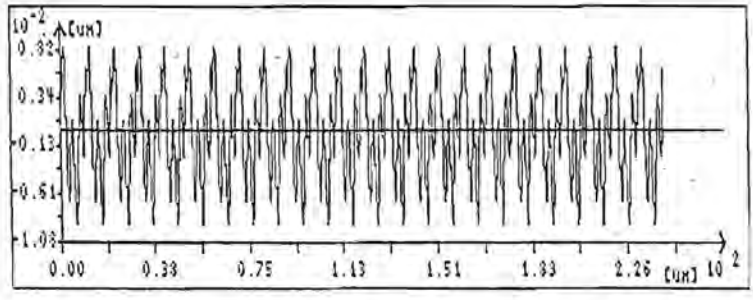

Fig.4.30. The surface profile when the profile of the cutting edge contains a waviness with an amplitude of 5 nm and a wavelength of 3 μm.

If the lateral resolution of the measuring instrument is small, then the short term variations in the surface can be detected and the cutting tool condition can be easily monitored. However, long term waviness of the tool edge cannot always be assessed from the surface. For example, the surface profile will not show any remarkable, distinct feature for a wavelength of 50 μm, even if the amplitude is 50 nm (Fig.4.31). The only difference with respect to the ideal turned surface is the magnitude of the peak-to-valley height.

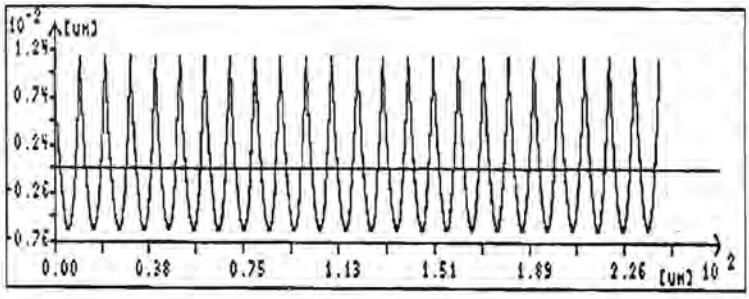

Fig.4.31. The surface profile when the profile of the cutting edge contains a waviness with an amplitude of 50 nm and a wavelength of 50 μm.

It is clear that a machine tool condition monitoring system based on the surface of the work-piece will have the limitation that it cannot distinguish among all types of error. However, since each feature can be attributed to a restricted number of types of error, it still useful for a fast tracing of the source of error. Besides, it provides information which cannot be obtained from conventional methods. For example, a dynamometer, which is often used for assessing the magnitude of the tool wear, is suitable for determining the magnitude of the tool wear area, but will fail to give information about the waviness of the tool edge.

4.7 Conclusions

1. The surface generation is a complex process involving many interacting factors. Most of these play an important role in single-point diamond turning. Therefore, a model, which includes several of these and their most important interactions and influences upon the surface roughness, will give better predictions of the roughness parameters than simple expressions.

2. In the range of 50 - 400 nm for the peak-to-valley height the surface profile can be estimated within 10% by means of the model presented.

3. The deviations can be imputed to the omission of the contributions of several parameters, such as the additional variations in the operational settings that occurred when machining the test-pieces, the metallurgical properties and the initial roughness of the work-piece, the Spanzipfels and side flow, and the progress of the wear of the cutting edge during machining. Most of these contributions are not predictable, but since the roughness values can be estimated within 10%, they must be small in the range considered.

4. The model is suitable for examining the influence of diverse parameters, that are involved in turning.

5. A machine tool condition monitoring system based on the surface of the work-piece cannot distinguish among all types of error. Errors introduced by variations in the rotational speed can be similar to those due to instabilities of the feed velocity and vibrations in different directions may result in the same variation in the surface profile.
   But this system is still useful for the optimum utilisation of the machine and cutting tools, because it provides valuable information which cannot be obtained from conventional methods.

References

4.1. Ohmori, G.; Takada, S.:
Primary factors affecting accuracy in ultra-precision machining by diamond tool.
Bull. Japan Soc. of Prec. Engg., 16, No. 1, 1982, p. 3-7.

4.2. Brammertz, P.H.:
Die Entstehung der Oberflächenrauheit beim Feindrehen.
Industrie-Anzeiger,83,No.2,1961,p.25-32.

4.3. Stadler, H.J.; Freisleben, B.; Heubeck, C.:
Response of metallic materials to micromachining.
Abstracts 4th Int. Precision Engineering Seminar (Cranfield),1987.

4.4. Pekelharing, A.J.:
Das Fertigdrehen.
Microtecnic,14,No.2,1960,p.68-78.

4.5. Lo-A-Foe, T.C.G.; Dautzenberg, J.H.; van der Wolf, A.C.H. :
Cutting parameters and surface roughness in single-point diamond cutting.
Proceedings VII. Int. Oberflachenkolloquium Karl-Marx-Stadt, 1988,p.188-195.

4.6. Struik, K.G.; Fan Muchang :
Measurement of Shape and Roughness by a Modified Compact Disc Sensor Coupled to a Computer.
Abstracts 4th Int. Precision Engineering Seminar,1987,p.81-90.

4.7. de Bruin, J.G.; Burgmeijer, J.W.; Mesman, W.; Prast, G.; Wierenga, P.E.:
Comparison of some optical and mechanical roughness measurement techniques.(in Dutch)
Nat.Lab. Technical note No.155/85,1986.

4.8. Komanduri, R.:
Some aspects of machining with negative rake angle tools simulating grinding.
Int. J. Mach. Tool Des. Res.,11,1971,p.223

4.9. Avitzur, B.; Huang, C.K.; Zhu, Y.D.:
A friction model based on the upper-bound approach to the ridge and sublayer deformations.
Wear,95,1984,p.59-77.

4.10. Connolly, R.; Rubenstein, C.:
The mechanics of continuous chip formation in orthogonal cutting.
Int. J. Mach. Tool Des. Res.,8,1968,p.159-187.

4.11. Rakels, J.H.:
Monitoring of the machine-tool condition by optical surface finish analysis.
Proceedings VII. Int. Oberflachenkolloquium Karl-Marx-Stadt, 1988, p.228-235.

4.12. Hingle, H.T.:
Practical method of machine tool condition monitoring by analysis of component surface finish data.
Fourth Int. Symposium on Optical and Optoelectronic Applied Science and Engineering (The Hague),1987.

5 Conclusions and recommendations

The essential difference between the single point diamond turning and the conventional cutting process is the relative magnitude of the influence of some factors. The influence of anisotropy of material behaviour upon the surface roughness and the strain rate upon the specific stress and strain hardening exponent may be neglected in conventional cutting, but should not in single-point diamond turning.

The cutting forces can be estimated by means of the simple relationships:

$$F_w' = F_w + \Delta F_w = \frac{\mu_r}{1-\mu_r}.C.A + A_{VB}.C \qquad (2.57)$$

$$F_v' = F_v + \Delta F_v = \frac{1}{1-\mu_r}.C.A + \mu_f.A_{VB}.C \qquad (2.58)$$

The accuracy of the estimations will depend upon the accuracy of values used for the parameters involved, namely the friction coefficient at the rake face (μ_r) and at the flank face (μ_f), the specific stress (C) and the area of contact between the work-piece and the tool at the flank face (A_{VB}), and can be better than 20%. When a dynamometer is used for monotoring the condition of the cutting tool, the magnitude of the flank wear can be estimated from the measured forces by means of the above mentioned equations. Further research can be the determination of the material properties at high strain rates and a detailed examination of the stresses on the rake and on the clearance face, leading to more reliable values.

The structural behaviour of the lathe is not optimal. It can be improved by means of a simple numerical model, which makes use of experimental data. Since this model has not been evaluated, further research can be the modification of the lathe as proposed in Chapter 3 and verification of the calculated amount of improvement.

Usually, the finished surface will not be an exact replication of the shape of the cutting edge of the tool. This is due to the burnishing process on the clearance face, the elastic recovery of the bulk material and phenomena, such as Spanzipfels and side flow. Although these processes will not be easy to model, they should not be neglected because a better understanding of these may provide valuable information about the tool wear rate and the tolerances of tool wear for a certain roughness value.

In the range of 50 - 300 nm for the peak-to-valley height, the surface profile can be estimated within 10% with the model presented in Chapter 4.
Simulations, by means of this model, show that it is not always possible to attribute a variation in the surface of the work-piece to a certain machine tool error. Variations in the feed velocity will give a similar feature in the surface as variations in the rotational speed. Hence, a machine tool monitoring system, based on the surface of the work-piece, will have the limitation that it cannot distinguish among all types of error.
Nevertheless, it is useful for a fast tracing of the source of error, since each feature of the surface profile can be attributed to a restricted number of types of error.

The model is suitable for determining the optimal cutting conditions for a particular machine, cutting tool and work-piece material.
The deviation from the desired geometry of the work-piece can be calculated for several values of the operational settings and then, the appropriate conditions for a minimum deviation can chosen.

APPENDIX A

The mathematical background of modal analysis.

A lathe is a continuous system with an infinite number of degrees of freedom, but for a characterization of the dynamic behaviour, it is not necessary to consider all of these.
The lathe can be idealized as a system with a restricted number (n_d) of masses, springs and damping elements.
When a linear system is assumed, the displacements can be derived from a set of equations of motion:

$$[M]\{\ddot{x}(t)\} + [C]\{\dot{x}(t)\} + [K]\{x(t)\} = \{F(t)\} \qquad (A.1)$$

where

$[M]$ = $(n_d * n_d)$ mass matrix
$[C]$ = $(n_d * n_d)$ damping matrix
$[K]$ = $(n_d * n_d)$ stiffness matrix
$\{x(t)\}$ = $(n_d * 1)$ displacement vector
$\{\dot{x}(t)\}$ = $(n_d * 1)$ velocity vector
$\{\ddot{x}(t)\}$ = $(n_d * 1)$ acceleration vector

This equation can be transformed from the time domain to the frequency domain by Fourier Transform:

$$F(i\omega) = \int_{-\infty}^{\infty} F(t).e^{-i\omega t}.dt \qquad (A.2)$$

with ω = frequency

Then, the following equation is obtained:

$$-\omega^2[M]\{x(i\omega)\} + i\omega[C]\{x(i\omega)\} + [K]\{x(i\omega)\} = \{F(i\omega)\} \qquad (A.3)$$

And taking:

$$[B(i\omega)] = -\omega^2[M] + i\omega[C] + [K] \qquad (A.4)$$

Equation(A.3) becomes:

$$[B(i\omega)]\{x(i\omega)\} = \{F(i\omega)\} \tag{A.5}$$

The displacements can be determined from:

$$\{x(i\omega)\} = [B(i\omega)]^{-1}\{F(i\omega)\} = [H(i\omega)]\{F(i\omega)\} \tag{A.6}$$

$B(i\omega)$ is called the system matrix and $H(i\omega)$ the transfer function matrix.

The problem will be solved for three cases, namely :

1. undamped structures,
2. proportional damping and
3. general viscous damping.

A.1. Undamped structures

For an undamped structure the set of equations of motion (Eq.(A.3)) reduces to:

$$-\omega^2[M]\{x(i\omega)\} + [K]\{x(i\omega)\} = \{F(i\omega)\} \tag{A.7}$$

The free response of the structure can be determined from the homogeneous equation where $\{F(i\omega)\} = \{0\}$:

$$[-\omega^2[M] + [K]]\{x(i\omega)\} = \{0\} \tag{A.8}$$

This equation has a non-trivial solution if the determinant of the system matrix is zero:

$$\det[-\omega^2[M] + [K]] = 0 \tag{A.9}$$

The solutions of this characteristic equation are called eigenvalues and represent the square values of the natural frequencies. This is more explicit if Eq.(A.9) is rewritten as:

$$\det[[M]^{-1}[K] - \omega^2[I]] = 0 \tag{A.10}$$

The non-trivial solution vector $\{\psi_i\}$ corresponding to a particular eigenvalue is called eigenvector. It represents the deformation pattern of the structure at a vibration frequency ω_i, which is equal to the square root of the eigenvalue. The eigenvectors are also referred to as modal shapes or modal vectors. The arrangement in matrix format of these vectors constitutes the modal matrix $[\Psi]$.
An important property of the modal vectors is the orthogonality property, which can be expressed as:

$$[\Psi]^t[M][\Psi] = [m] \tag{A.11}$$

and

$$[\Psi]^t[K][\Psi] = [k] \tag{A.12}$$

where $[m]$ and $[k]$ are diagonal matrices.
This property may be used to transform the system of coupled equations, such as Eq.(A.7), into a set of uncoupled equations in which each equation contains only one dependent variable. Thus the problem of finding the response of a multidegree-of-freedom system reduces to a determination of the response of single degree-of-freedom systems.
Equation (A.7) can be transformed by premultiplying it by the transpose of the modal matrix ($[\Psi]^t$) and replacing the vector of displacements:

$$[\Psi]^t[-\omega^2[M] + [K]][\Psi]\{q(i\omega)\} = [\Psi]^t\{F(i\omega)\} \tag{A.13}$$

where

$$[\Psi]\{q(i\omega)\} = \{x(i\omega)\} \tag{A.14}$$

As the system matrix $[B(i\omega)] = [-\omega^2[M] + [K]]$ consists of terms which are proportional to $[M]$ and $[K]$, the modal shapes are also orthogonal to this matrix and the transformation $[\Psi]^t[-\omega^2[M] + [K]][\Psi]$ results in a diagonal matrix:

$$[\Psi]^t[-\omega^2[M] + [K]][\Psi] = -\omega^2[\Psi]^t[M][\Psi] + [\Psi]^t[K][\Psi] = \\ = -\omega^2[m] + [k] \tag{A.15}$$

Hence the set of coupled equations Eq.(A.7) is transformed into a set of uncoupled equations:

$$(-\omega^2 m_i + k_i)\{q_i(i\omega)\} = [\Psi]_i^t\{F(i\omega)\} \quad ,i = 1,\ldots\ldots,n_d \tag{A.16}$$

where

m_i = modal or equivalent mass for mode i

k_i = modal or equivalent stiffness for mode i

The uncoupling of coordinates in the equations is much more attractive when working in the time domain. There, the equations are differential equations, which are easier to solve when the coordinates are uncoupled.

With Eq.(A.14) and Eq.(A.15) the following relationship can be derived for the displacements:

$$\{x(i\omega)\} = [\Psi]\{q(i\omega)\} = [\Psi][-\omega^2[m] + [k]]^{-1}[\Psi]^t\{F(i\omega)\} = \\ = [H(i\omega)]\{F(i\omega)\} \tag{A.17}$$

The inverse of the diagonal matrix $[-\omega^2.[m] + [k]]$ is a diagonal matrix with components $\dfrac{1}{-\omega^2 m_i + k_i}$ and the following relationship between the components of the transfer function matrix $H(i\omega)$ and the modal parameters can be derived:

$$H_{ij}(i\omega) = \sum_{k=1}^{n} \frac{\Psi_{ik}\Psi_{jk}}{-\omega^2 m_k + k_k} = \sum_{k=1}^{n} \frac{\Psi_{ik}\Psi_{jk}}{m_k(\omega_k^2 - \omega^2)} \tag{A.18}$$

The component $H_{ij}(i\omega)$ represents the frequency response or transfer function for the displacement $x_i(i\omega)$ of a point i, excited by a force $F_j(i\omega)$ in point j.

A.2. Proportional damping

Equation(A.1) can be solved in a similar way as for the undamped system when the damping matrix [C] can be resolved in matrices proportional to [M] and [K]:

$$[C] = \alpha[M] + \beta[K] \tag{A.19}$$

Hence, the name "proportional damping".
This condition is sufficient but not necesarry. The necessary condition is that:

$$[\Psi]^t[C][\Psi] = [c] \tag{A.20}$$

where [c] = diagonal matrix

This is satisfied if the damping matrix can be expressed in the form:

$$[C] = [M] \sum_{i=-\infty}^{\infty} [a_i([M]^{-1}[K])^i] \tag{A.21}$$

Eq.(A.19) can be obtained from Eq.(A.21) when only two terms corresponding to i=0 and i=1 are considered.
The system matrix can be transformed to a diagonal matrix and the displacements can be uncoupled in the equations of motion.
The relationship for the displacements looks like Eq.(A.17) except an term for the damping:

$$x(i\omega) = \Psi*[-\omega^2[m] + i\omega.[c] + [k]]^{-1}[\Psi]^t\{F(i\omega)\} = [H(i\omega)]\{F(i\omega)\} \tag{A.22}$$

And the expression for the transfer function is:

$$H_{ij}(i\omega) = \sum_{k=1}^{n} \frac{\Psi_{ik}\Psi_{jk}}{-\omega^2 m_k + i\omega c_k + k_k} = \sum_{k=1}^{n} \frac{\Psi_{ik}\Psi_{jk}}{m_k(-\omega^2 + 2i\omega_k\zeta_k + \omega_k^2)} \tag{A.23}$$

where

$$\zeta_k = c_k/(2m_k\omega_k) = \text{modal damping ratio for mode k} \tag{A.24}$$

A.3. General viscous damping

In practice the condition of proportional damping is seldomly satisfied and the earlier described solution cannot be applied. For a relatively simple solution of Eq.(A.1) Duncan proposed to add to this equation the matrix identity:

$$[M]\{\dot{x}(t)\} - [M]\{\dot{x}(t)\} = \{0\} \tag{A.25}$$

This leads to a matrix equation of order $2n_d$:

$$\begin{bmatrix} [C] & [M] \\ [M] & [0] \end{bmatrix} \begin{bmatrix} \{\dot{x}(t)\} \\ \{\ddot{x}(t)\} \end{bmatrix} + \begin{bmatrix} [K] & [0] \\ [0] & [-M] \end{bmatrix} \begin{bmatrix} \{x(t)\} \\ \{\dot{x}(t)\} \end{bmatrix} = \begin{bmatrix} \{F(t)\} \\ \{0\} \end{bmatrix} \tag{A.26}$$

In frequency domain this equation becomes:

$$i\omega . \begin{bmatrix} [C] & [M] \\ [M] & [0] \end{bmatrix} \begin{bmatrix} \{x(i\omega)\} \\ i\omega\{x(i\omega)\} \end{bmatrix} + \begin{bmatrix} [K] & [0] \\ [0] & [-M] \end{bmatrix} \begin{bmatrix} \{x(i\omega)\} \\ i\omega\{x(i\omega)\} \end{bmatrix} = \begin{bmatrix} F(i\omega) \\ \{0\} \end{bmatrix} \tag{A.27}$$

In order to determine the modal parameters, the homogeneous equation is considered and transformed to the eigen problem:

$$[\,[A]^{-1}[B] + \lambda.[I]]\{y(i\omega)\} = \{0\} \tag{A.28}$$

where

$$A = \begin{bmatrix} [C] & [M] \\ [M] & [0] \end{bmatrix} \tag{A.29}$$

$$B = \begin{bmatrix} [K] & [0] \\ [0] & [-M] \end{bmatrix} \tag{A.30}$$

$$\{y(i\omega)\} = \begin{bmatrix} \{x(i\omega)\} \\ i\omega\{x(i\omega)\} \end{bmatrix} \tag{A.31}$$

$$\lambda = i\omega \tag{A.32}$$

The solution of this problem leads to 2n eigenvalues:

$$\lambda_{k1,2} = \delta_k \pm \upsilon_k \tag{A.33}$$

The physical meaning of these parameters will be easily seen if a single degree-of-freedom system is considered. The inverse of [A] for this is:

$$[A]^{-1} = \frac{1}{m^2} \cdot \begin{bmatrix} 0 & m \\ m & -c \end{bmatrix} \tag{A.34}$$

Hence:

$$[A]^{-1}[B] = \frac{1}{m} \cdot \begin{bmatrix} 0 & -m \\ k & c \end{bmatrix} \tag{A.35}$$

and the following characteristic equation can be derived:

$$\lambda^2 m + \lambda c + k = 0 \tag{A.36}$$

and the eigenvalues are:

$$\lambda_{1,2} = \frac{-c \pm \sqrt{(c^2 - 4mk)}}{2m} \tag{A.37}$$

With :

$$\omega = \sqrt{(k/m)} = \text{undamped eigenfrequency} \tag{A.38}$$

$$\zeta = c/2m\omega = \text{damping ratio} \tag{A.39}$$

Eq.(A.37) can be rewritten as:

$$\lambda_{1,2} = -\zeta\omega \pm \omega\sqrt{(\zeta^2 - 1)} \tag{A.40}$$

Consequently:

$$\delta_k = -\zeta_k \omega_k \tag{A.41}$$

$$\upsilon_k = \omega_k \sqrt{(\zeta_k^2 - 1)} \tag{A.42}$$

If the system is critically or over-damped ($\zeta \geq 1$) the eigenvalues are real and negative and represent the exponentional decay rate of the displacements:

$$x = D_1 e^{\lambda_1 t} + D_2 e^{\lambda_2 t} \tag{A.43}$$

In case of an underdamped system, the eigenvalues are complex and occur in conjugate pairs. The negative real part δ_k represents the exponentional decay of the displacements and the imaginary part υ_k corresponds to the frequency of the damped pulsation.
For every eigenvalue a complex mode shape $\{\Psi_k\}$ can be found and the modal matrix will be of the form:

$$[\varphi] = \begin{bmatrix} [\Psi] & [\Psi^*] \\ [\Psi][\lambda] & [\Psi^*][\lambda^*] \end{bmatrix} \tag{A.44}$$

where

$[\lambda]$ = a diagonal matrix of order n containing the eigenvalues with a positive imaginary part

$[\lambda^*]$ = a diagonal matrix of order n containing the eigenvalues with a negative imaginary part

$[\Psi]$ = the modal matrix of order n corresponding to the eigenvalues of $[\lambda]$

$[\Psi^*]$ = the modal matrix corresponding to the eigenvalues of $[\lambda^*]$

The matrices A and B can be transformed to diagonal matrices:

$$[\varphi]^t[A][\varphi] = [a] \tag{A.45}$$

$$[\varphi]^t[B][\varphi] = [b] \tag{A.46}$$

And the components of $y(i\omega)$ can be uncoupled by the transformation:

$$[\varphi]^t[i\omega[A] + [B]][\varphi]\{z(i\omega)\} = [i\omega[a] + [b]]\{z(i\omega)\} = [\varphi]^t\{F'(i\omega)\} \tag{A.47}$$

where

$$[\varphi]\{z(i\omega)\} = \{y(i\omega)\} \tag{A.48}$$

$$\{F'(i\omega)\} = \begin{bmatrix} \{F(i\omega)\} \\ \{[0]\} \end{bmatrix} \tag{A.49}$$

Consequently, the relationship for $y(i\omega)$ is:

$$\{y(i\omega)\} = [\varphi]\{z(i\omega)\} = [\varphi][i\omega[a]+[b]]^{-1}[\varphi]^t\{F'(i\omega)\} \tag{A.50}$$

According to Eq.(A.28) the matrix of the eigenvectors satisfies the condition:

$$[A]^{-1}[B][\varphi] = -[\varphi][\lambda'] \tag{A.51}$$

where $[\lambda']$ = diagonal matrix of order $2n_d$ containing the eigenvalues λ and λ^*.

With this equation the matrix [b] can be expressed in terms of [a]:

$$[b] = [\varphi]^t[B][\varphi] = [\varphi]^t[A][\varphi][\lambda'] = -[a][\lambda'] \tag{A.52}$$

Substitution of this in Eq.(A.50) yields:

$$\{y(i\omega)\} = [\varphi][i\omega[I]-[\lambda']]^{-1}[a]^{-1}[\varphi]^t\{F'(i\omega)\} \tag{A.53}$$

The displacements are represented by the first n_d components of $\{y(i\omega)\}$ and with Eq.(A.44) the following relationship for a component of the transfer function matrix H can be derived:

$$H_{ij}(i\omega) = \frac{x_i(i\omega)}{F_j(i\omega)} = \sum_{k=1}^{n}\left[\frac{\Psi_{ik}\Psi_{jk}}{a_k(i\omega-\lambda_k)} + \frac{\Psi^*_{ik}\Psi^*_{jk}}{a^*_k(i\omega-\lambda^*_k)}\right] \tag{A.54}$$

where a_k represents one of the first n and a^*_k one of the last n_d diagonal components of [a].

Normally the frequency response is expressed in the following form:

$$H_{ij}(i\omega) = \frac{x_i(i\omega)}{F_j(i\omega)} = \sum_{k=1}^{n}\left[\frac{R_{k,ij}}{i\omega-p_k} + \frac{R^*_{k,ij}}{i\omega-p^*_k}\right] \tag{A.55}$$

where

$$R_{k,ij} = \frac{\Psi_{ik}\Psi_{jk}}{a_k} = \text{residue} \tag{A.56}$$

$$p_k = \lambda_k = \text{pole} \tag{A.57}$$

The asterisk denotes the complex conjugate.

The residues and the poles can be spitted into real and imaginary components:

$$R_{k,ij} = U_{k,ij} + iV_{k,ij} \tag{A.58}$$

$$p_k = \delta_k + i\upsilon_k \tag{A.59}$$

The relationship for the frequency response becomes:

$$H_{ij}(i\omega) = \frac{x_i(i\omega)}{F_j(i\omega)} = \sum_{k=1}^{n}\left[\frac{U_{k,ij}+iV_{k,ij}}{-\delta_k+i(\omega-\upsilon_k)} + \frac{U_{k,ij}-iV_{k,ij}}{-\delta_k+i(\omega+\upsilon_k)}\right] \quad (A.60)$$

The amplitude of the displacement $x_i(i\omega)$ at mode k is proportional to $\sqrt{(U_{k,ij}^2+V_{k,ij}^2)}$ and the phase shift between the displacement and the driving force $F_j(i\omega)$ is $\tan^{-1}(V_{k,ij}/U_{k,ij})$.

A similar equation as for the undamped and proportional damped system can be obtained if the two terms of Eq.(A.60) are put together under one denominator and the Eqs.(A.41) and(A.42) are used for δ_k and υ_k:

$$H_{ij}(i\omega) = \sum_{k=1}^{n}\left[\frac{2U_{k,ij}(i\omega-\delta_k) - 2V_{k,ij}\upsilon_k}{\delta_k^2 - 2i\omega\delta_k - \omega^2 + \upsilon_k^2}\right] =$$

$$\sum_{k=1}^{n}\left[\frac{2U_{k,ij}(i\omega+\zeta_k\omega_k) - 2V_{k,ij}\omega_k\sqrt{(1-\zeta_k^2)}}{-\omega^2 - 2i\omega\zeta_k\omega_k + \omega_k^2}\right] \quad (A.61)$$

If the system is proportional damped the nominator will be real (Eq.(A.23)), which is the case when $U_{k,ij}$ is zero. With Eqs.(A.23) and (A.56) the imaginary part of the residue can be expressed in the following form:

$$V_{k,ij} = \frac{\Psi_{ik}\Psi_{jk}}{m_k}/(2\omega_k\sqrt{(1-\zeta_k^2)}) = \frac{\Psi_{ik}\Psi_{jk}}{ia_k} \quad (A.62)$$

Hence the relationship for the scaling constant a_k is:

$$a_k = -2im_k\omega_k\sqrt{(1-\zeta_k^2)} \quad (A.63)$$

For the undamped system ζ_k is zero, so the formulas for this can be obtained by omitting the terms with ζ_k.

If $U_{k,ij}$ is not equal to zero the numerator of Eq.(A.60) will be complex. Physically, this means that at a certain eigenfrequency ω_k the displacements of the points will show a phase shift, not only with respect to the driving force but also mutually.

APPENDIX B

The solution of the eigenproblem

After the determination of the system matrices the eigenproblem:

$$[[M]^{-1}[K] - \omega^2[I]]\{X(i\omega)\} = \{0\} \qquad (B.1)$$

is solved by the following procedure.

1. LU-decomposition of the mass matrix.
   This is done in order to transform the matrix $[M]^{-1}[K]$ into a symmetric matrix of which the eigenvalues and eigenvectors can determined rather easily by the Jacobi method.
   Since the mass matrix is positive definite, it can be decomposed by means of the Choleski algorithm [B.1], resulting in:

   $$[M] = [L][L]^t \qquad (B.2)$$

   where: [L] = triangle matrix
   t denotes the transpose

2. Calculation of the inverse of [L] and $[L]^t$.

3. Multiplying K by the inverse matrices:

   $$[A] = [L]^{-1}[K][L]^{-t} \qquad (B.3)$$

   where [A] = symmetric matrix

4. Solution of the eigenproblem of [A] by the Jacobi method [B.1].
   The matrix [A] is not the same as the matrix $[M]^{-1}[K]$:

   $$[M]^{-1}[K] = [L]^{-t}[L]^{-1}[K] = [L]^{-t}[A][L]^t \qquad (B.4)$$

   but the eigenvalues are the same and the eigenvectors can be easily transformed to those of $[M]^{-1}[K]$. This indirect method is chosen because the matrix $[M]^{-1}[K]$ is not symmetric and the Jacobi method cannot be used for this matrix.

5. Transforming the eigenvectors of A into the eigenvectors of $[M]^{-1}[K]$.

The eigenvectors of [A] satisfy the condition:

$$[A]\{\varphi\} = \lambda\{\varphi\} \tag{B.5}$$

where $\{\varphi\}$ = eigenvector

λ = eigenvalue

The equation for the eigenvector $\{\Psi\}$ of $[M]^{-1}[K]$ is:

$$[M]^{-1}[K]\{\Psi\} = [L]^{-t}[A][L]^{t}\{\Psi\} = \lambda\{\Psi\} \tag{B.6}$$

Premultiplying Eq.(B.6) by $[L]^{t}$ yields:

$$[A][L]^{t}[\Psi] = \lambda[L]^{t}[\Psi] \tag{B.7}$$

and with Eq.(B.5) the following relationship between the eigenvectors can be derived:

$$[L]^{t}\{\Psi\} = \{\varphi\} \tag{B.8}$$

Hence:

$$\{\Psi\} = [L]^{-t}\{\varphi\} \tag{B.9}$$

Reference

B.1 A.R. Gourlay, G.A. Watson:
Computational Methods for Matrix Eigenproblems.
John Wiley & Sons, 1973.

APPENDIX C

The accuracy of the measurement with a stylus instrument.

The accuracy of the measurement with a stylus instrument is limited by several factors, including the instrumental noise, the dimension of the stylus and the stylus loading. In this appendix the measuring error due to the dimension of the stylus and the stylus loading will be considered.

C.1. The dimension of the stylus

In practice, the stylus has a certain thickness and the tip is not sharp. Therefore, the tip will not become fully seated at the position of the point to be measured on the surface, which leads to measuring errors. These errors will depend upon the blunting of the tip, which is usually expressed in terms of a tip radius, the included angle of the stylus, the slope and spatial frequency of the surface irregularities. The relationship between the error and the dimensions of the stylus and the surface irregularities at V-shaped grooves (Fig.C.1) is:

$$\Delta t = x.\tan\theta_s - r + \sqrt{(r^2-1)} \qquad \text{if } x \leq r.\sin\beta_s \qquad (C.1)$$

$$\Delta t = x.\tan\theta_s - \frac{x}{\tan\beta_s} - \frac{r}{\sin\beta_s} - r \qquad \text{if } x \geq r.\sin\beta_s \text{ and } \theta_s \geq \beta_s \qquad (C.2)$$

$$\Delta t = r.\left(\frac{1}{\cos\theta_s} - 1\right) \qquad \text{if } x \geq r.\sin\beta_s \text{ and } \theta_s \leq \beta_s \qquad (C.3)$$

where r = tip radius

θ_s = slope of the valley

x = half the width of groove

β_s = half the included angle of the stylus.

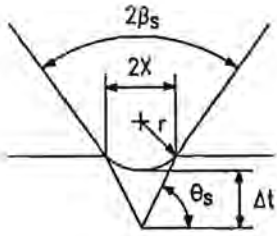

Fig.C.1a. The measuring error (Δt) if the width of the groove (2X) is smaller than the width of the rounded tip ($2r.\sin\beta_s$).

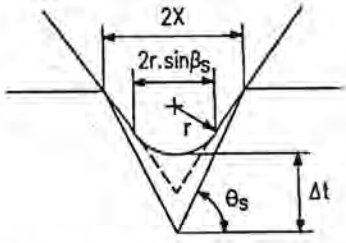

Fig.C.1b. The measuring error (Δt) if the width of the groove (2X) is larger than the width of the rounded tip ($2r.\sin\beta_s$).

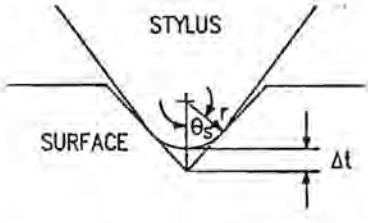

Fig.C.1c. The measuring error (Δt) if the width of the groove (2X) is larger than the width of the rounded tip ($2r.\sin\beta_s$) and the included angle of the groove is larger than that of the stylus.

It is obvious that, if the surface slope is very steep, the measuring error will be very large. For example, if the conditions for Eq.(C.3) are satisfied and the slope of the surface is 45 degrees, while the tip radius is 1 μm, then the measuring error will be 0.414 μm, which is very large. The error can be reduced by applying a stylus with a sharper tip, but even if the radius is 0.1 μm, which is in practice hardly attainable, the measuring error will be large (41 nm). Therefore, steeply sloped surface irregularities, such as scrathes and roughness due to short term waviness of the tool edge, cannot be measured accurately. For a tip radius of 1 μm the measuring error will be less than 10 nm if the slope of the surface is less than 8 degrees.

If the shape of the grooves is circular, which is the case in single-point diamond turning, then the measuring error will be (See Fig.C.2):

$$\Delta t = \sqrt{[R^2-(R-r)^2.\sin^2\theta_s]} - (R-r).\cos\theta_s - r \qquad (C.4)$$

where R = the radius of the cutting tool
r = radius of the stylus
θ_s = slope of the surface

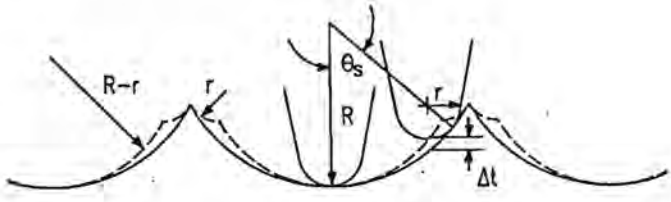

Fig.C.2. The measuring error (Δt) if the shape of the grooves is circular.

The measured shape (dashed line in Fig.C.2) is a circular segment with a radius of R-r, which is distorted at the boundaries by circular segments with a radius of r.
If the tool radius is much larger than the tip radius (R>>r) and the slopes of the surfaces are small, which is usually the case in single-point diamond turning, then Eq.(C.4) can be simplified to:

$$\Delta t = r.(\frac{1}{\cos\theta_s} - 1) \qquad (C.5)$$

which is the same as Eq.(C.3) for V-shaped grooves.
The slopes of the surfaces are mostly less than 3 degrees. If the tip radius is 1 μm, then the measuring error will be less than 1.4 nm, which is rather small. Hence, surface features produced by the radius of the cutting tool can be accurately represented.
In order to indicate the lateral resolution of the stylus instrument, a sinusoidal surface is considered (Fig.C.3).

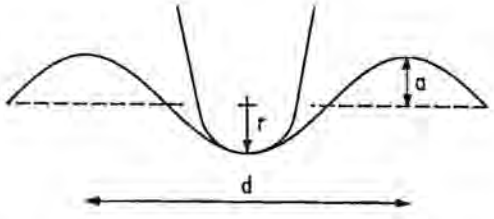

Fig.C.3. A sinusoidal surface component with an amplitude a and period d and a stylus of radius r.

For an accurate measurement of the surface feature, the curvature of the surface should be less than that of the stylus. This is the case if the following condition is fulfilled [C.1]:

$$d > 2\pi\sqrt{(ar)} \qquad (C.6)$$

If the amplitude (a) is equal to 25 nm and the tip radius (r) is equal to 1 μm then d must be greater than 1.0 μm. Thus, the lateral solution obtainable for the above mentioned conditions is 1.0 μm. It is clear that this value will be lower for smoother surfaces (smaller amplitude) and for smaller tip radii.

C.2 Stylus loading

Another measuring error is introduced by the stylus loading, which causes penetration of the stylus into the work-piece material. Since the stylus loading of the available surface profiling instrument (Talysurf) is quite large, about 1 mN, the depth of penetration and, consequently, the measuring error can be large too. However, if the differences in penetration depths along the surface are small then accurate measurements of the surface profiles can be obtained.
In order to determine the order of magnitude of these differences, the depth of penetration will be estimated for different slopes of the surface irregularities. This depth can be determined from the area of contact between the work-piece and the stylus, which in its turn can be calculated by means of the following equation:

$$A = \frac{P}{H_v} \qquad (C.7)$$

where A = the area of contact between the work-piece and the stylus
P = the stylus loading
H_v = the hardness of the work-piece material

With the assumptions that the peak is triangular and that influence of side flow may be neglected, the following relationship between the contact area (A), the depth of penetration (h), the stylus radius (r) and the slope of the peak (θ) can be derived (Fig.C.4):

$$A = 2\cos\theta_s.[\ (r-h).\sqrt{(2hr-h^2)} + (r^2-(r-h)^2\cos^2\theta_s).\tan^{-1}(\frac{\sqrt{(2hr-h^2)}}{(r-h)\sin\theta_s})\ ] \qquad (C.8)$$

The depth of penetration can be determined from this equation by means of an iterative method.

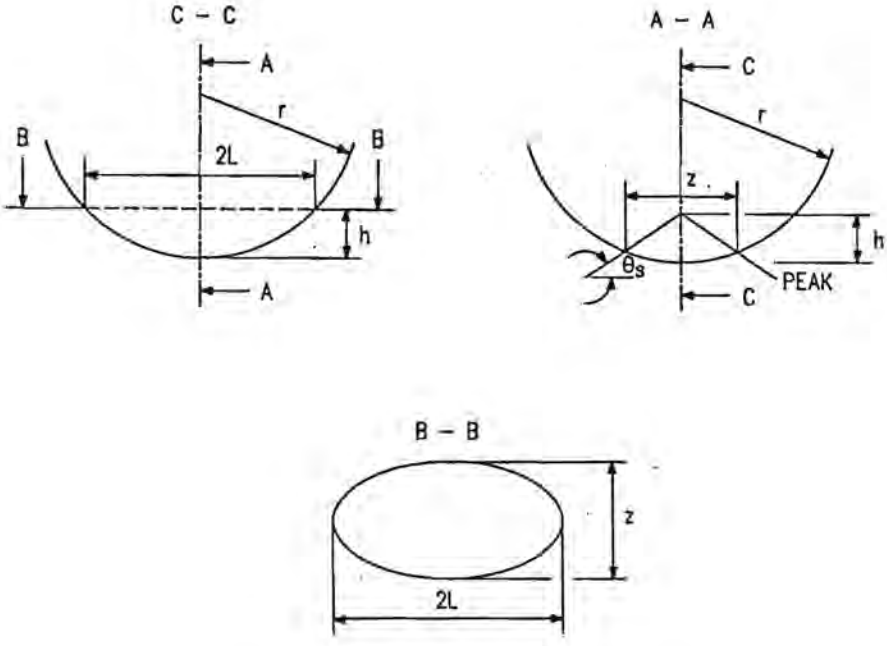

Fig.C.4. The depth of penetration (h) of a stylus in a peak and the projected area of contact (A_{ws}) between the stylus and the surface (B-B).

The calculated penetration depth for several values of the stylus radius and of the slope of the peak is depicted in Fig.C.5, which shows that the depth of penetration is considerable. However, the gradients of the curves, which look like lines, are small (about 6 nm/^{o}). This means that for diamond turned surfaces, where the slopes are mostly less than 3 degrees, the difference between the penetration depth at a peak and that at straight surface is less than 18 nm.

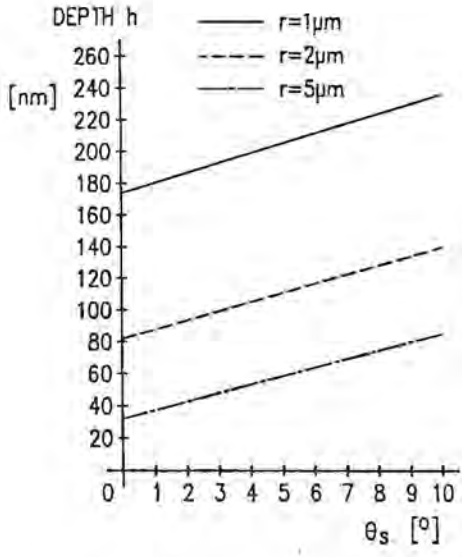

Fig.C.5. The depth of penetration (h) as a function of the slope angle of the surface peak for several values of the stylus radius.

Reference

C.1. Bennet, J.M.; Dancy, J.H.:
Stylus profiling instrument for measuring statistical properties of smooth optical surfaces.
Applied Optics, 20, No.10, 1981, p.1785-1802.

SAMENVATTING

Dit proefschrift behandelt de invloed van verschillende parameters op de oppervlaktekwaliteit van met monokristallijne diamant verspaande producten.
Het doel van de uitgevoerde studie was meer inzicht te verkrijgen in het verspaningsproces om daardoor de techniek van het fijnverspanen te verbeteren alsmede om tegemoet te komen aan de wens voor een betere kwaliteitsbewaking in de massaproductie.
Allereerst is er een verspaningsmodel, dat de invloed van machine-instelling (snijsnelheid, voeding en snedediepte), materiaaleigenschappen (in het bijzonder het plastisch gedrag) en de beitelgeometrie op de verspaningskrachten beschrijft, geëvalueerd (Hoofdstuk 2). Experimenteel werd aangetoond dat een aantal weggelaten factoren, zoals de invloed van de krachten op het vrijloopvlak en van de reksnelheid op het materiaalgedrag, niet verwaarloosbaar zijn bij het fijnverspanen. Indien deze factoren in het model werden opgenomen, konden de verspaningskrachten voorspeld worden met een nauwkeurigheid van 20%.
Vervolgens werd het dynamisch gedrag van een aanwezige fijnverspaningsbank onderzocht door middel van modale analyse (Hoofdstuk 3). Dit gedrag bleek niet optimaal te zijn. Daarom werd met behulp van een model, dat gebruik maakt van de resultaten van de modale analyse, gezocht naar mogelijke aanpassingen van de onderdelen om dit gedrag te verbeteren.
Tenslotte werd er numeriek simulatie model ontwikkeld om de directe invloed van de machine-instelling, de materiaaleigenschappen en de beitelgeometrie en hun indirecte invloed - via de verspaningskrachten-op de oppervlakteruwheid te bepalen (Hoofdstuk 4).
Dit model is experimenteel geverifieerd; het bleek dat de nauwkeurigheid ervan beter dan 10% was.
Het simuleren van de invloed van de verschillende parameters toonde aan dat waardevolle informatie over de conditie van de beitel en de draaibank verkregen kan worden uit het profiel van het fijnverspaand produktoppervlak. Het liet echter ook zien dat voor bepaalde variaties in het oppervlakteprofiel het niet mogelijk is eenduidig de oorzaak ervan aan te wijzen.

NAWOORD

Het onderzoek beschreven in dit proefschrift is uitgevoerd binnen the vakgroep Productietechniek en Automatisering van de faculteit Werktuigbouwkunde met steun van de Stichting voor de Technische Wetenschappen (STW).
Langs deze weg wil ik deze stichting en de medewerkers van de vakgroep WPA hartelijk bedanken voor de gelegenheid die zij mij boden dit proefschrift te realiseren.
Een bijzonder woord van dank gaat uit naar Jos Manders, Klaas Struik en Guus van Dijk, die mij bij de experimenten geholpen hebben.
Tevens wil ik mijn dank betuigen aan Prof.dr.ir. A.C.H. van der Wolf, Prof.ir. F. Doorschot, dr.ir. J.H. Dautzenberg, ir. T.G. Gijsbers en ir. J.A.W. Hijink, die regelmatig de moeite hebben genomen, het niveau van mijn onderzoek op peil te brengen.
Verder ben ik Philips B.V. bijzonder erkentelijk voor het ter beschikking stellen van de fijnverspaningsbank en de optische ruwheidstaster.
De leden van de promotie commissie en collega Pieter Jan Bolt wil ik bedanken voor hun moeite dit proefschrift kritisch door te nemen.
Studenten en collega's promovendi, die in de afgelopen jaren voor extra gezelligheid hebben gezorgd, mag ik ook niet vergeten te bedanken.

STELLINGEN

behorende bij het proefschrift

SINGLE-POINT DIAMOND TURNING

van

T.C.G. Lo-A-Foe

Eindhoven, 28 november 1988

1. Het essentieel verschil tussen het fijnverspanen en het grofverspanen is dat bij het fijnverspanen bepaalde factoren, zoals de reksnelheid, de krachten aan het vrijloopvlak en de metallurgische eigenschappen van het werkstukmateriaal, een belangrijker rol spelen.

   - Hoofdstukken 2 en 4 van dit proefschrift

2. Het feit, dat er nog geen algemeen geaccepteerd verspaningsmodel bestaat, is te wijten aan het gebrek aan infrastructuur voor het gezamenlijk onderzoeken van de vele processen, die bij het verspanen een rol spelen.

   - Shaw, M.C.:
     Metal cutting principles.
     Oxford,Clarendon press,1984

3. Het is niet altijd mogelijk uit de oppervlaktetopografie van het werkstuk te bepalen welk onderdeel van de machine of het proces niet voldoet.

   - Hoofdstuk 4 van dit proefschrift

   - Hingle, H.T.:
     A practical method of machine tool condition monitoring by analysis of component surface finish data.
     Fourth Int. Symposium on Optical and Optoelectronic Applied Science and Engineering (The Hague),1987

   - Condition Monitor,No.21,1988,(Patents)

4. Een eenvoudige methode om de specifieke spanning (C) bij hoge deformatiesnelheden te bepalen zou een verspaningsproef kunnen zijn.

   - Hoofdstuk 2 van dit proefschrift

   - Oxley, P.L.B.; Stevenson, M.G.:
     Measuring stress/strain properties at very high strain rates using a machining test.
     Journal of the Institute of Metals,95,1967,p.308-313

5. Bij bepaalde trillingen van de beitel t.o.v. het werkstuk kan ondanks een grote amplitude van de trilling toch een oppervlakteruwheid binnen de toleranties verkregen worden door de juiste machine-instelling en beitel te kiezen.

   - Hoofdstuk 4 van dit proefschrift

6. De toekomstig ingenieur in de precisietechniek zal zo weinig mogelijk gebruik moeten maken van statistische modellen.

   - McKeown, P.:
     High precision manufacturing in an advanced industrial economy.
     Preprints International Precision Engineering Seminar (Cranfield), 1987, p. 13-14

7. Een overeenkomst tussen het fijnverspanen en het promoveren is dat het resultaat sterk beinvloed wordt door de omgeving.

8. Door de snelle ontwikkelingen in de techniek zal het indelen van het onderwijsstelsel in afzonderlijke studierichtingen op den duur leiden tot nog grotere communicatieproblemen en onbegrip voor elkaars problemen.

9. Een gedwongen retraite na een ongeluk kan zeer verfrissend op de geest werken.

   - Eigen ervaring

10. Op den duur zal men niet meer exact kunnen bepalen welke nauwkeurigheid een product heeft, omdat men dan niet weet welke nauwkeurigheid de onderdelen van de mogelijke meetinstrumenten hebben.

11. De vaak gebruikte dimensie [$] voor de objectfunctie bij het optimaliseren van werktuigbouwkundige constructies mag dan een valse schijn van objectiviteit wekken, maar als deze dimensie wegvalt, is meestal het optimaliseren niet nodig.

    - Stelling 10 behorende bij het proefschrift 'On the dynamic characteristics of slideways' van Jos van Heck

12. Vandalisme is het gevolg van het gebrek aan mogelijkheden zich uit te leven en kan alleen bestreden worden door voldoende van deze mogelijkheden te creëren.